

Summer 6-29-2018

Magma Mixing at Oldoinyo Lengai: A Mineralogical and Trace Element Analysis of the 2007-8 Eruption.

Nicole Thomas
University of New Mexico

Tobias P. Fischer Dr.
University of New Mexico

Adrian J. Brearley Dr.
University of New Mexico

Follow this and additional works at: https://digitalrepository.unm.edu/eps_etds



Part of the [Geology Commons](#)

Recommended Citation

Thomas, Nicole; Tobias P. Fischer Dr.; and Adrian J. Brearley Dr.. "Magma Mixing at Oldoinyo Lengai: A Mineralogical and Trace Element Analysis of the 2007-8 Eruption.." (2018). https://digitalrepository.unm.edu/eps_etds/236

This Thesis is brought to you for free and open access by the Electronic Theses and Dissertations at UNM Digital Repository. It has been accepted for inclusion in Earth and Planetary Sciences ETDs by an authorized administrator of UNM Digital Repository. For more information, please contact disc@unm.edu.

Nicole Thomas

Candidate

Earth and Planetary Science

Department

This thesis is approved, and it is acceptable in quality and form for publication:

Approved by the Thesis Committee:

Tobias Fischer , Chairperson

Adrian Brearley

Brandon Schmandt

**MAGMA MIXING AT OL DOINYO LENGAI: A
MINERALOGICAL AND TRACE ELEMENT ANALYSIS OF
THE 2007-8 ERUPTION.**

by

NICOLE THOMAS

B.S, E & P.S., UNIVERSITY OF NEW MEXICO, 2013

THESIS

Submitted in Partial Fulfillment of the
Requirements for the Degree of

**Master of Science In
Earth and Planetary Science**

The University of New Mexico
Albuquerque, New Mexico

July, 2018

DEDICATION

In memory of my late husband, Dahlimar Lorinic (11/10/1961 – 02/19/2001), may
the stars forever guide your path.

This thesis work is dedicated to my family. To my three children: Raven, Isaiah and Draconis Thomas, who have always been beacons to guide my path through life. Your strength in the face of adversity, your kindness and generosity, these qualities have held me up in my darkest times, and in my brightest moments, I love you more than the moon and stars!, and to my parents, Steve Thomas and Rene Bushelle whose love and unfailing belief in me has always been a great source of strength and motivation.

ACKNOWLEDGMENTS

I extend the deepest of gratitude and acknowledgment to Dr. Tobias P. Fischer, my advisor and thesis chair for all the instruction, opportunities and patience he has granted me from the time we met in my first volcanology class to the summit of Oldoinyo Lengai, and now completion of these works.

In addition, I extend great thanks to Dr. Adrian Brearley, my mineralogy mentor, and committee member without which the mineralogical analyses would have been impossible. I would like to thank my committee members: Dr. Brandon Schmandt and Dr. Louis Scuderi for their guidance, academic support throughout this process. Many thanks to UNM EMPA technician Mike Spilde for all his invaluable SEM and EMPA instruction. I would also like to thank Dr. Steve Goldstein of Columbia U Lamot- Doherty Earth Observatory, and Dr. Chip Shearer (UNM).

In addition, I would like to thank Maarten de Moor for the ash samples collected at Lengai in 2008-9, and the photos of the stratigraphy column of ash deposits used in this study, and especially for the care which each layer was preserved. Thanks extended also to Melania Maqway who on our trip to the summit of Oldoinyo Lengai on July 4th 2014 found the CPX and Apatite xenolith (sample MEL-OL14) used in this study. I would also like to acknowledge The Maasai people for all their gracious help and hospitality on the many occasions in which samples from this study were collected from Oldoinyo Lengai (“The Mountain of God”).

CHAPTER I:

MAGMA MIXING AT OLDOINYO LENGAI: MINERALOGICAL ANALYSIS OF 2007-8 ERUPTIVE ASH DEPOSITS

By:

Nicole Thomas

B.S., Earth and Planetary Science, University of New Mexico, 2013

M.S., Earth and Planetary Science, University of New Mexico, 2018

Abstract

The 2007-8 eruption at Lengai was highly explosive, reaching plinian proportions, and the anhydrous nature of the nephelinite magma at Lengai, does not explain this highly volatile behavior. The increase in volatiles in a low H₂O nephelinite magma could occur from decompression melting of magma injection from a deeper source. Two distinct nephelinite compositions were identified in a mineralogical analyses of the ash erupted: a highly evolved nephelinite (OL2), with less than 3% glass from the magma chamber, as indicated by the highly peralkalitic feldspathoid: combeite (Na₂Ca₂Si₃O₉), commonly found in Lengai eruptive products (Dawson 1966, 1998), and a less evolved nephelinite magma, with up to 17% glass (ASHES) that did not contain combeite, with significantly higher Si, Al, Mg, and Mn content. Phase abundances, mineral formulas and endmember components are calculated for both assemblages. Phenocrysts encountered in both nephelinite assemblages are nepheline, augite (CPX), titanium andradite, wollastonite, apatite, and iron oxides. Magma mixing of the two nephelinites are evidenced by sudden changes in the melt chemistry in both ash sample sets. In the combeite-wollastonite-nephelinite (OL2), combeite microlites exhibit resorption rims

indicative of mineral instability, and nepheline from this assemblage has a distinct chemical boundary within $<8\mu\text{m}$ of the crystal rim, evidenced by Mg overgrowth. The wollastonite-nephelinite contains almost fully resorbed CPX, and resorption rims on Ti-andradite. Chemical changes resulting from a decrease of in Ca in the melt were detected in the rims of the wollastonite via electron microprobe WDS mapping. Two large CPX mineral grains with very differing composition and crystallization histories were found alongside each other in the wollastonite-nephelinite. Primary compositional differences between the two CPX grains are Ti and Mg content, the CPX mineral grain exhibiting disequilibrium features (ASH15-DISEQ) had higher total Mg (Mg content as high as 0.87 c.p.f.u., with an average of 0.72 c.p.f.u. as opposed to an average of 0.52 c.p.f.u.) and lower Ti (on average 0.00 c.p.f.u., as opposed to 0.02 c.p.f.u. in the second grain), than the zoned CPX (ASH15-EQUIL). The Ti-enriched CPX (ASH15-EQUIL) exhibits oscillatory compositional zoning, with few inclusions. The second (ASH15-DISEQ) is richer in Mg, and contains abundant inclusions, suggesting a high degree of disequilibrium. Both CPX and nepheline microlites and rims are enriched in Al, Mg and Mn, elements typically depleted in the highly peralkaline magma chamber. For both ash types the crystal size distribution is bimodal indicative of two stage cooling: an initial stage of slow cooling, with low nucleation and high growth rates producing large crystals (longest axes up to 1.5mm), followed by a stage of rapid cooling with high nucleation and low growth rates as the magma migrated to the surface. The large volume of visible interstitial glass vesicles in OL2 scoria is indicative of rapid degassing and subsequent crystallization in the magma chamber.

Table of Contents

CHAPTER I:

Abstract.....	v-vi
List of Figures.....	viii
List of Tables	ix
List of Appendices.....	x
Introduction	1
Volcanic Rock Sequence	1
Eruptive History and Crater Formation	1
Methods	4
Sample Collection and Processing	4
SEM Analyses.	4
Lispix™ Phase Mapping.	5
Electron Microprobe Analyses.	6
Results	11
Mineral Formula Calculations	11
Mineral Assemblages and Phase Abundances	12
Combeite.....	22
CPX	27
Nepheline.....	35
Garnet: Ti-Andradite	40
Discussion.....	48
Conclusion.....	59
Implications	62
References	66

List of Figures

Figure 1: Lengai Ash Stratigraphy	5
Figure 2: OL2 Lispix Multi-Phase Map	14
Figure 3: Nephelinite Phase Abundances (%)	16
Figures 4a-e: OL2 and ASHES SEM BSE Images (μm).....	18-22
Figure 5: OL2-A SEM BSE Images and X-Ray Maps.....	23
Figures 6a-c: Combeite Core to Rim Line Analyses	26-27
Figure 7: ASH15-DISEQ SEM BSE Images and X-Ray Map	31
Figure 8: ASH15-EQUIL SEM BSE Images and X-Ray Map.....	32
Figure 9: ASH15 EMPA core to rim point analyses.....	33
Figure 10a: CPX Compositions Quadrilateral Diagrams.....	34
Figure 10b: CPX Compositions Quadrilateral Diagrams	35
Figure 10c: CPX Compositions Quadrilateral Diagrams.....	36
Figure 11: Nepheline MgO and FeO (wt%).....	40
Figure 12: Ti-Andradite composition.	42
Figure 13: Ti-Andradite Major Cation Proportions (c.p.f.u. O[12])	43
Figure 14a-c: Resorbtion Figures.....	44-46

List of Tables

Table 1: Mineral Inclusions.	13
Table 2: Mean Mineral Formulas.	49

List of Appendices

Appendix A: Wavelength Dispersive Spectroscopy (WDS) Chemical Maps.....	A-1-19
Appendix B: Lispix Phase Mapping.....	A-70-76
Appendix C: EMPA Summary with Locations.....	A-77-165
Appendix D: Mineral Formula Calculations.....	A-166-196

Introduction

Ol Doinyo Lengai could be categorized as one of Earth's most unique active volcanic systems, a highly peralkalitic (Dawson 1998) mixed magma system containing nephelinite and natrocarbonatite co-existing in a silicate-carbonate liquid immiscibility system (Church and Jones 1995, Dawson 1962, Dawson et al 1996, Keller and Krafft 1990). This system contains some of the world's rarest minerals. In the natrocarbonatite, there are the anhydrous alkali carbonates, nyererite ($\text{Na}_2(\text{Ca}(\text{CO}_3)_2)$) and gregoryite (Na_2CO_3). In the nephelinite, both combeite ($\text{Na}_2\text{Ca}_2\text{Si}_3\text{O}_9$), a complex zeolite-like cyclosilicate, recently (Pekov et al., 2009) added to the lovozerite group, and igneous wollastonite (CaSiO_3) occur (Dawson et al., 1993, 1994, 1996, Klaudius and Keller 2006). The silicate lavas extruded at Lengai, are comprised of olivine-free nephelinites, phonolitic nephelinites, and phonolites (Dawson, 1962a). This study presents a mineralogical analysis of the eruptive ash deposits from the most recent 2007-8 eruption, which displayed a far higher degree of explosivity than previously observed or expected. It had been previously assumed that Lengai was in a period of decreased explosivity and H_2O content (Dawson, 1962, 1998). The 2007-8 eruption had a significantly higher H_2O content (de Moor et al., 2013), than the 1993 eruption (Koepenick, 1996), suggestive of volatile recharge from a deeper source.

This mineralogical analysis was conducted to assess the conditions of the magma chamber just prior to eruption. The ultra-fine ash deposits represent the best opportunity to capture the final chemical signature of the melt as ashes are

quickly quenched and contain a bulk of smaller, and therefore more recently crystallized mineral grains.

Volcanic Rock Sequence

Ol Doinyo Lengai was formed through a complex series of events, involving explosive eruptions of tuffs and agglomerates and effusive eruptions of lava. The carbonatite lavas emerge as black as oil and quickly weather to white when exposed to the atmosphere.

The cone rocks are not well exposed, however on the eastern slope there is partial exposure of a cross-section of the cone. Much of the cone is composed of weathered ash from the 1966-67 eruption. (Nyamweru et al 1988). J.B. Dawson was the first to map the volcano and establish the rock sequence from oldest to youngest as follows:

- I. Yellow tuffs and agglomerates with interbedded lavas that compose the bulk of the volcano.
- II. Grey tuffs and agglomerates make up parasitic cones and craters on the outer slopes.
- III. Black tuffs and agglomerates on the lower slopes of the mountain and high on its Western and North Western slopes.
- IV. *Melanephelinite extrusives (lava flows and parasitic cones) on the outer slopes of the volcano.
- V. Grey semi-indurated tuffs, consisting of nephelinite lapilli and mica plates cemented by carbonate, tentatively assigned to the eruption in 1917.
- VI. Poorly consolidated black ash on the north, west and south slopes (has also been observed at Olduvai Gorge, 45 miles to the west-southwest). Probably from 1940/1941 eruption.

VII. Variegated deposits of soda ash on the southern wall of the summit crater.
These may have formed in 1954/55.

VIII. Recent natrocarbonatite lavas of the northern crater floor. (Dawson 1962).

Eruptive History and Crater Formation

The dating of older eruptions of Ol Doinyo Lengai has considerable margins for error; however tephrochronology has given us a general idea of the eruptions that occurred in the past. The tephrochronology based estimated eruption sequence is: 1550BC \pm 1000 years, 50BC, 700AD, and 1350 AD all of which were explosive eruptions. In the 1800's the first historical records of eruptions appear; with two explosive central vent eruptions, in 1880 and 1882-1883 the latter of which had lava flows as well, both of these eruptions had a VEI of 2. This century, the first scientist to climb to Ol Doinyo Lengai's summit crater, otherwise known as the "Mountain of God" by the Masai was F. Jaeger in 1904. However it was six years later that the first description of the crater is recorded, "The northern crater had only a horse-shoe-shaped southern rim immediately below the summit, and lacked a crater rim to the north, west and east. The crater was more like a platform on which there was a central cone from which gas was being emitted,"(Muller and Uhlig et al 1910). Lava flows and pinnacles formed on the crater in 1913-1915 (Nyamweru 1988). In December 1916 there was an extremely explosive eruption; the eruption lasted until June 1917 and had a Volcanic Explosivity Index (VEI) of 3.

Historical records indicate there were eruptions in 1921 and 1926 of VEI 2, with explosive and central vent eruptions from the North crater, the eruption in 1921 even caused mud flows and lahars (Global Volcanism Program et al 2006). It is not until 1940 that we have a complete record of the phases of the eruption as well as a detailed

description of the crater after the eruption.

J. Richards recorded three phases to the eruption that started July 24 1940 and ended Feb 1941. This eruption had a VEI 3 and was an Explosive Central vent eruption with phreatic explosions and lahars causing damage to property and land and evacuation of the surrounding area (Global Volcanism Program et al 2006).

Several minor lava eruptions occurred in 1954, 1955 and 1958 (Nyamweru 1988). In 1960 eruptions started that continued for six consecutive years and culminated in 1966 with an explosion first observed by two airline pilots on the 14 of August 1966. This was a VEI 3 explosive central vent eruption. Ash fall was reported as far as Seronera (130 km west), Loliondo (70 km north-west) and Shombole (70 km north).

Lengai erupted explosively again with lava flows and causing significant damage with a VEI 3 from July 8th through Sept 4th of 1967.

Activity was reduced until 1983, when eruptions started and volcanic activity continued for 10 years until Sept 24th 1993, during this time a lava lake formed in the crater and there were explosions and overflow from the lava lake on several occasions. Magmatic evolution became a subject of interest as there were variances in the composition of the natrocarbonatite lavas erupted during this time (Jago and Gittins et al 1991).

A year later the volcano erupted again and has since then been at varying degrees of activity with ongoing fumaroles and low viscosity, low temperature lava flows. The lava continued to fill the crater over this time.

2007 started off as a calm year for Lengai with no activity or eruption of lava; however noises such as rumbling and churning of boiling magmas were reported by the

Masai and tourists alike. Throughout July and August earthquakes were ongoing, Barry Dawson and Roger Mitchell observed on the early morning of 24th September [2007] at ~ 0900hrs an eruption started that quickly formed a black eruption column with a plinian plume estimated to be ~ 6,000m high (Dawson and Mitchell et al Sept 2007).

The eruption lasted until April 2008. The natrocarbonatite flows resumed in 2012 (GVP), and in July 2014 an excursion to the summit of Oldoinyo Lengai undertaken by Tobias Fisher, Nicole Thomas, Hyun Wu Lee and Melania Maquay confirmed that a cinder cone was building on the floor of the collapsed crater of the 2007 eruption, and a magma pool was sloshing natrocarbonatite outward and back into the edifice of the volcano where it could be heard sloshing through the fumaroles on the western flank of the volcano.

Figure1: Oldoinyo Lengai Ash Stratigraphy Column of eruptive ash deposits from 2007-8.

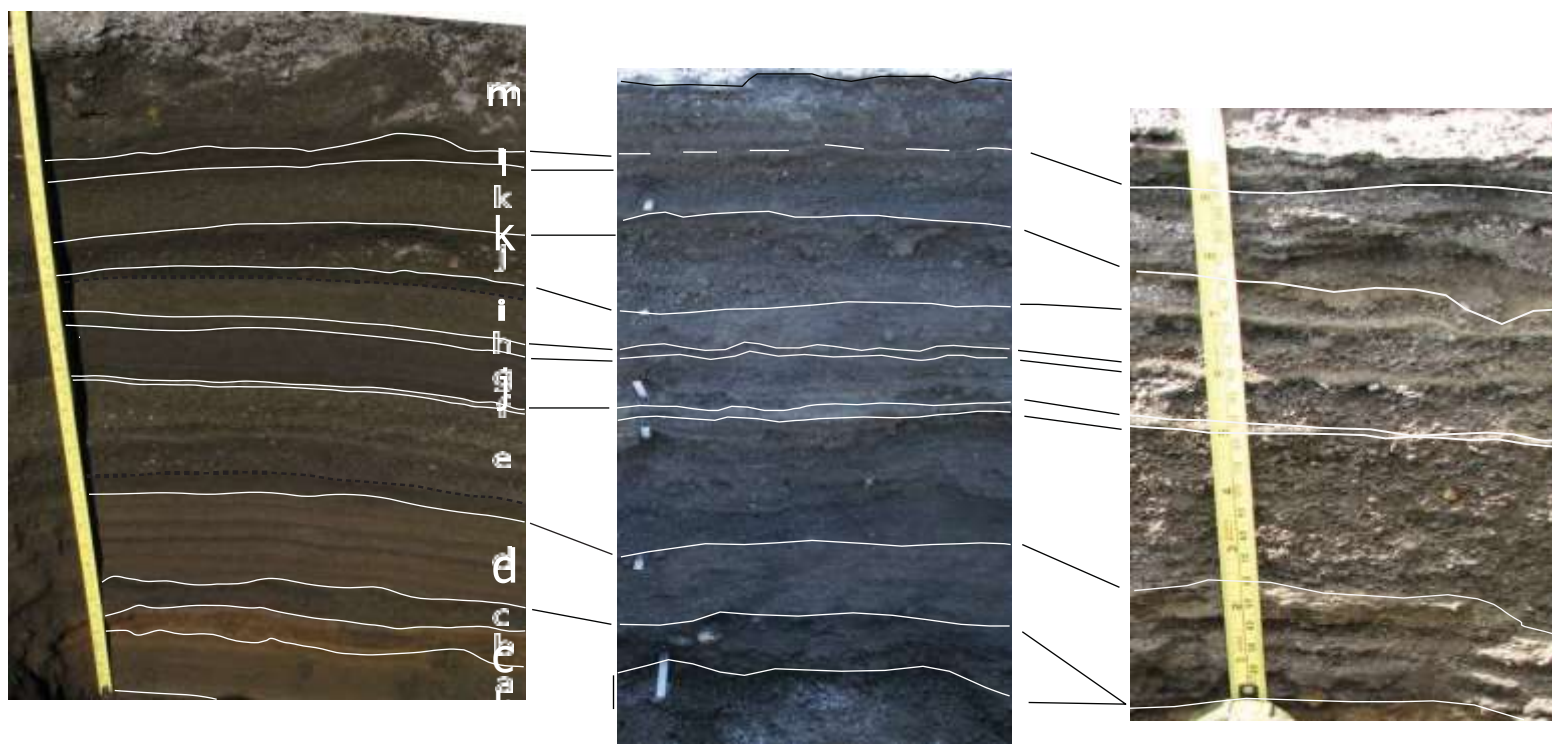


Figure 1: 2007-8 Oldoinyo Lengai Nephelinite Ash Stratigraphy Column.

All samples collected and stored by layer as shown by Maarten de Moor. Letters denote the layer identifier within the ash deposits.

The scale is in inches on the left and centimeters on the right of the measurement tape.

Sample "OL2" is from the M layers of these deposits. Samples labeled "ASHES" were from layers E-J.

Scale is in inches on the left and centimeters on the right.

Photos and samples courtesy of Maarten De Moor

Methods

Sample Collection and Processing

Distinct ash samples were collected from each layer of the ash fall deposits of the 2007-8 eruption by Maarten de Moor in 2008 and 2009 (these were distinct in that each ash layer in Figure 1 was preserved separately, as to maintain the integrity of the layers). The samples were collected at the summit of Oldoinyo Lengai (at 9715 ft elevation) in the Spring of 2009, just off of “King’s road”, which is a 10” wide trail that circles the vent at Lengai. A total of 6 of these ash sets were isolated for this analysis. The ash samples labeled OL2 (A-F) were collected from the M layer of the ash column in April 2008 (Figure 1).

The samples referred to as ASHES were collected in 2009 from the E thru J layers of the stratigraphic ash column (Figure 1). All samples were processed with anhydrous kerosene and anhydrous methanol. Ashes were set into 1” epoxy rounds and polished to a 0.03 μ m finish, then sputter-coated with carbon (~5nm thickness).

SEM Analyses

Six ash samples collected from the July 2007 eruption of Ol Doinyo Lengai were analyzed using the Scanning Electron Microscope at the University of New Mexico. Analytical conditions: 20kV, Spot size: 11 μ m, Aperture: 2, Z=10mm. Observations were made from the BSE (Backscattered Scanning Electron) images on: visible inclusions (co- crystallization), crystalline textures, mineral grain sizes, and groundmass composition. The nephelinite ROIs (regions of interest) were identified in the SEM through collection of backscatter images and EDS analysis (Appendix A). X-ray maps

for Al, C, Ca, Cl, Cr, Fe, K, Mg, Mn, N, O, P, Si and Ti (Appendix A) were obtained by energy dispersive spectroscopy (EDS). Mineral phases in the ashes were initially identified using qualitative EDS analysis.

Lispix™ Phase Mapping

Relative mineral abundance distribution was determined from multiphase maps created for each ash sample from their respective WDS elemental maps utilizing Lispix™, a computerized phase mapping program which allows the user to load BSE images and WDS chemical maps to create multiphase maps based on the elemental distribution within the sample. Lispix™ version Lx190P was used in generating mineral phase maps for 3 ash maps from the ASHES set (ASH09, ASH13, and ASH17) and from the OL2 sample.

Elemental components were selected for each phase based on the phases identified in the SEM analysis. Relative concentrations of each element were selected to correlate directly to mineral composition. Threshold values for each mineral phase were repeated for each sample to reproduce consistent multiphase maps for each ash sample. Masks for each element within a phase were created with the threshold slider (in percentiles), and stored as an elemental mask. Elemental masks for each phase were combined using the Lispix™ phase mapping tool to create the multiphase maps. Multiple mineral phase maps for a sample were overlaid using the phase map overlay tool (Lispix™ phase lists, threshold values, and multi-phase maps can be found in Appendix B).

Areas of volcanic glass far too fine for mineral analysis were identified using aluminum as a mask, and to filter out the areas of the map that do not contain the ash sample, since the carbon coat was thicker in these ‘holes’, a mask of high carbon content relative to

other elements present was used to remove these areas from the analysis. Relative proportions of each phase were determined by mapping all possible phases, and eliminating non-mapable areas from the total pixel area calculations. Relative mineral phase proportions were determined by the following calculation: [pixel count per phase]/[total pixels count of all phases]. Mineral proportions calculated for the ASHES set represent the mean of three ash samples (ASH-09, ASH-13, ASH-17). In order to eliminate potential errors from phase overlap, mineral chemistry was identified through uniquefying features with the threshold slider, for example the proportion of Ca in CPX vs. the proportion of Ca in Wollastonite.

Checks for unmapped phases were made by cross comparison of the original BSE ash maps to the zero use map generated on Lispix™ after all phases had been defined and non-mapable areas had been omitted. Non-mapable areas consist of the sample-free area composed primarily of the embedding epoxy. These areas were subtracted from the total multi-phase map area for all relative phase abundance calculations. Glass phases were defined to determine the relative abundance of phenocrysts vs. fine-grained groundmass with microlites summarized in Figure 2.

Electron Microprobe Analyses

Five ash samples (OL2, Ash02, Ash09, Ash13, and Ash15) were analyzed at University of New Mexico. Quantitative mineral analyses were obtained by electron microprobe at UNM's Institute of Meteoritics, Department of Earth and Planetary Sciences, with a JEOL 8800 Electron Microprobe with energy dispersive x-ray spectroscopy (EDS) and wave-dispersive spectroscopy (WDS). Operating conditions: accelerating voltage 15 kV, beam current 10 nA, counting times on peak and background were 30-60 seconds

(see Appendix C for a complete summary of peaks, backgrounds and counting times). Focused beam was 1 μm across. Standards used for the Ash02, Ash09, Ash13, Ash15 and Ash 17 samples were: Augite A209, Labradorite and Wollastonite. Elements analyzed for these ashes were: Cr, P, Ti, Si, Al, Mn, Fe, Mg, Ca Na, K, and Cl. for all elemental peaks, background counting times and ZAF corrections see Appendix C) in addition to S; Diopside and Augite A209 standards were used for OL2 Ashes (for a complete description of the standards run see Appendix C). A total of 226 point analyses were taken; 100 points from Ash02, Ash09, Ash13 and Ash15 and 116 point analyses from OL2 ashes (maps A- G). X-ray mapping was conducted on 3 sections of OL2 Ashes and on Ash15 (-EQUIL and - DISEQ) for Al, Ca, Fe, Na, and Ti.

A core to rim zoning profiles were measured on Ash15, containing two large (>500 μm on shortest axis) compositionally distinct CPX phenocrysts. Mineral formulae were calculated for all mineral phases from a total of 205 data points (Appendix D). A total of 11 EMPA analysis points were discarded due to low or poor totals (poor totals defined as totals that appeared non-representative as a result of the beam interaction area under the sample being much larger than the surface beam width and in these cases beam interaction area went beyond grain boundary). There are various factors that may have contributed to lower totals for Ti-andradite, CPX and combeite: the calculation of all Fe as Fe^{2+} , when a significant Fe^{3+} component is expected in these melts (Kladius and Keller 2006), undetected elements, poor polish due to the friability of these melts and small sample sizes. For these reasons totals between 103% and 95% were used in this study. The majority (>80%) of totals fell between 98-101%. nepheline and wollastonite totals were all between 99-101% ((Table C-3, Appendix C).

Results

Mineral Formula Calculations.

FeO wt% for Andradite and CPX was recalculated for Fe₂O₃ and FeO according to charge balance utilizing the updated [Olivine, Pyroxene, Garnet, Spinel and Feldspar Spreadsheets](#), which utilizes the Droop method (Droop, 1987).

Calculating the Ti- andradite mineral formulae from peralkalitic systems can pose difficulties in determining cation site occupancies for Al, Ti⁴⁺ and Fe³⁺ in the presence of the lack of sufficient Si to fill the tetrahedral site. Since Lengai magmas are particularly Al poor, the issue becomes the placement of the Ti and Fe. Contrary to crystallographic charge and size cation site placement principles, studies suggest that Fe³⁺ preferentially enters the tetrahedral site over Ti⁴⁺ (Huggins, 1977), and Fe³⁺ can be found in both tetrahedral and octahedral coordination in natural Ti-bearing Andradite (Manning 1972, Kühberger 1989).

Experimental studies (Kühberger, 1989) of Ti-andradite synthesized at a pressure of $P(\text{H}_2\text{O})=3$ kbar and temperatures of 700–800° C, with oxygen fugacities controlled by [Ni/NiO; SiO₂ + Fe/Fe₂SiO₄] solid state buffer, demonstrated that at high oxygen fugacities these Ti-andradites have Fe³⁺ present in both octahedral and tetrahedral coordination; Ti-andradites from low oxygen fugacities also have tetrahedrally and octahedrally coordinated Fe²⁺ as well. Therefore Kühberger et al (1989) presented that charge balance in these “reduced” garnets must be

maintained by $O^{2-} \rightleftharpoons OH$ substitution by 2 mechanisms: $(SiO_4)^{4-} \rightleftharpoons (O_4H_4)^{4-}$ and $(Fe^{3+}O_6)^{9-} \rightleftharpoons (Fe^{2+}O_5OH)^{9-}$. This was supported by their FTIR spectra which confirmed the presence of (OH)- bound in the mineral structure, and that in a natural sample of these “reduced” Ti-andradites tetrahedrally and octahedrally coordinated Fe^{3+} are observed together with Fe^{2+} on all three cation sites of the garnet structure (Kühberger et al, 1988). In the past, Lengai Nephelinite magmas were typically considered to be highly anhydrous (Mitchell, 2007). However recent studies (De Moor et al, 2013) revealed as high as 10.1 wt% H_2O in nepheline glass inclusions from the same deposits analyzed in this study. Therefore, it is possible the presence of undetected structurally bound (OH)- in the Ti-andradite from these deposits is also responsible low totals found in the EMPA analyses. The Kühberger study does not align with classical ionic radius criteria (Shannon and Prewitt, 1969) in suggesting that Fe^{2+} substituted for Si^{4+} in tetrahedral co-ordination, however in their synthetic samples, the dodecahedral positions were completely occupied by Ca^{2+} , which would also be the case in a Ca enriched melt such as that found in Lengai (Dawson 1966). Although, Fe^{2+} typically occupies the octahedral sites in silicates, it has been found in tetrahedral co-ordination in other minerals such as: melilite (Seifert and Federico 1987), staurolite (Regnard 1976). It has been observed that octahedrally coordinated Ti^{3+} may be present in the andradite mineral structure (Howie, 1968). As noted there are several complexities surrounding the cation placement in Ti-andradites. For this study Fe^{3+} has been placed in octahedral coordination, however the data presented above demonstrates that this interpretation of the cation assignment for these garnets can be challenged. The Ti site placement was based on initially

assigning needed Ti cations to completely fill the tetrahedral site and the excess of Ti cations were assigned to the octahedral site. To determine which site to assign Ti and Fe³⁺ cations, Fe and Ti cation values were plotted against Si (Figure 13), clearly demonstrating that Ti content is inversely correlated to Si, whereas the Fe³⁺ does not change with Si content. In fact the Fe³⁺ content was also inversely correlated to Ti, so that samples low in Si were also also low in Fe³⁺. Therefore, the Fe³⁺ content appears to be dependent rather on the Ti content (Figure 13) as increasing Fe³⁺ was evident with lower Ti, indicating the Fe³⁺ is not tetrahedrally coordinated in these garnets, and that the tetrahedral cation substitution order is Si>>Al>>Ti> Fe³⁺.

The apatite mineral formula was simply as oxide data and the mineral formulae were not recalculated due to the complex nature of the formula and anion content

Mean and individual crystal compositions were calculated (Tables D-1 thru D-20, Appendix D) and summarized in Table 2.

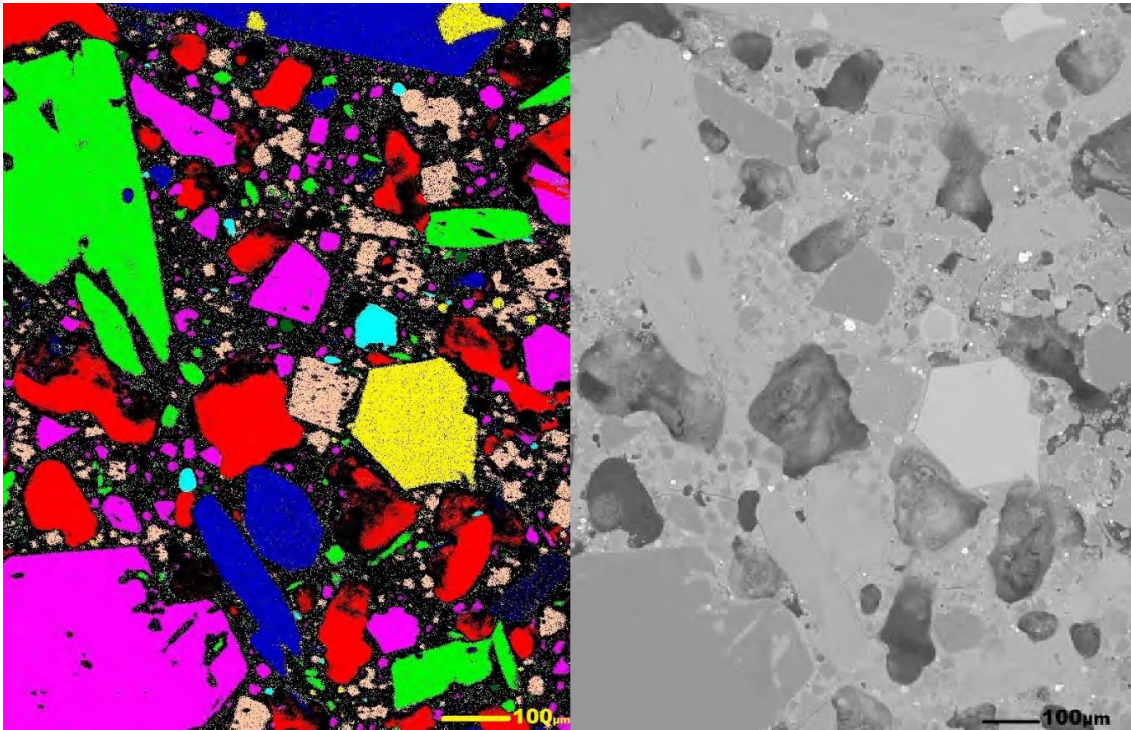
Mineral Assemblages and Phase Abundances

SEM analyses of the ash samples revealed two distinct nephelinite compositions, differentiated by mineral content, mineral chemical composition and glass abundances. The most distinctive difference in the ash sample sets (labeled OL2 and ASHES) was the mineral assemblages. Sample set OL2 (A thru G) contained combeite (Na₂Ca₂Si₃O₉), a very rare mineral found in only a few locations in the EARS, and commonly found in Lengai erupta (Dawson 1966, 1998). In contrast,

the other nephelinite ash samples, the ASHES sample set (ASH-02, -09, -13, -15, -17) did not contain combeite. Relative glass to mineral content (Figure 2) of the combeite-free assemblage (ASHES) was an order of magnitude higher (up to 17% glass) than OL2, the combeite-bearing assemblage (3% glass). All other minerals were common to both nephelinite assemblages: nepheline ($\text{NaAlSi}_3\text{O}_8$), clinopyroxene-CPX ($(\text{Ca},\text{Na})(\text{Mg},\text{Fe},\text{Al},\text{Ti})(\text{Si},\text{Al})_2\text{O}_6$), titanium-rich andradite ($\text{Ca}_3\text{Fe}^3_2\text{Si}_3\text{O}_{12}$), wollastonite (CaSiO_3), apatite $\text{Ca}_5\text{P}_3\text{O}_{12}(\text{OH},\text{F},\text{Cl})$, and Fe-oxides (FeO). Relative abundances of each mineral were quantified from the Lispix[®] multi-phase maps generated from the WDS elemental maps and the backscatter (BSE) SEM (appendix B).

Inclusion relationships as observed in the Lispix[®] multi-phase maps for both nephelinite assemblages are summarized in Table 1. All SEM BSE images can be found in Appendix A, and WDS chemical maps, Lispix multi-phase maps, and Lispix metadata are in Appendix B).

Figure 2: OL2 Lispix Phase Map



Phase	Color in Map	% Area ^a	% Of Mapped Area ^b
CPX	Dark Blue	6.23	14.11
Ti-Andradite	Yellow	3.56	8.06
Nepheline	Magenta	14.41	32.64
Apatite	Cyan - light blue	0.67	1.52
Fe Oxide	Dark Green	0.25	0.57
Wollastonite	Green	11.22	25.41
Glass	Light Green	1.33	3.01
Combeite	Peach	6.48	14.68
Vesicles ^c	Red	10.99	
Groundmass/Epoxy ^c	Black	44.86	
Totals:		100	100
Mapped phase total ^d		44.15	

^a: % Area is referring to the amount of area within a particular phase which was mapped by Lispix as a result of the phase threshold (phase threshold and chemical slider data can be found in appendix B).

^b: % of mapped area is referring the phase abundances normalized to the total area of mapped phases. The vesicles/epoxy phase and unmapped area is excluded from this total.

^c: Mapped areas excluded from phase abundance calculations.

^d: Area total of mapped phases excluding vesicles and epoxy areas.

Figure 2: OL2 CWN (combeitic wollastonite-nepheline) Lispix™ phase map from EDS data (µm) on the left. Ne: nepheline; CPX; clinopyroxene; Grnt: Ti-andradite; Wo: wollastonite; Comb; combeite; Ap; Apatite. Phase abundances from mineral grains ranging from large phenocrysts (>400µm diameter on the shortest axis) to microlites in the groundmass (mineral grains as small as ~3 µm diameter on the shortest axis). Red areas are “vesicles” or regions of bubbles that formed in the epoxy. Black areas are groundmass in which no microlites could be identified according the phase thresholds used (Appendix B). Visible inclusion relationships: Ti-andradite in CPX (top of Lispix™ phase map), CPX in wollastonite (blue in green: mid-upper left-hand side and lower right-hand corner of Lispix™ phase map).

Table 1- Inclusion relationships in Lengai 2007-8 nephelinite assemblages: ASHES (WN: wollastonite-nephelinite) and OL2 (CWN: combeitic wollastonite-nephelinite) as determined from SEM EDS maps and BSE Images.

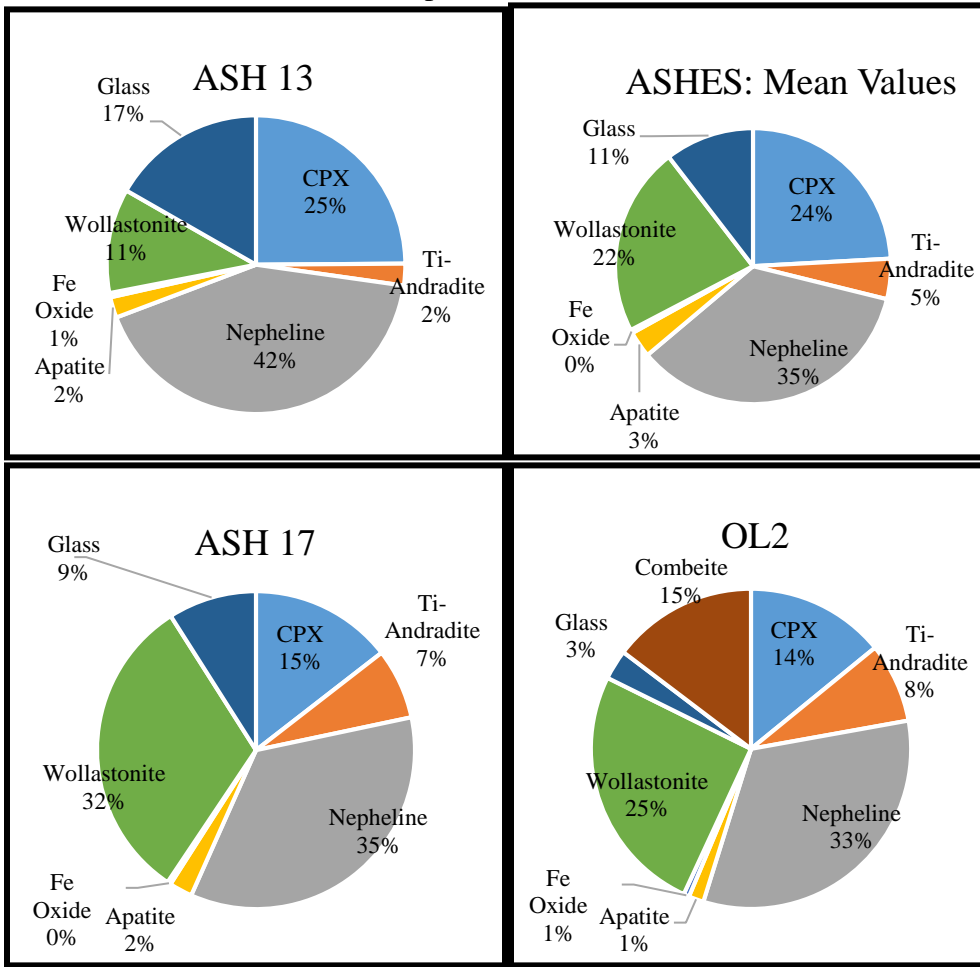
Inclusion	Host Crystal					
	Apatite	CPX	Garnet	Nepheline	Wollastonite	Combeite
ASHES (WN)						
Apatite	NA	Yes		Yes		NP
CPX		NA	Yes	Yes	Yes	NP
Garnet		Yes	NA		Yes	NP
Nepheline		Yes		NA	Yes	NP
Wollastonite		Yes		Yes	NA	NP
OL2 (CWN)						
Apatite	NA					Yes
CPX		NA		Yes	Yes	Yes
Garnet			NA			Yes
Nepheline		Yes	Yes	NA	Yes	Yes
Wollastonite		Yes		Yes	NA	Yes
Combeite						NA

Blanks indicate an inclusion was not observed

NA: Indicates that combination is not applicable

NP: Indicates that mineral was not present

Figure 3: OL2 and ASHES: Nephelinite Phase Abundances (%) from Lispix™ phase mapping of WN (wollastonite-nephelinite: ASH 13, ASH 17, ASHES mean values) and CWN (combeitic wollastonite nephelinite: OL2).



Mineral abundances from phase maps generated with Lispix™ from SEM EDS chemical maps for two different nephelinite assemblages: ASHES (WN: wollastonite nephelinite assemblage from layers E-J) and OL2 (CWN: combeitic wollastonite-nephelinite from layers BCD and M). Minerals are represented as follows: grey-nepheline, green-wollastonite, light blue-CPX, orange-andradite, dark blue-glass, yellow-apatite, brown-combeite (only present in the OL2 assemblage), and Fe-oxide is in such low abundances as to make it barely visible. All values are in normalized mean %. Glass content is the highest in the WN – sample Ash13, which also has the highest CPX (25%) and nepheline abundances (42%), with lowest wollastonite (11%) and Ti-andradite (2%) of all samples. In contrast, WN Sample ASH17 contains the highest wollastonite (32%) abundance, with lower CPX (15%) and nepheline (35%). CWN sample OL2 was the only assemblage with combeite (15%), also had the lowest glass (3%), CPX (14%) and nepheline (33%) abundances of all samples, and the highest abundance of Ti-andradite (8%).

Mineral Assemblages and Phase Abundances (Cont'd)

Electron microprobe mineral analyses confirmed the two nephelinite mineral assemblages differed by the presence of combeite in the OL2 ash sample. As seen in the Lispix™ phase mapping, ASH-07 from the wollastonite-nephelinite (ASHES-WN) combeite-free assemblage had the highest glass content at 17%, and the mean glass content was 11%. In contrast, the combeite-bearing assemblage (OL2-CWN) had very low glass content (3% mean), and a high abundance of microlite crystal mush texture as seen in the EMPA high magnification x-ray map for OL2-A (Figure 4a), with Ti-andradite, wollastonite, combeite, and nepheline microlites ranging from 1-15µm (shortest diameter). Inclusion relationships (Table 1) indicate that in the CWN assemblage (OL2 samples), combeite contained inclusions of all other phases, even apatite, therefore all other phases were present when combeite crystallized. In contrast, combeite was not found included in any of the mineral phases.

Figure 4a: OL2-G EMPA BSE Image (μm) of CWN (combeitic wollastonite-nephelinite)

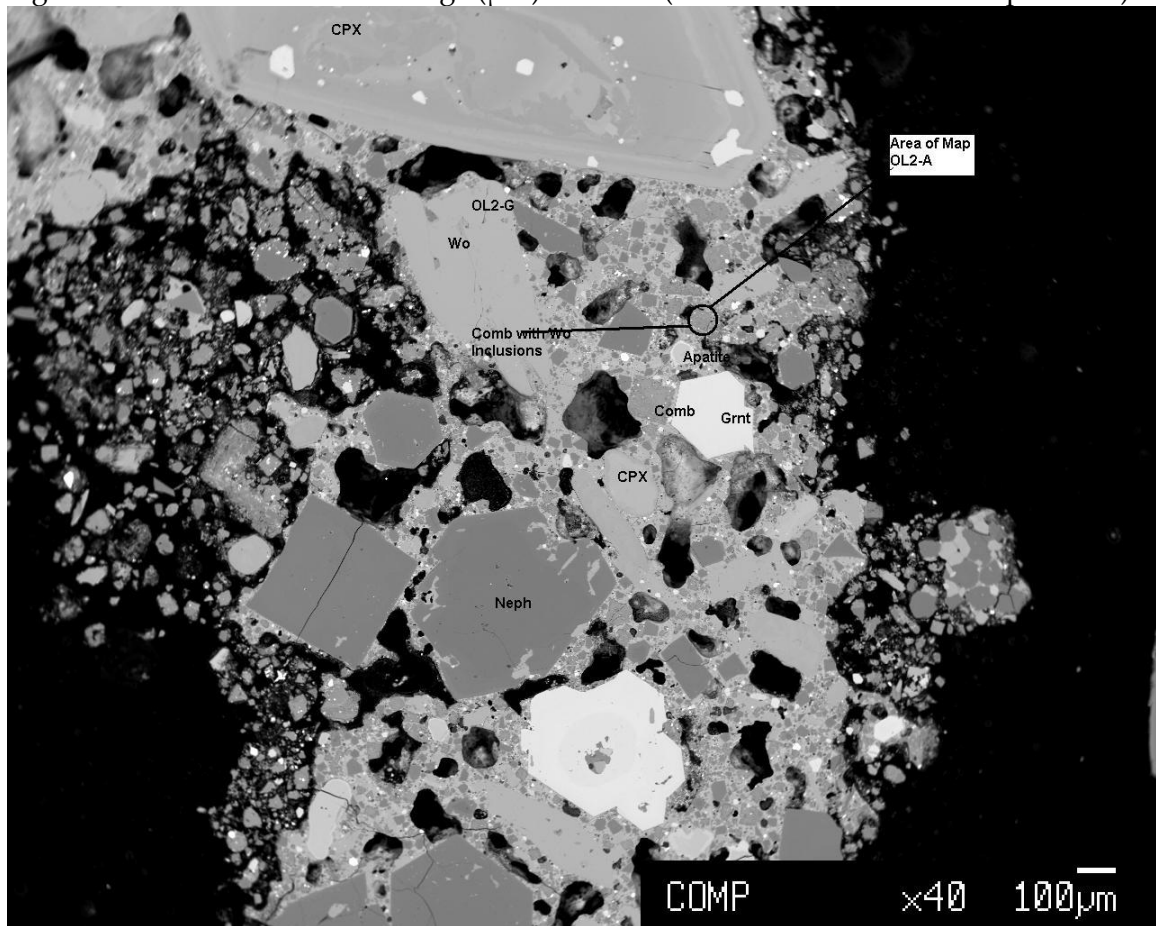


Figure 4a: A: Large ($\sim 500\mu\text{m}$ on shortest axis) CPX phenocryst, with mottled core and oscillatory banding within $100\mu\text{m}$ of crystal rim, multiple inclusions. Oscillatory banding is indicative of variation in Fe and Ti concentrations, with abundant Ti-andradite inclusions. B: Large ($\sim 75\mu\text{m}$ on shortest axis) Ti-andradite inclusion in CPX. C: Ti-andradite phenocryst with core to rim compositional zoning. D: Ti-andradite without any evidence of compositional zoning. E: Euhedral nepheline phenocryst. F: Non-euhedral nepheline phenocryst. G: Wollastoite phenocryst, with CPX inclusions. H: Location of OL2-A maps found in Figures 4b and 4c.

Figure 4b: BSE image of CWN (combeitic wollastonite-nephelinite, sample OL2-A) from FEI Quanta FEGSEM (μm).



Figure 4b: A: Combeite mineral grain from CWN (OL2-A). Core contains higher Si, Ca and Na, compositional change occurs within $10\mu\text{m}$ of grain rim. B: Rim demonstrates partial resorbtion and contains higher abundances of Al, K, and S. Inclusions in the rim are: nephelinie, CPX, wollastonite, and Ti-andradite. C: Nepheline mineral grain ($20\mu\text{m}$ on shortest axis), inclusion free. D: Mineral microlites in quench texture.

Figure 4c: BSE image of CWN (combeitic wollastonite-nephelinite sample OL2-A) from FEI Quanta FEGSEM (μm).

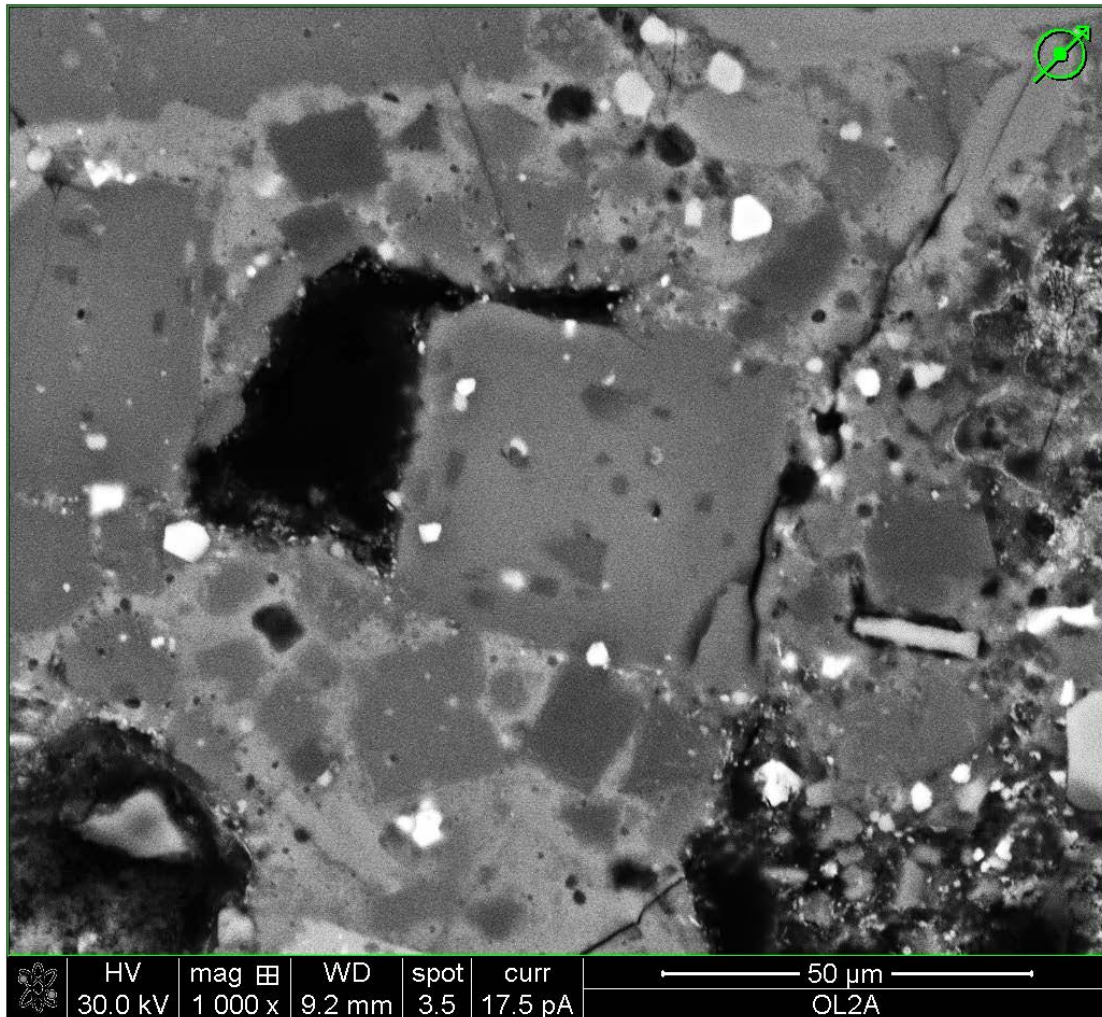


Figure 4c: A: Combeite mineral grain in CWN assemblage (combeitic wollastonite-nephelinite) with inclusions of nepheline, wollastonite and Ti-andradite. B: melt area, vesiculated, with fewer microlites than Figure 4a, mineral boundaries showing evidence of resorbtion. C: nepheline mineral grain (12 μm in diameter on shortest axis with step zoning within 3 μm of rim. D: Wollastonite mineral grains with core to rim compositional gradation, increase Na in rims. E: Wollastonite mineral grain (16 μm long and 4 μm wide

Figure 4d: BSE image of WN (wollastonite-nephelinite sample ASH-02) from FEI Quanta FEGSEM (μm).

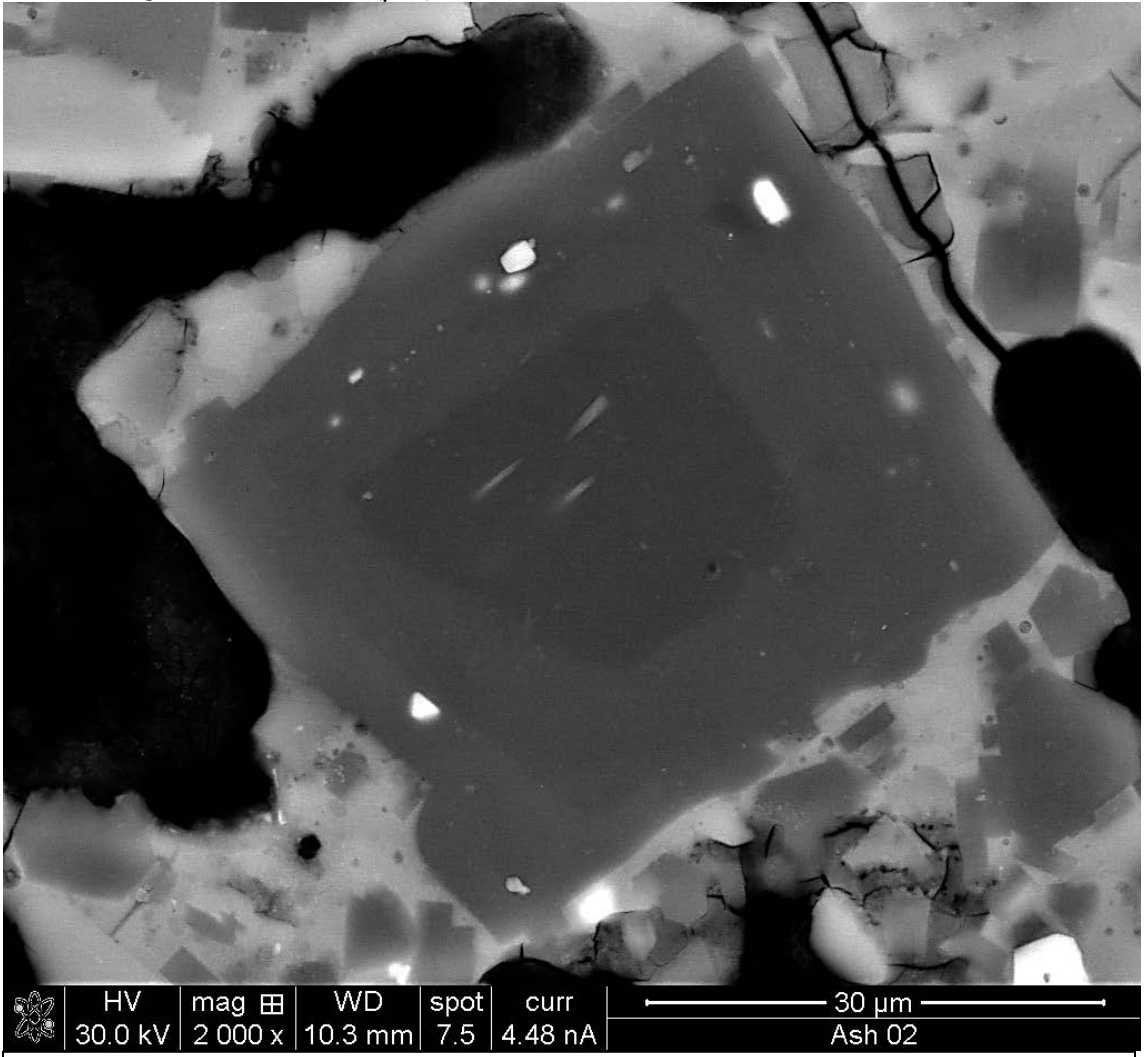


Figure 4d: A: Nepheline mineral grain ($\sim 45\mu\text{m}$ in diameter) with step zoning. B: Rim of nepheline mineral grain is relatively enriched in FeO (5 wt% increase) and MgO (from 0.0 wt% in core to 0.25 wt% in rim) Visible inclusions are Ti-andradite. C: Microlites of nepheline, wollastonite and Ti-andradite in quench material

Figure 4e: BSE image of WN (wollastonite-nephelinite sample ASH-13) from FEI Quanta FEGSEM (μm).

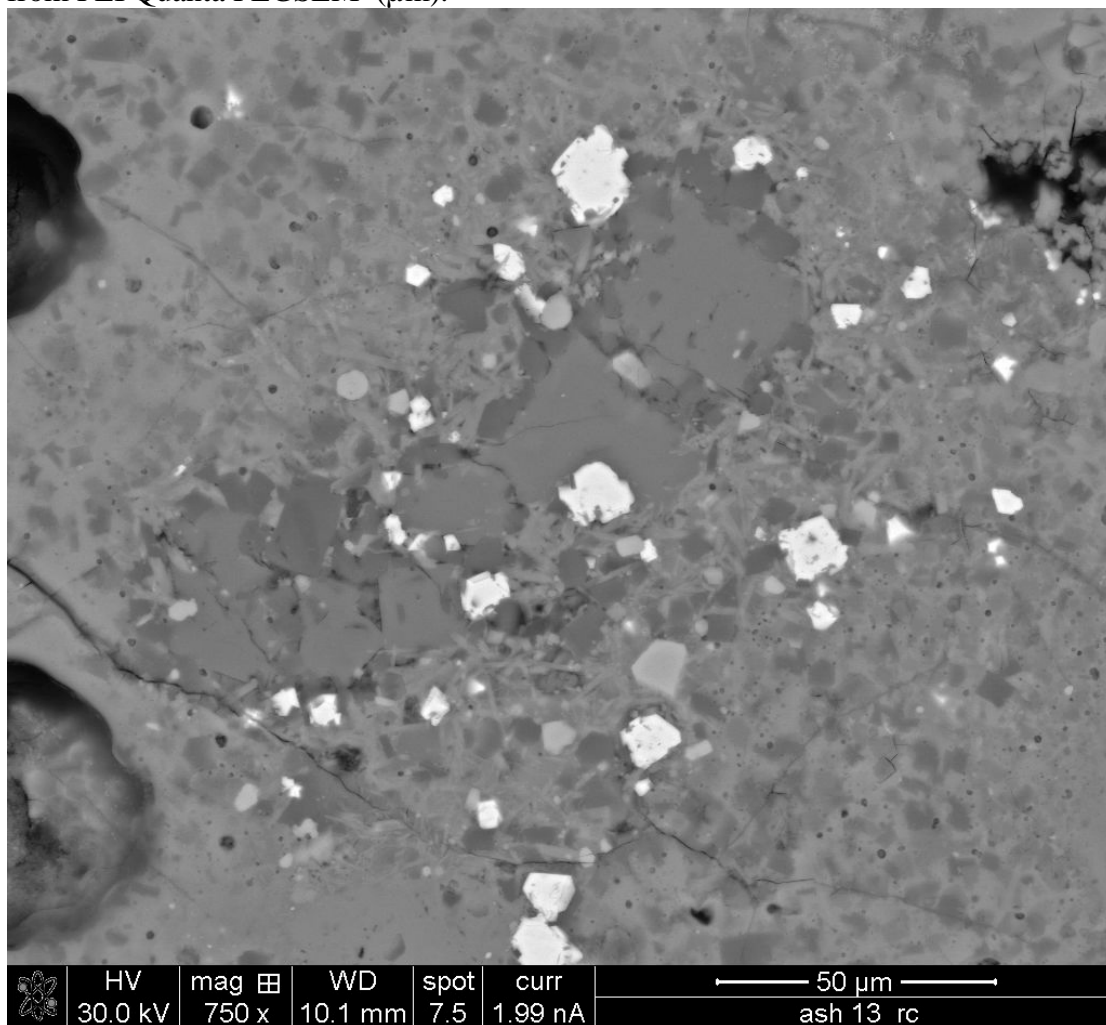


Figure 4e: BSE image of WN (wollastonite-nephelinite sample ASH-13) from FEI Quanta FEGSEM (μm).

Figure 5: OL2-A SEM BSE Images and Elemental Map for Al, Ti, Na, Fe and Ca

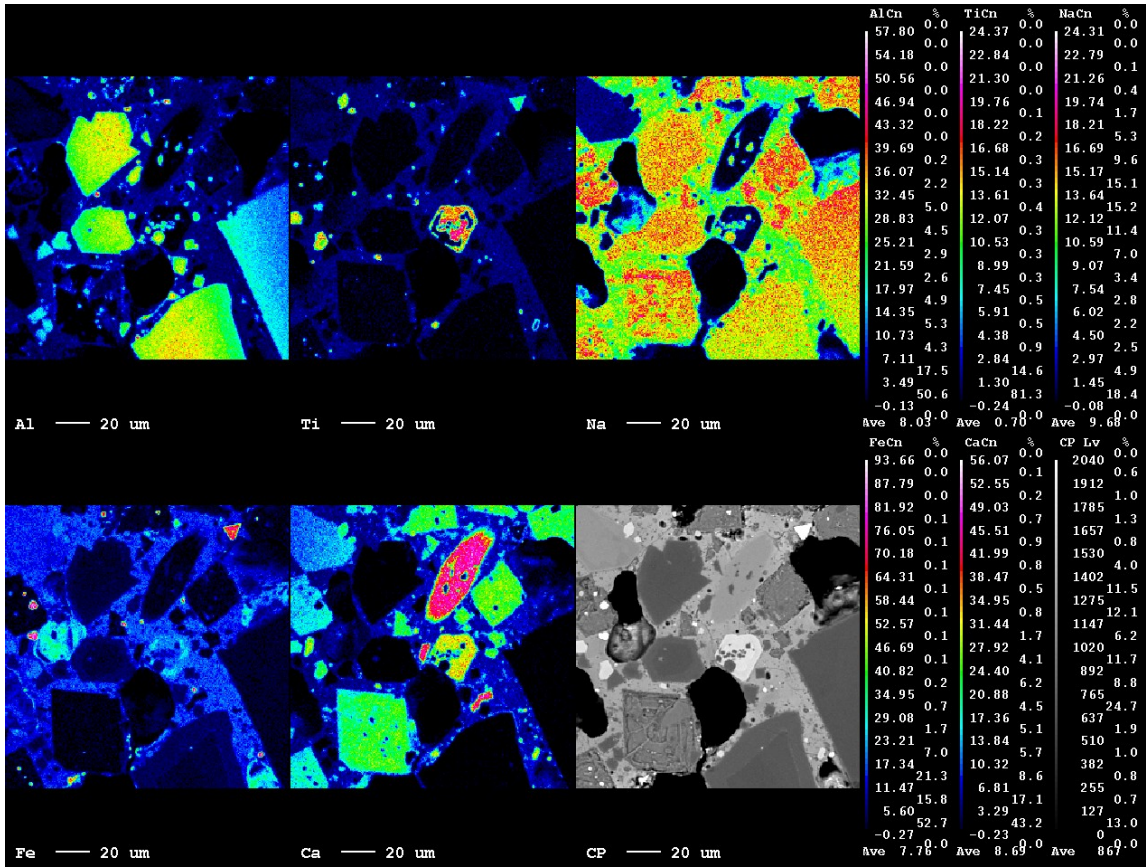


Figure 5: WDS generated images (Al, Ti, Na – top row left to right), Fe, Ca and backscatter electron image (bottom row left to right). Ti map has a combeite mineral grain in the center, with a defined Ti-enriched rim. Ca map demonstrates a wollastonite mineral grain (oblong pink colored crystal in upper center right position of Ca map) with distinctive compositional change from core to rim. Rim of

Combeite

Combeite ($\text{Na}_2\text{Ca}_2\text{Si}_3\text{O}_9$) was only found in the combeitic-wollastonite nephelinite (OL2-CWN) ash set, as seen the backscatter electron image of OL2 (Figure 4). Combeite mineral grains ranged in size from very small microlites of $<2\mu\text{m}$ (diameter on the shortest axis) up to $\sim 100\mu\text{m}$. Average combeite grain size was $40\mu\text{m}$. Mineral grains over $10\mu\text{m}$ all contained abundant inclusions of: nepheline, wollastonite, CPX, Ti-andradite, and a few apatite inclusions. Inclusions occurred primarily in a band approximately $8\text{-}12\mu\text{m}$ from the rim of the mineral grain. An average (non-microlite) combeite mineral grain from the CWN deposits would be $\sim 40\mu\text{m}$ in diameter and have at least 40 visible inclusions, the largest of which could be up to $10\mu\text{m}$ in diameter and the smallest $<1\mu\text{m}$. The core would be more homogenous and representative of the expected chemical formula ($\text{Na}_2\text{Ca}_2\text{Si}_3\text{O}_9$), whereas the rims (within $\sim 10\mu\text{m}$) would contain higher quantities of non-formulaic components such as Al, Fe, Mg and S. Resorption and an increase in inclusions is also seen on the rims of combeite mineral grains. Combeite microlites compositions mimics the composition of the rims larger grains, with less inclusions. In a core to rim analyses of a $100\mu\text{m}$ (diameter) combeite mineral grain the abundance of major oxides (SiO_2 , CaO and Na_2O (wt%)), were constant in the core of the mineral, and then dropped dramatically at a $20\mu\text{m}$ distance from the rim. SiO_2 dropped 12wt%, CaO dropped 20wt% and Na_2O dropped initially 10wt% then recovered 6wt% of that (Figure 6a). An analyses of the minor elements of this mineral grain revealed a very low concentration (under 0.5wt%) of SO_3 , TiO_2 , MgO, and K_2O , at the core of the grain. At the same distance ($20\mu\text{m}$) from the grain boundary as the major oxides were depleted, these minor elements increased dramatically SO_3 rose to 2.8 wt%, TiO_2 to 1.7wt%, and K_2O to 6wt%. MgO rose to 3wt% and then dropped back down to 1.7 wt%, all within 20

μm of the crystal rim (Figure 6a). Combeite rims (within 10 μm) had a much higher Si and lower Al (c.p.f.u) than the cores (rim and core values taken from 60-100 μm diameter grains, Figure 6c). In the combeitic-wollastonite nephelinite (OL2-CWN), the x-ray maps demonstrate mineral overgrowths as well, visible as change in Ca concentration in the combeite crystal rims (Figure 5), additionally, combeite rims exhibit a marked increase in Fe, Al, and Mg (figure 6b). A summary of mineral formula averages are summarized in Table 2. All raw elemental data, calculated mineral formulas, and normalized averages for each mineral and point analysis summarized can be found in Appendix DA summary of mineral formula averages are summarized in Table 2. All raw elemental data, calculated mineral formulas, and normalized averages for each mineral and point analysis summarized can be found in Appendix D.

Figure 6a-b: Combeite core to rim EMPA analyses showing variation in major and minor elements (oxide wt%)

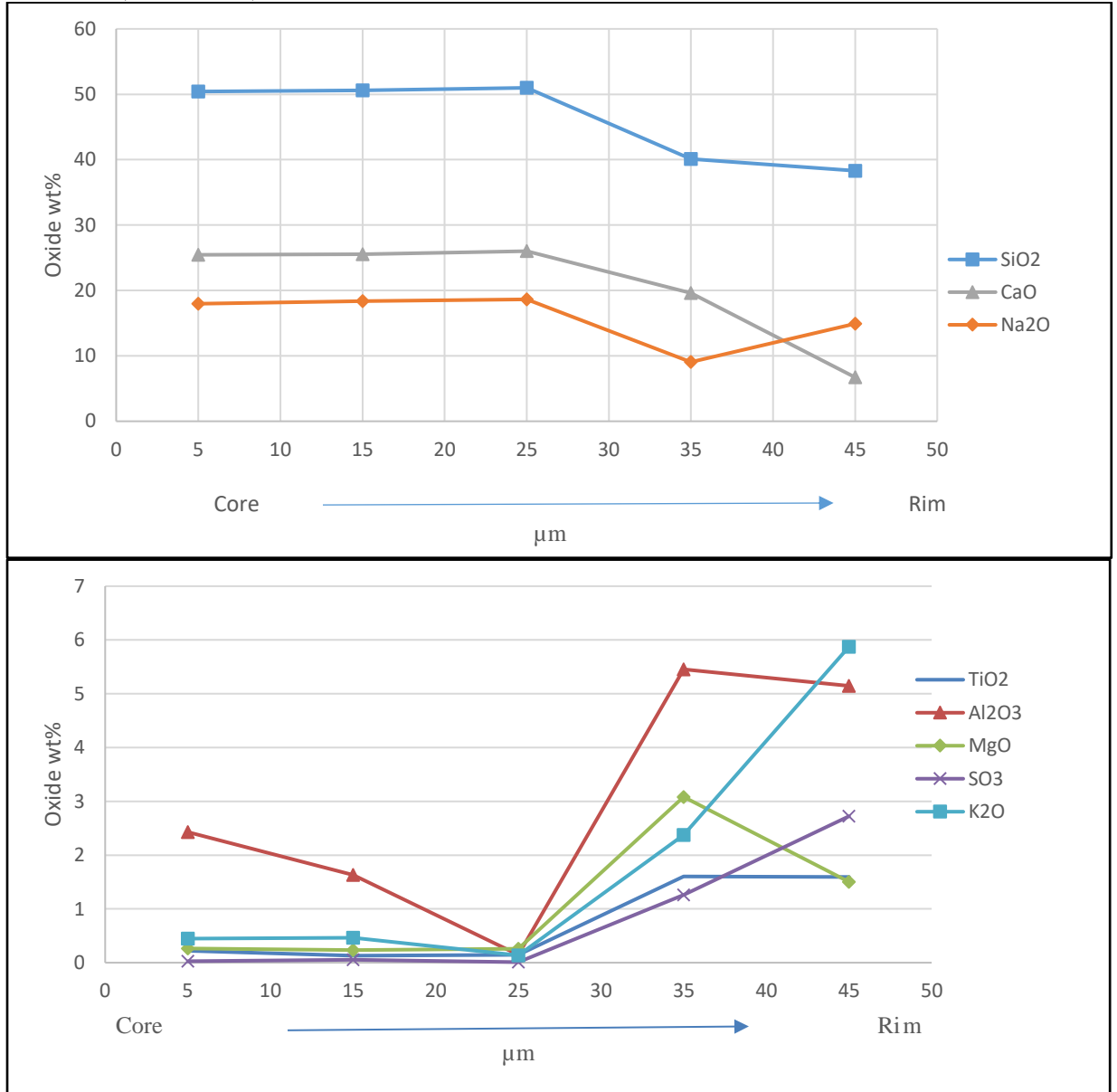
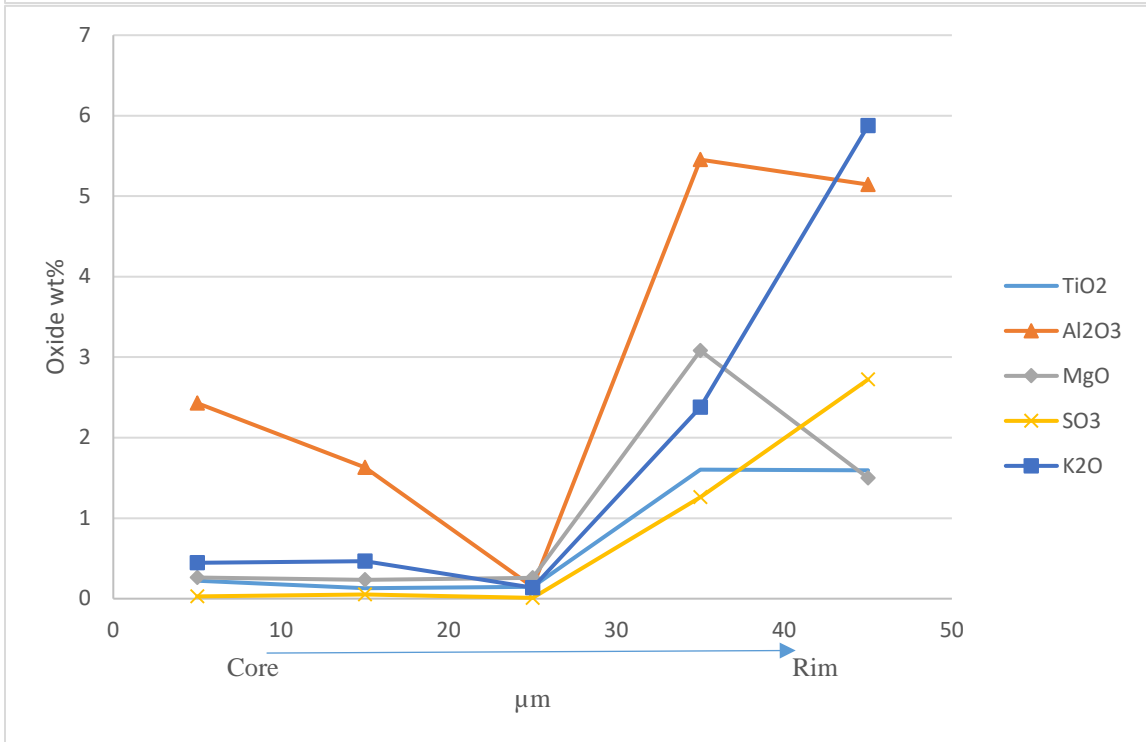
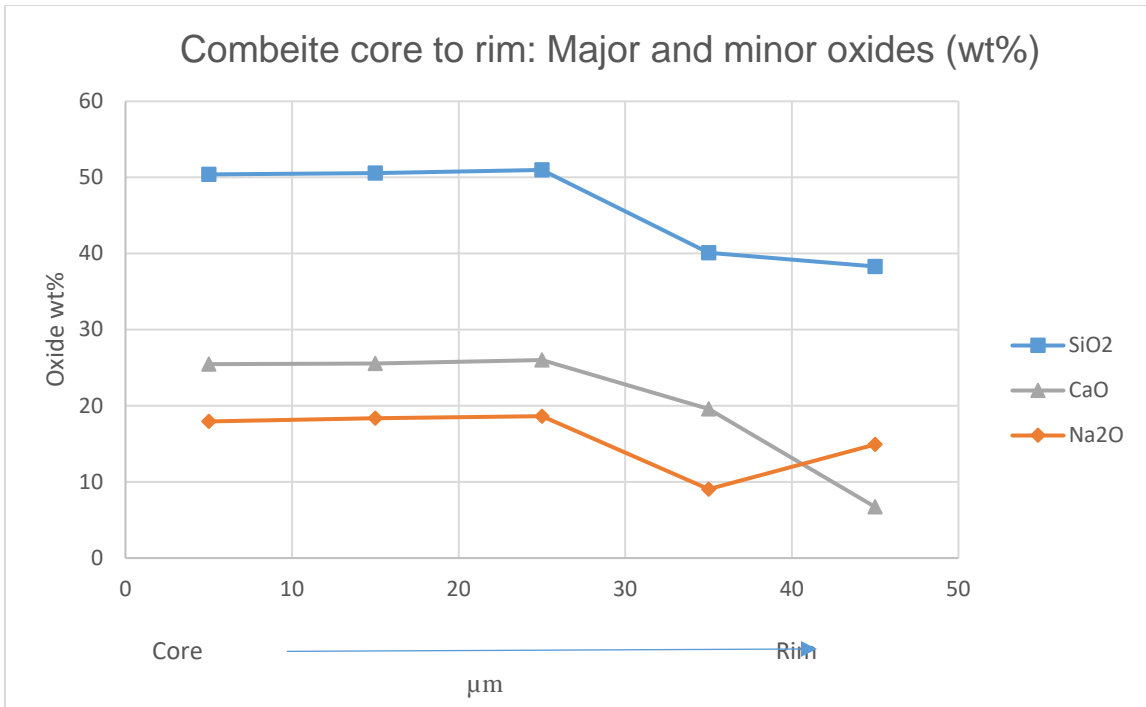


Figure 6a (top graph) : Major element oxide wt% on y-axis for OL2-G 100 μm combeite mineral grain, distance of analyses point from center of mineral grain on x-axis (μm). SiO₂- blue, CaO- green, Na₂O – red.

Figure 6b: Bottom graph: Minor element oxide wt% on y-axis for OL2-G 100 μm combeite mineral grain, distance of analyses point from center of mineral grain on x-axis (μm). TiO₂ – grey/blue, Al₂O₃ – red, MgO – green, SO₃ – purple, and K₂O – turquoise.

Figure 6a: Combeite Core to Rim EMPA Analysis (Majors and Minors)



OL2 core to rim combeite major and minor elements in oxide wt% plotted on the y-axis (see legend for oxide identification). The distance from the center of a 100μm wide combeite mineral grain (Figure 5) is plotted on the x-axis.

Figure 6c: Combeite Core to Rim EMPA Analysis (Si/Al)

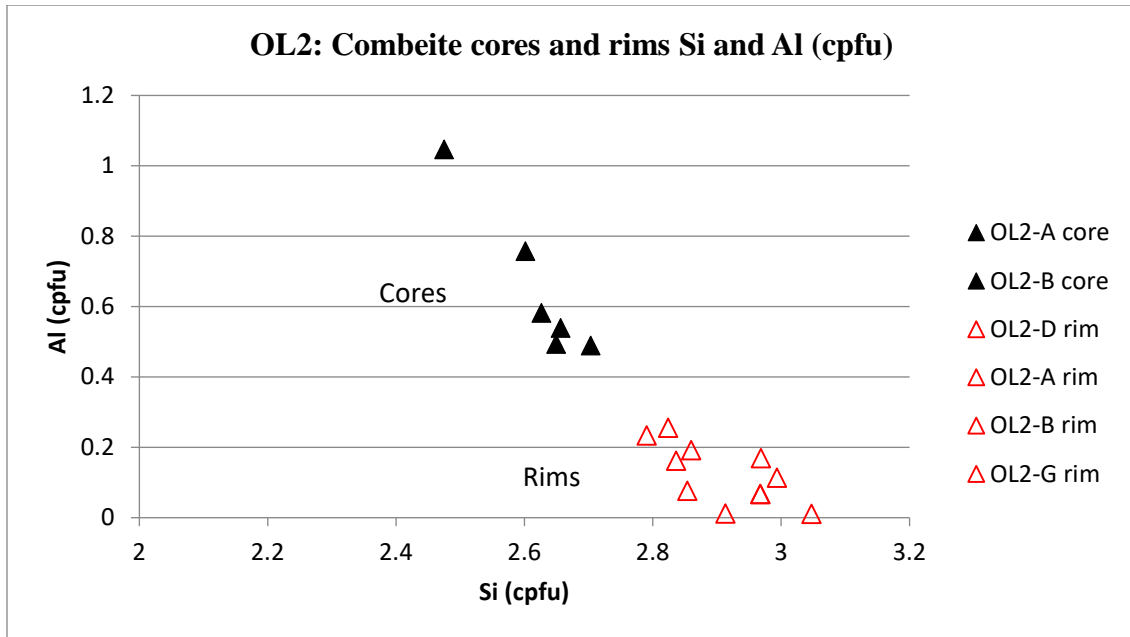


Figure 4c: OL2 combeite core and rim EMPA point analyses, Red triangles indicate analyses within less than 10 μ m of the rim of combeite mineral grains up to 100 μ m. Black triangles are from cores of combeite mineral grain sizes ranging from 50-100 μ m width. All samples from OL2 sample set, combeitic-wollastonite nephelinite.

CPX.

ASHES (WN- wollastonite-nephelinite) and OL2 (CWN- combeitic wollastonite-nephelinite) assemblages contained CPX. CPX grain sizes ranged from very small (<10 μm) to greater than 700 μm (diameter measured on the shortest axis). CPX mineral grains primarily exhibited heterogeneous cores, oscillatory zoning, Mg overgrowth, resorption rims and near complete resorption. Overall CPX compositional variability is plotted on the Wo-En-Fs pyroxene quadrilateral diagrams based on assemblage (10a) and core to rim variability (Figure 10b). The wollastonite-nephelinite (WN) assemblage is more diopsidic, more Mg enriched than the combeite-bearing assemblage (CWN)(Figure 10a). The core to rim zoning profiles of all CPX indicate an increase in SiO_2 , MgO, and MnO in the rims as compared to the cores (Figure 10b), with the rims (within 10 μm of crystal rim) displaying a more diopsidic, Mg-enriched composition, as opposed to the cores which were relatively Fe enriched.

A feature of interest in the glass rich, combeite-free, wollastonite-nephelinite assemblage (ASHES-WN) was presented by two large CPX phenocrysts (>500 μm , on the short axis). These two CPX phenocrysts from Figure 7 (sample name: ASH15-EQUIL) and Figure 8 (sample name: ASH15-DISEQ) exhibited compositional variability and distinct crystallization histories. The first phenocryst (Figure 7), is highly euhedral, with defined unresorbed rims, displays low overall Al content, with bands of increased Ti and Al content, a complex Fe, Ca and Na mottled core, and oscillation zoning of Fe and [Ti+Al]. Few (>20) visible inclusions ranging in size from <10-50 μm (on the shortest axis), Ti-andradite inclusions up to

30 μ m in diameter.

The second phenocryst (Figure 8), is non-euhedral, displays significant rim resorption, no visible zoning, low overall Al and Na content, with higher Al and Na content in the core, in addition to >100 visible inclusions, abundant nepheline inclusions ranging from <5-50 μ m (on the shortest axis), and multiple visible Ti-andradite inclusions up to 50 μ m in diameter, with for more inclusions as compared to the phenocryst in Figure 7.

Both ASH15 CPX phenocrysts compositions are plotted on the pyroxene quadrilateral diagram (Figure 10c), the Figure 8 CPX is more Mg and Ca enriched, whereas the Figure 7 CPX is more Fe enriched. From Figure 9, differences in composition of these two ASH15 CPX phenocrysts can be observed from the EMPA traverse analyses. TiO₂ wt% is the same at the core of both phenocrysts, in the CPX from Figure 7 (sample name: ASH15-EQUIL) TiO₂ wt% remains constant from core to rim, whereas in the CPX from Figure 8 (sample name: ASH15-DIS) it diminishes to near zero at the rim. SiO₂ content is on average 2 wt% higher in the Figure 8 CPX. FeO (Total) wt% ranged from 2-10 wt% higher (average 6%) in the Figure 8 CPX. MgO wt% was on average 4% higher in the CPX from Figure 8, and increased about midway from crystal core to rim in both samples. MnO was also higher in the CPX from Figure 8. CaO wt% was relatively constant for both samples. A summary of mineral formula averages are summarized in Table 2. All raw elemental data, calculated mineral formulas, and normalized averages for each mineral and point analysis summarized can be found in Appendix D.

Figure 7: CPX Phenocryst from wollastonite-nephelinite (ASHES-WN sample name: ASH15-EQUIL): EMPA BSE and x-ray maps for Al, Ti, Na, Fe, and Ca (elemental wt%)

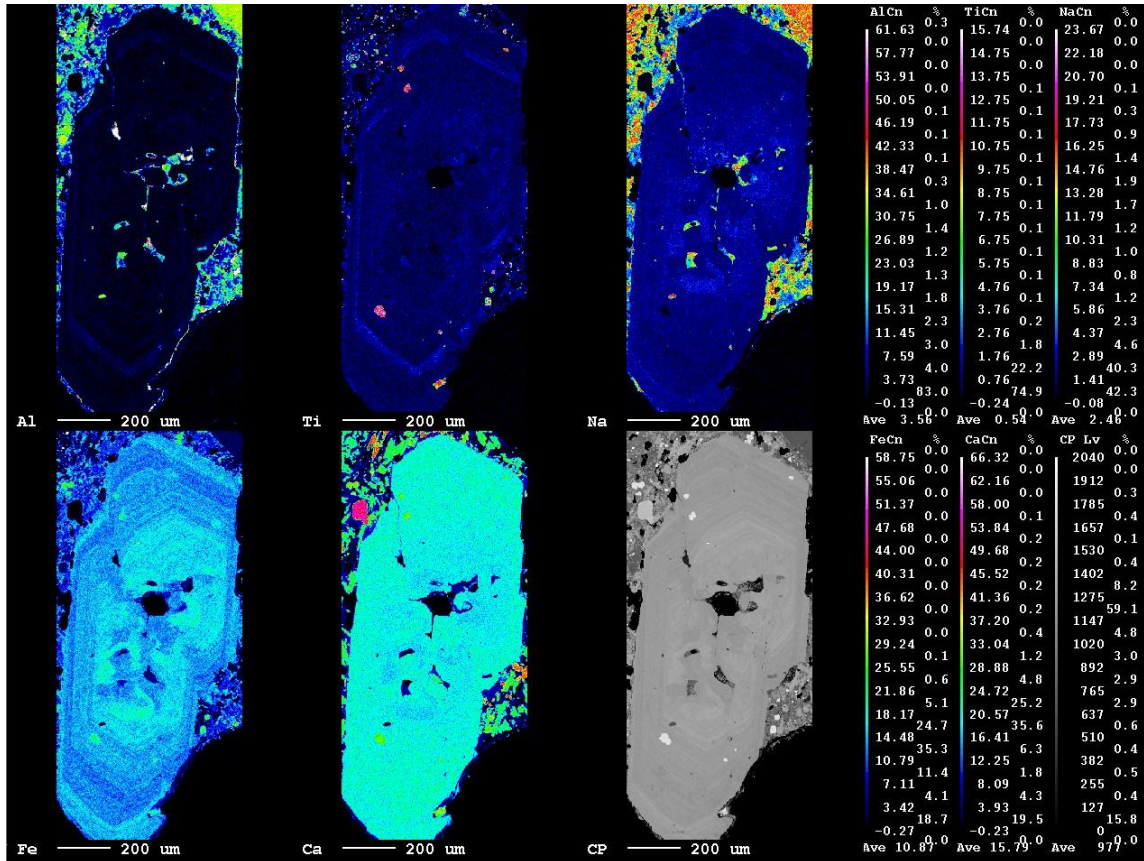


Figure 7: CPX from wollastonite-nephelinite (WN) assemblage. This phenocryst was found adjacent to the CPX phenocryst in Figure 8. Top row, left to right: Al, Ti, and Na. Bottom row: Fe, Ca and backscatter electron (BSE). Phenocryst displays low overall Al content, bands of increased Ti and Al content, Fe rich core, Fe, and (Ti+Al) oscillation zoning. Ti-andradite inclusions up to 30μm in diameter. Distinguishing features for mineral identification: **Ti-andradite**: Pink in Ti map, green in Ca map, and white in BSE map. **Nepheline**: Green in Al map, orange in Na map, dark grey in BSE map. **Wollastonite**: Orange in Ca map, **Apatite**: Pink in Ca map, white in BSE map.

Figure 8: CPX Phenocryst from wollastonite-nephelinite (ASHES-WN, sample name ASH15-DISEQ): EMPA BSE and x-ray maps for Al, Ti, Na, Fe, and Ca (elemental wt%)

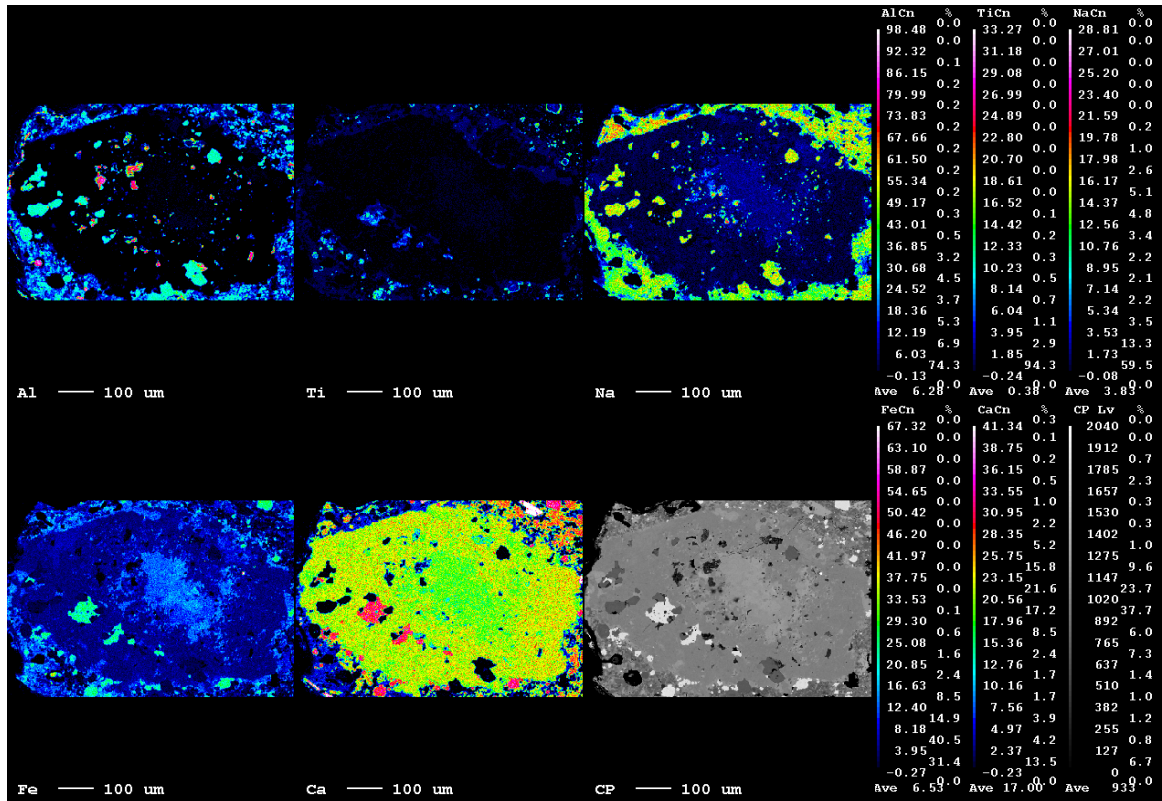


Figure 8: CPX (sample name: ASH15-DISEQ) from wollastonite-nephelinite (WN) assemblage. This phenocryst was found adjacent to the CPX phenocryst in Figure 7. Top row, left to right: Al, Ti, and Na. Bottom row: Fe, Ca and backscatter electron (BSE). Phenocryst displays low overall Al and Na content, with higher Al and Na content in the core. Abundant nepheline inclusions ranging from <5-50µm (on shortest axis), Ti-andradite inclusions up to 50µm in diameter. Distinguishing features for mineral identification:
Ti-andradite: Pink in Ti map, green in Ca map, and white in BSE map.
Nepheline: Turquoise in Al map, yellow-orange in Na map, dark grey in BSE map.
Wollastonite: Orange in Ca map,
Apatite: Pink in Ca map, turquoise in Fe map, white in BSE map.
 Abundant nepheline inclusions ranging from <5-50µm (on shortest axis), Ti-andradite inclusions up to 50µm in diameter.

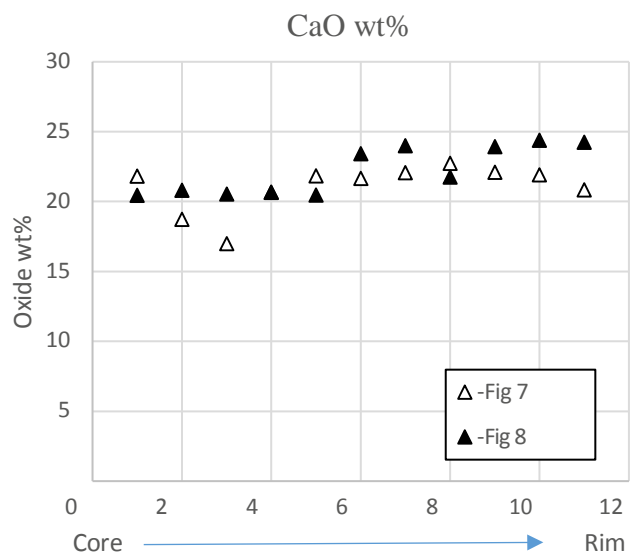
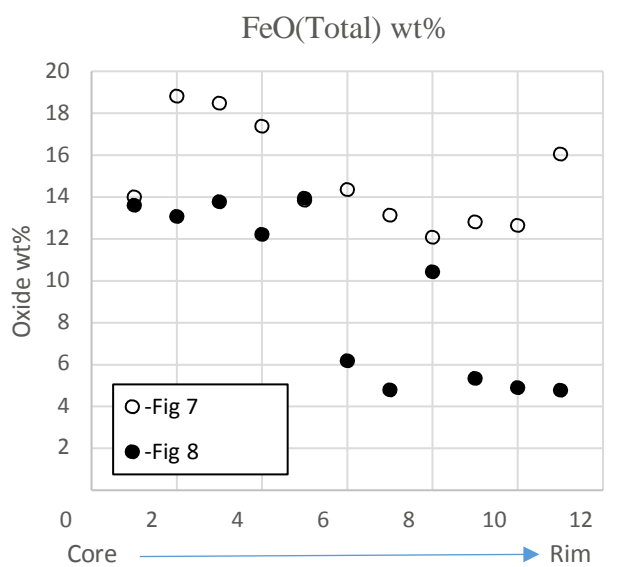
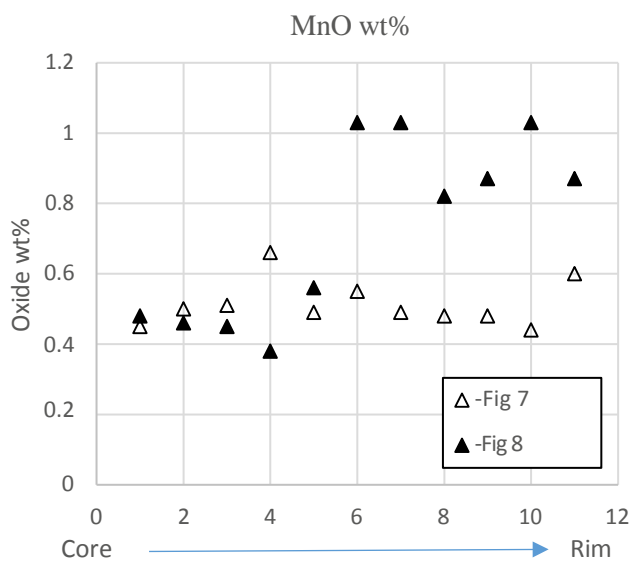
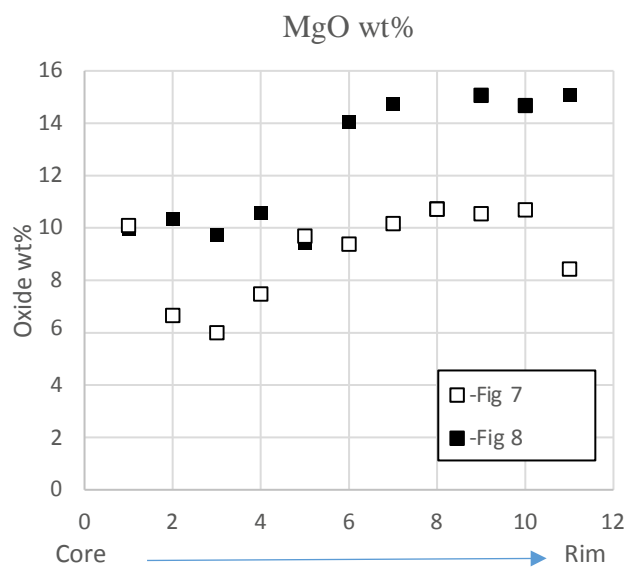
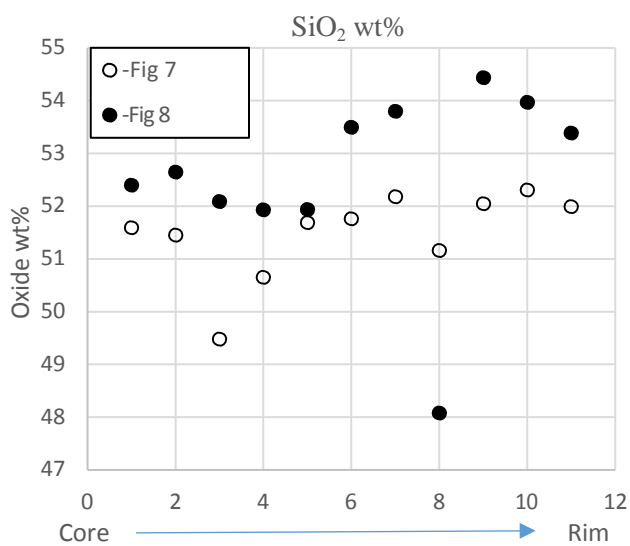
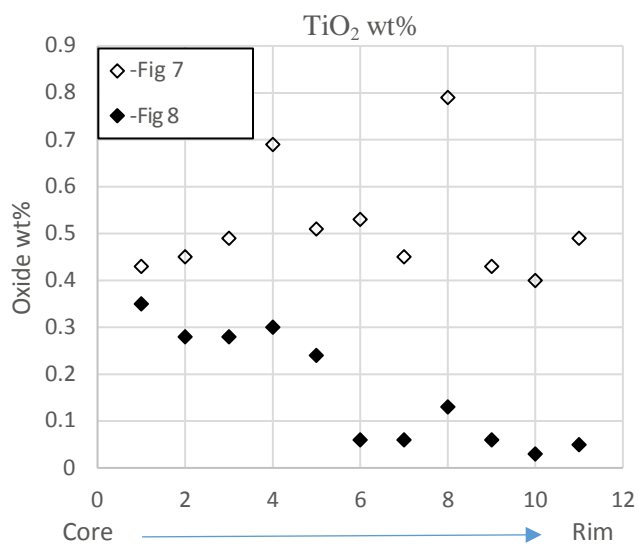


Figure 10a: CPX Compositions by Mineral Assemblage (ASHES-CWN and OL2-CWN)
Pyroxene Quadrilateral Diagram

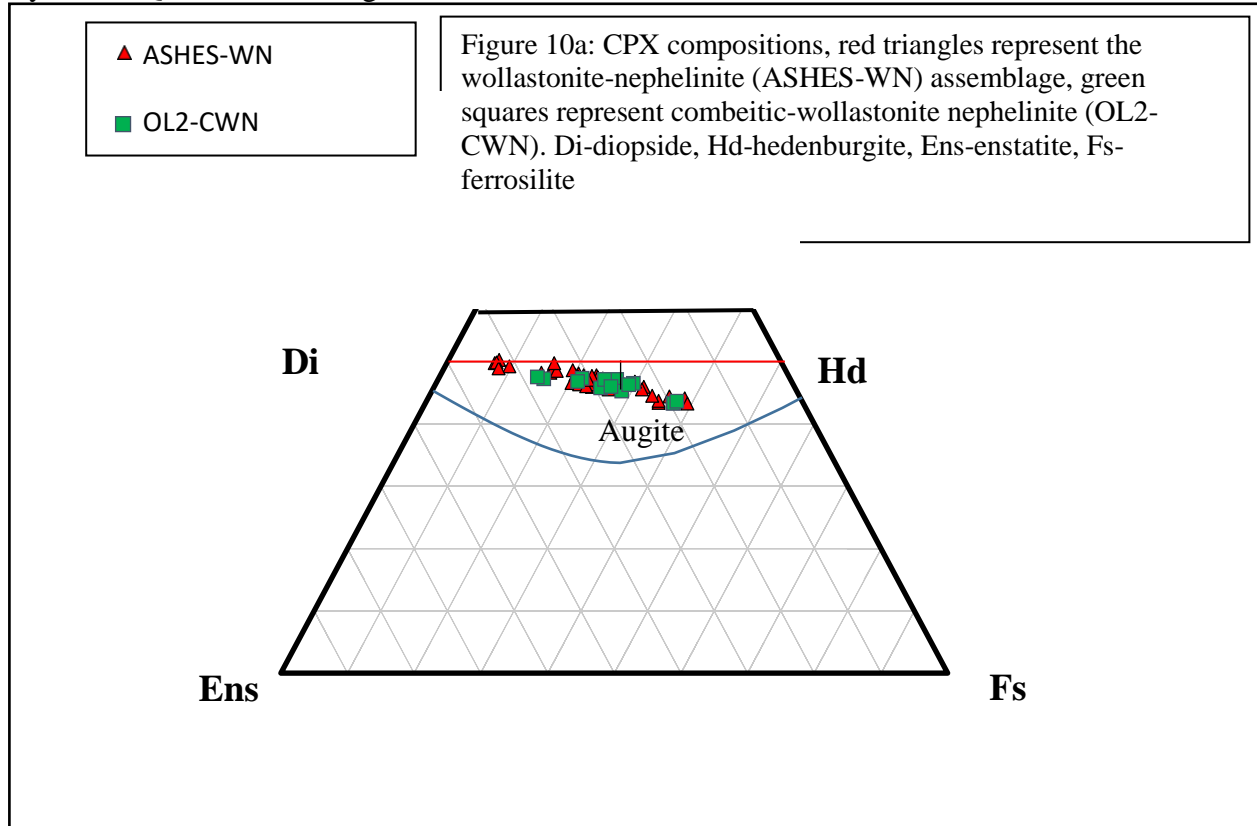


Figure 10b: CPX Compositions of Cores and Rims (within 10 μ m of grain boundary) of Large (>500 μ m diameter) Phenocrysts on Pyroxene Quadrilateral Diagram

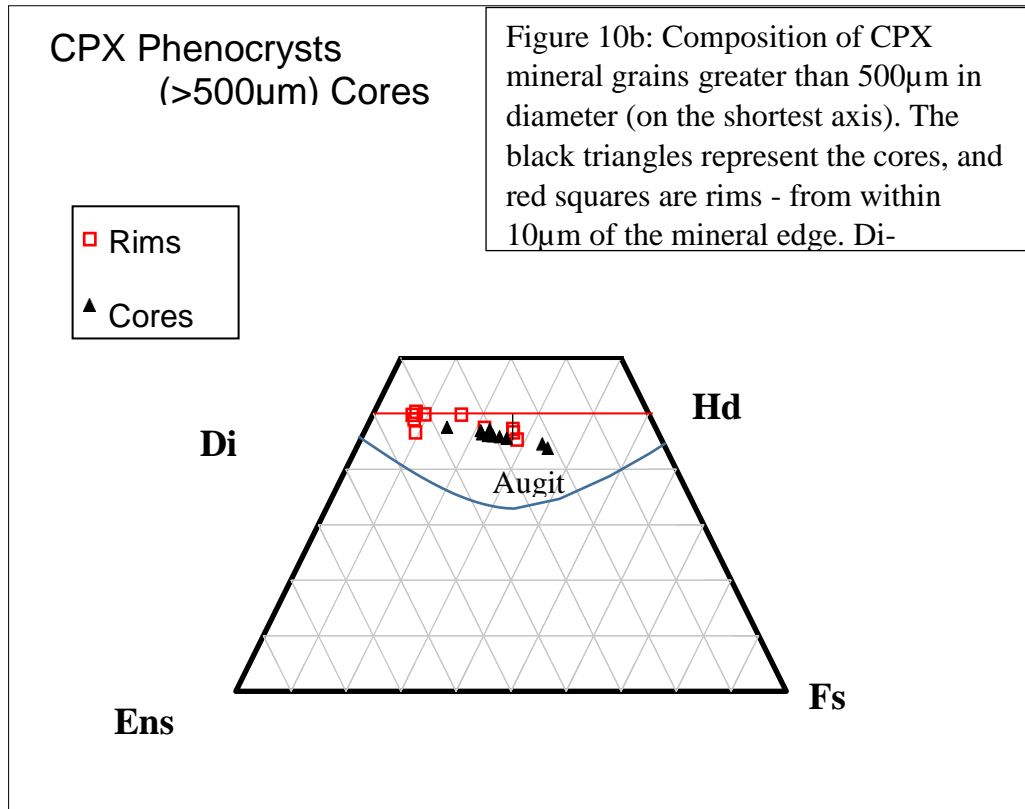
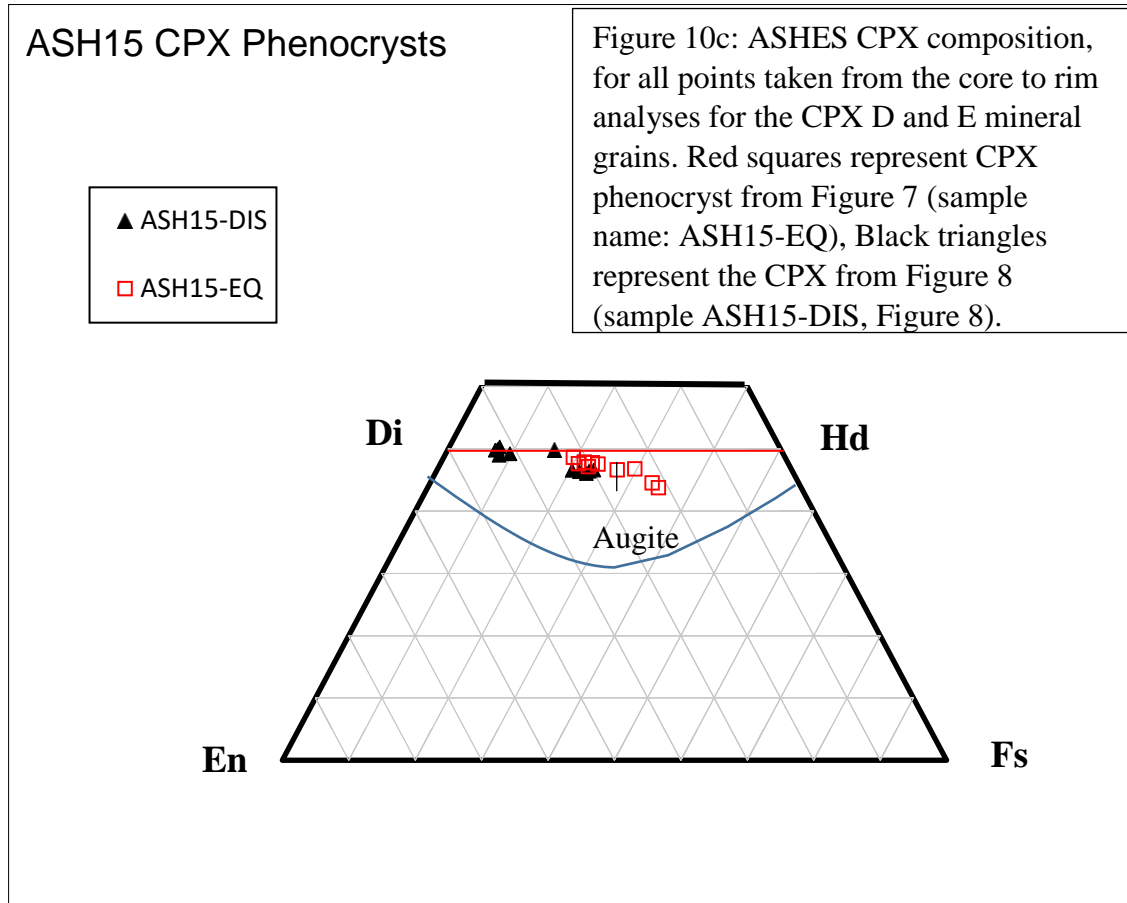


Figure 10c: CPX composition of ASH15 Phenocrysts from Figures 7 and 8 on Pyroxene Quadrilateral Diagram



Nepheline

Nepheline phenocrysts and mineral grains were primarily euhedral, free of resorption features, with relatively few inclusions. Additionally, there is a stepwise chemical boundary which can be observed in both large and small crystals, marked by FeO increase and an inclusion rich band. In Figure 4d the nepheline mineral grain (~45 μ m in diameter) displays step zoning, the rim is enriched in FeO (5 wt% increase) and MgO (from 0.0 wt% in core to 0.25 wt% in rim), visible inclusions are Ti-andradite. Nepheline grain sizes ranged from <5 μ m up to ~500 μ m in diameter (on the shortest axis).

Nepheline displayed the most constant composition of all minerals. The mineral chemistry demonstrated the most variability when compared by crystal size.

Nepheline EMPA analyses (Figure 11) were displayed according to crystal size as follows:

Rims (within 10 μ m of grain boundary) and small mineral grains (less than 15 μ m diameter on the shortest axis), followed by mid-sized (50-100 μ m diameter on the shortest axis), and the large group >100 μ m from each mineral assemblage (CWN and WN) were plotted on Figure 11. Although the variability was not large, there was a significantly larger MgO content in the rims and small mineral grains of both the combeite-wollastonite nephelinite (CWN) and the wollastonite-nephelinite (WN), and the CWN rims and small mineral grains had the highest FeO(Total) of all nepheline samples (~4% higher). The small (~15-25 μ m) nepheline inclusions in the large (>500 μ m) CPX from Figure 8 (ASH-15-DIS) have the highest MgO content

(Figure 11). Both nephelinite assemblages exhibited overgrowths to varying degrees.

The change in the nepheline composition occurs within ~10 μ m of the crystal rim (Figure 14b). In OL2 nepheline FeO wt% and MgO wt% mirrors this as both oxide values are higher within ~10 μ m of crystal rim and in microlites <15 μ m (figure 14b). The wollastonite-nephelinite (ASHES-WN) nepheline crystal chemistry demonstrates a higher MgO wt%, and stable FeO wt% throughout. Microlite composition of OL2 and combeite rim resorbtion in a highly vesiculated glass can be seen in the BSE image for OL2-F (Figure 14c). A summary of mineral formula averages are summarized in Table 2. All raw elemental data, calculated mineral formulas, and normalized averages for each mineral and point analysis summarized can be found in Appendix D.

Garnet: Ti-Andradite

Garnet (Ti-Andradite) was present in both nephelinite assemblages (CWN and WN), both euhedral (Figure 4a) and highly resorbed (Figure 4e) mineral grains, zoned (Figure 4a) and unzoned, with grains sized ranging from <5 μ m-400 μ m diameter on the shortest axis (Figure 4a). Figure 14a demonstrates significant rim resorbtion in multiple small (<50 μ m) garnets. Garnet composition, Ti-Andradite is closer to a moromoitite and schorlomite than andradite (Figure 12). Garnet composition from both mineral assemblages had very similar compositions, and little variability in mineral composition (Figure . Compositional variance was marked by assemblage; Si:Ti ratio (c.p.f.u) was higher for the wollastonite-nephelinite (ASHES-WN) sample set (the combeite-

free assemblage). In these garnets the Fe^{3+} content is inversely proportional to the Ti content. Fe content was also higher in the wollastonite-nephelinite (ASHES-WN)(Figure 13). A summary of mineral formula averages are summarized in Table 2. All raw elemental data, calculated mineral formulas, and normalized averages for each mineral and point analysis summarized can be found in Appendix D.

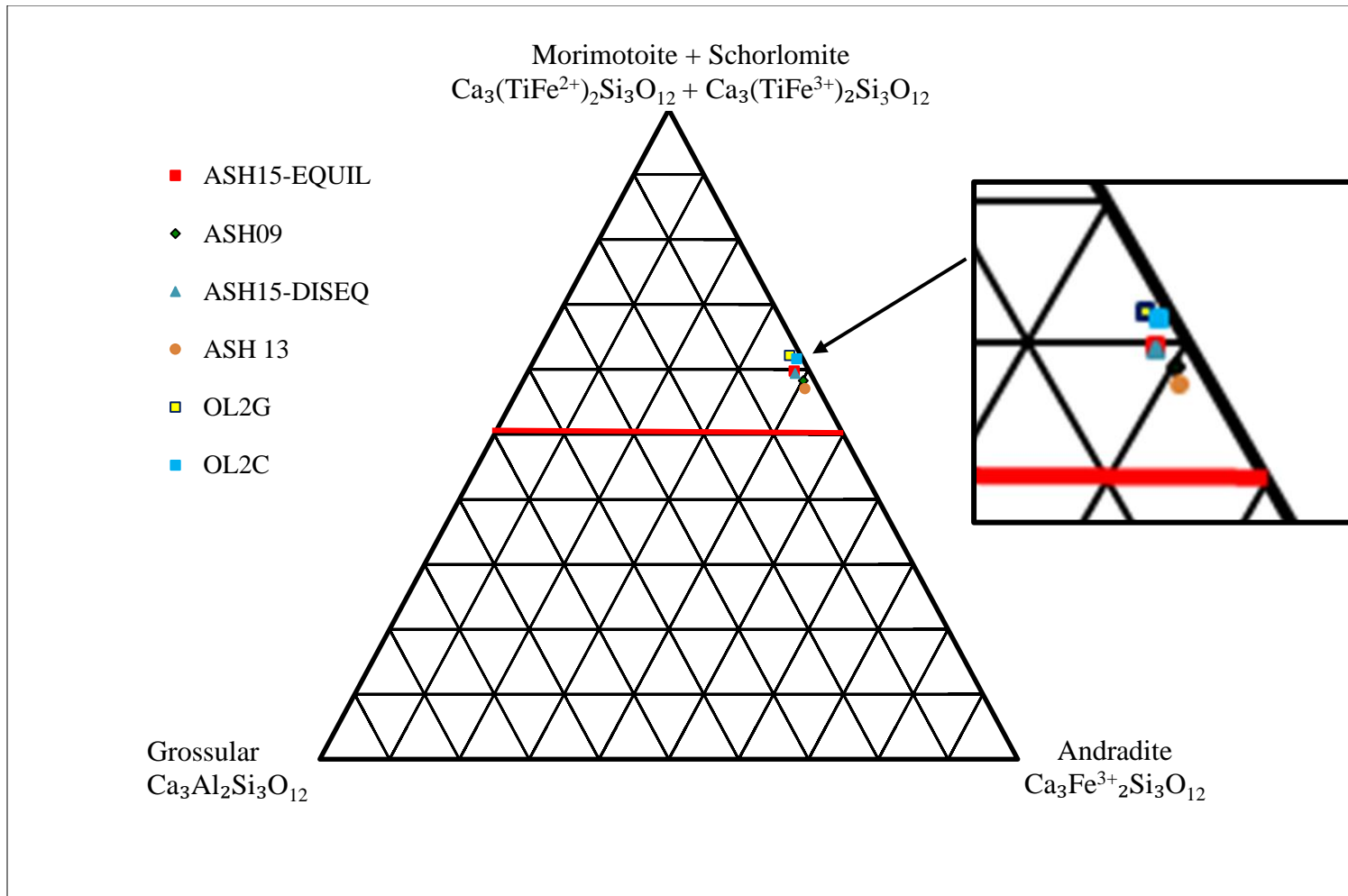


Figure 8: OL2 and ASHES garnet composition. CWN (combeitic wollastonite-nephelinite) is all samples prefixed with “OL”, WN (wollastonite nephelinite) are prefixed with “ASH”.

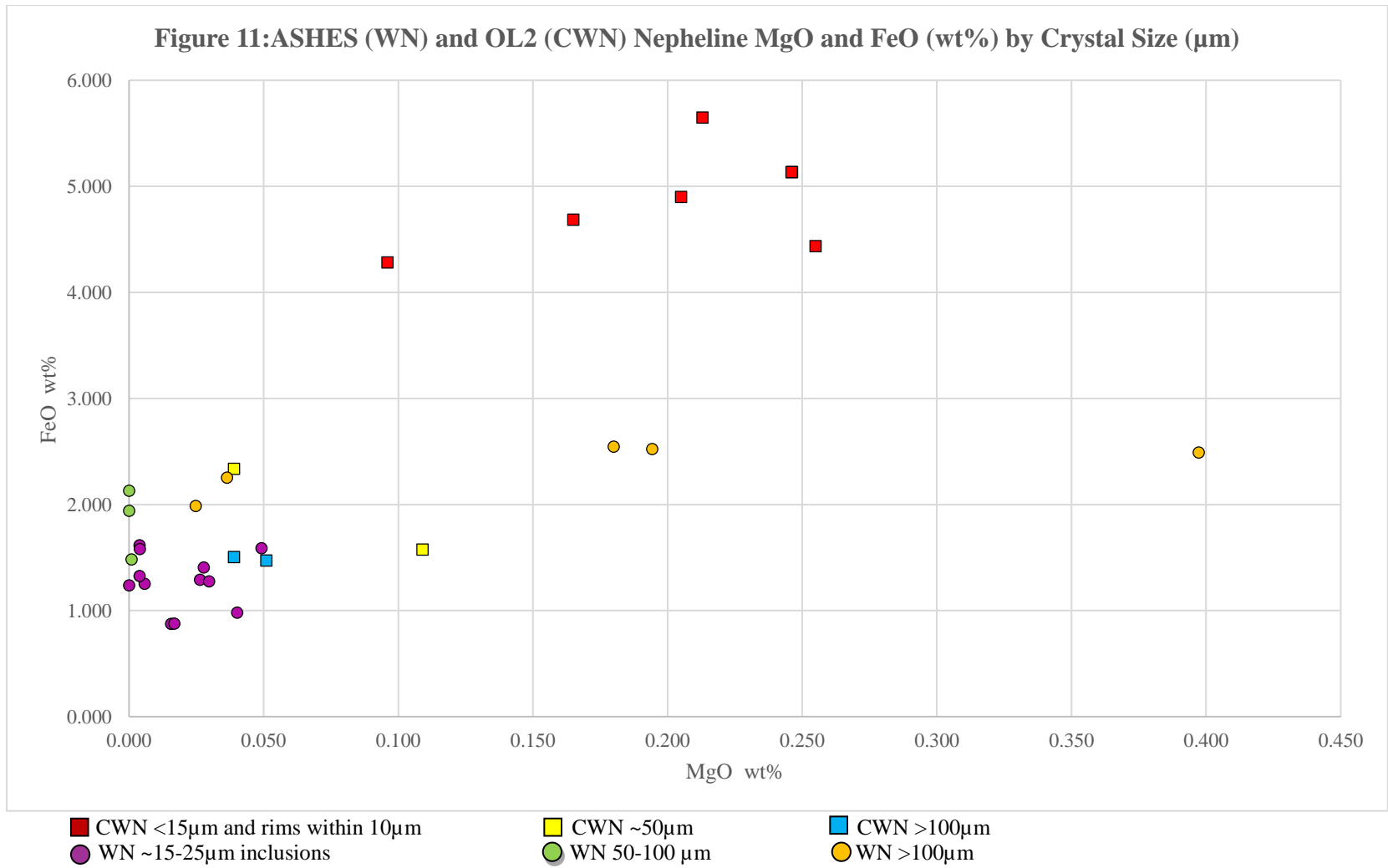


Figure 11: Nepheline FeO (oxide wt%) on the y-axis and MgO (oxide wt%) on the x-axis. Squares represent (OL2 combeite bearing nephelinite), and circles are from ASHES (non-combeite bearing nephelinite) mineral assemblage, with color variation for varying grain size (>15 μm , ~50 μm , <100 μm).

Garnet: Ti-Andradite

Garnet (Ti-Andradite) was present in both nephelinite assemblages (CWN and WN), both euhedral (Figure 4a) and highly resorbed (Figure 4e) mineral grains, zoned (Figure 4a) and unzoned, with grains sized ranging from $<5\mu\text{m}$ - $400\mu\text{m}$ diameter on the shortest axis (Figure 4a). Figure 14a demonstrates significant rim resorption in multiple small ($<50\mu\text{m}$) garnets. Garnet composition, Ti-Andradite is closer to a moromoitite and schorlomite than andradite (Figure 12). Garnet composition from both mineral assemblages had very similar compositions, and little variability in mineral composition (Figure . Compositional variance was marked by assemblage; Si:Ti ratio (c.p.f.u) was higher for the wollastonite-nephelinite (ASHES-WN) sample set (the combeite-free assemblage). In these garnets the Fe^{3+} content is inversely proportional to the Ti content. Fe content was also higher in the wollastonite-nephelinite (ASHES-WN)(Figure 13). A summary of mineral formula averages are summarized in Table 2. All raw elemental data, calculated mineral formulas, and normalized averages for each mineral and point analysis summarized can be found in Appendix D.

Figure 12: OL2 and ASHES Ti-Andradite Compositions

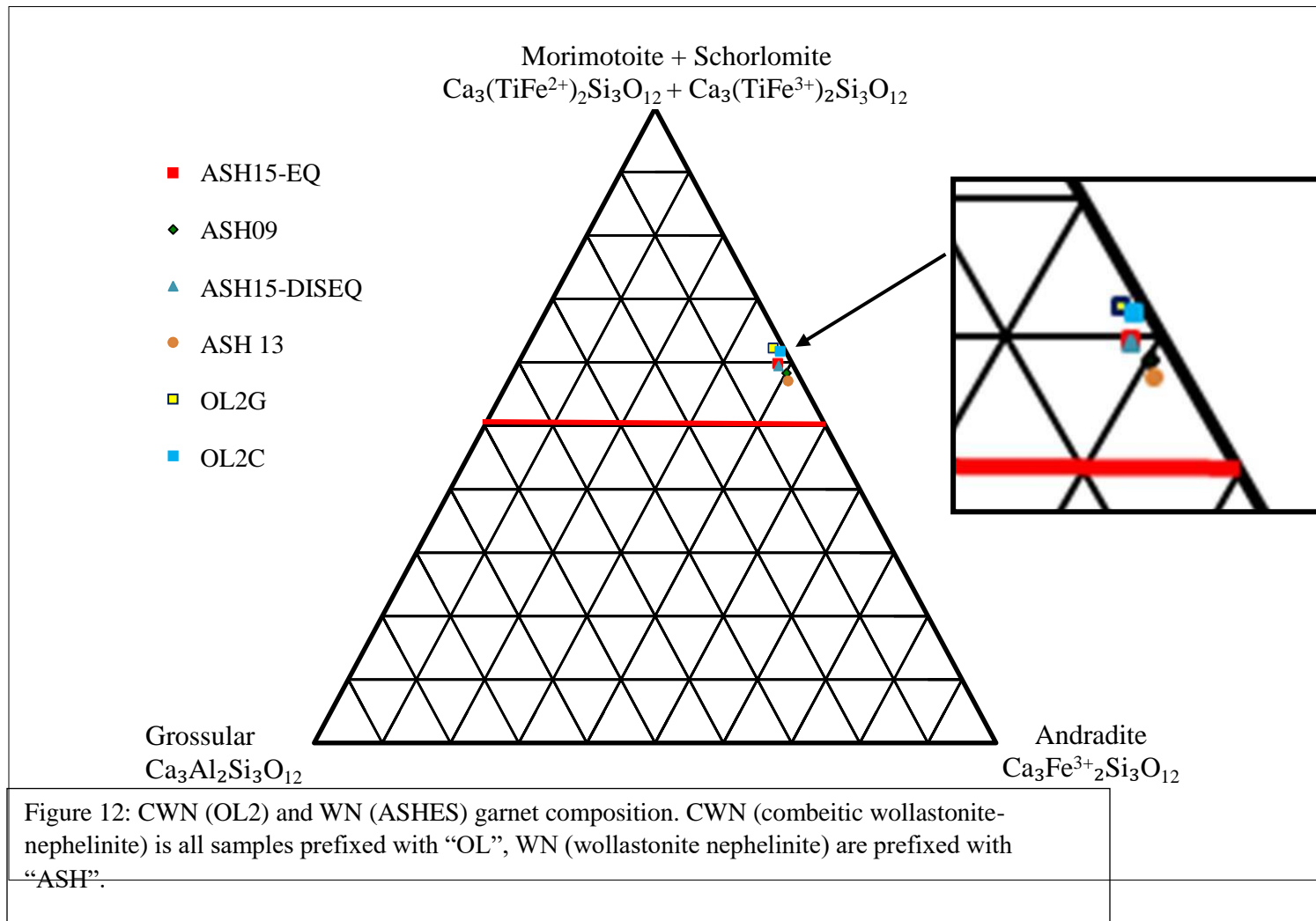


Figure 13: Ti- Andradite Major Cation Proportions Si/[Ti and Fe³⁺] (c.p.f.u O[12])

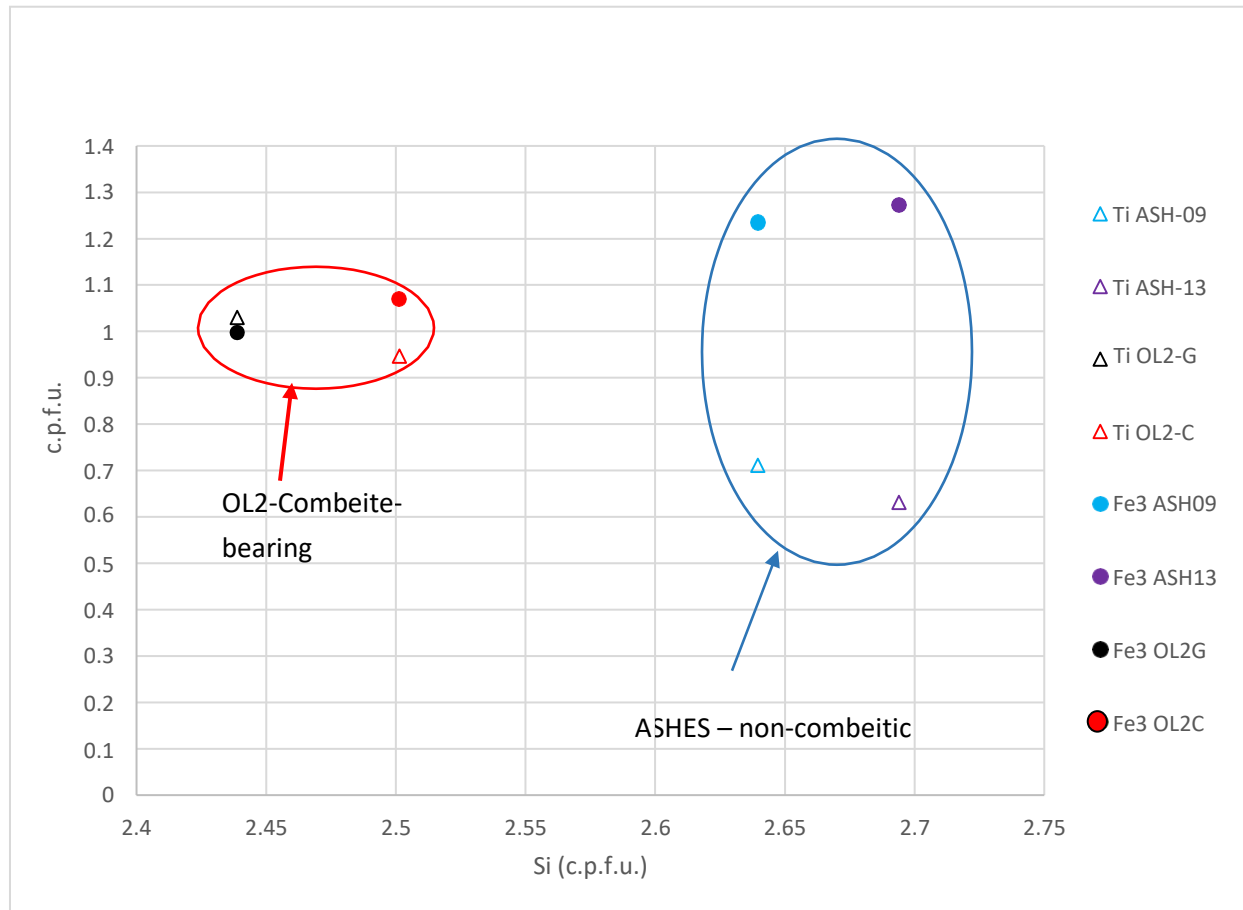


Figure 13: Andradite Ti (triangles) and Fe (circles) cation proportions for both assemblages. CWN combeitic-wollastonite nephelinite (OL2 -prefix in sample name) in red circle, WN- wollastonite nephelinite in blue circle. WN demonstrates significantly less Ti and more Fe than CWN andradites.

Figure 14a: Multiple Mineral Resorbption in Wollastonite-Nephelinite (ASHES-WN) SEM BSE Image (μm)

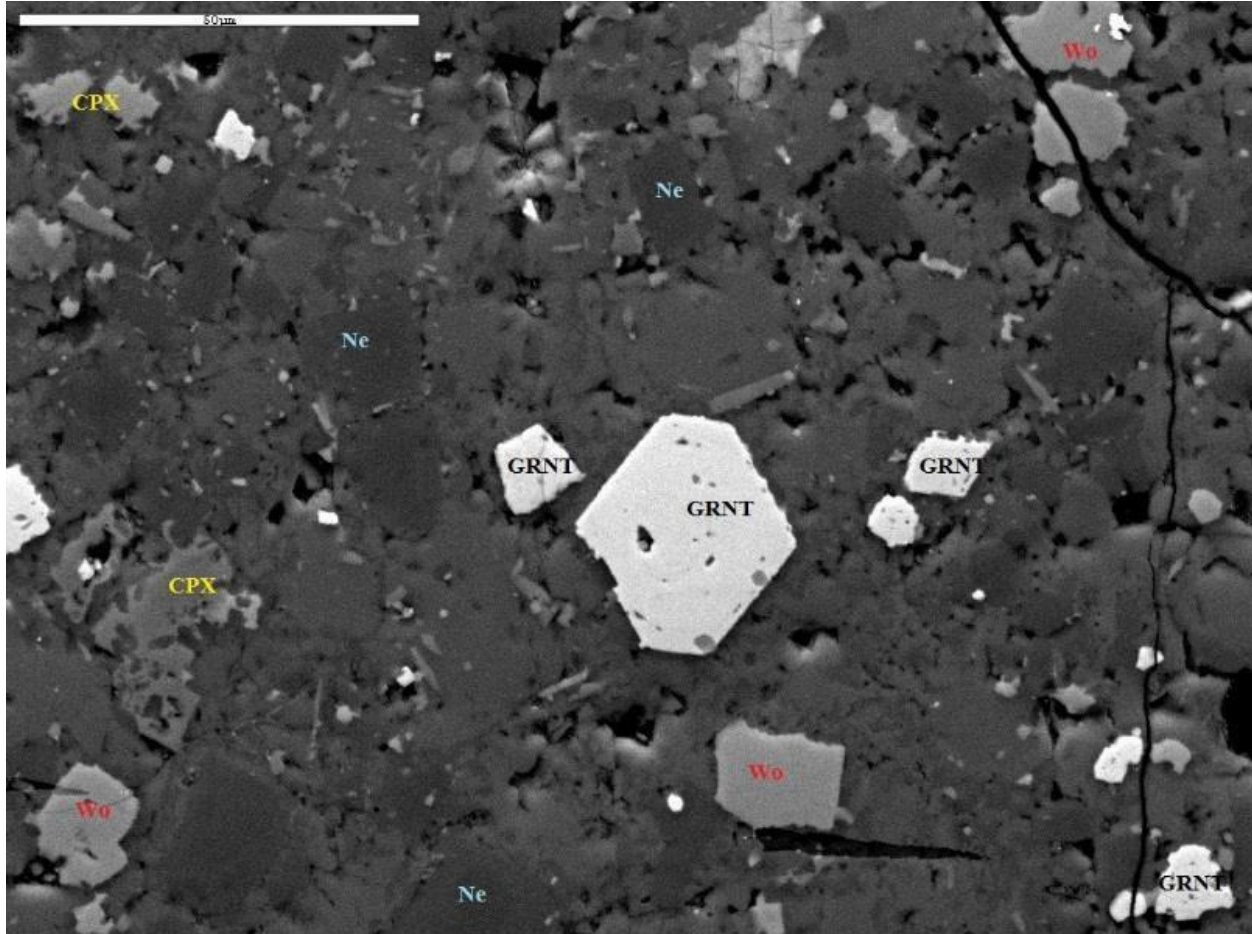


Figure 14a: Multiple mineral resorbption in wollastonite-nephelinite (ASHES-WN) exhibiting resorbption to varying degrees. Garnets (white mineral grains labeled 'GRNT') varying from fairly (largest garnet in center) to resorbed (lower right corner). Wollastonite (light grey, labeled 'Wo' in red print) also exhibiting resorbption (far upper right corner and lower left corner). Highly resorbed CPX (darker grey, labeled "CPX" in yellow print), nearly fully resorbed CPX (middle left)

Figure 14b: Mineral resorbtion and Zoning in combeitic-wollastonite Nephelinite (OL2- CWN)
EMPA BSE Image (μm)

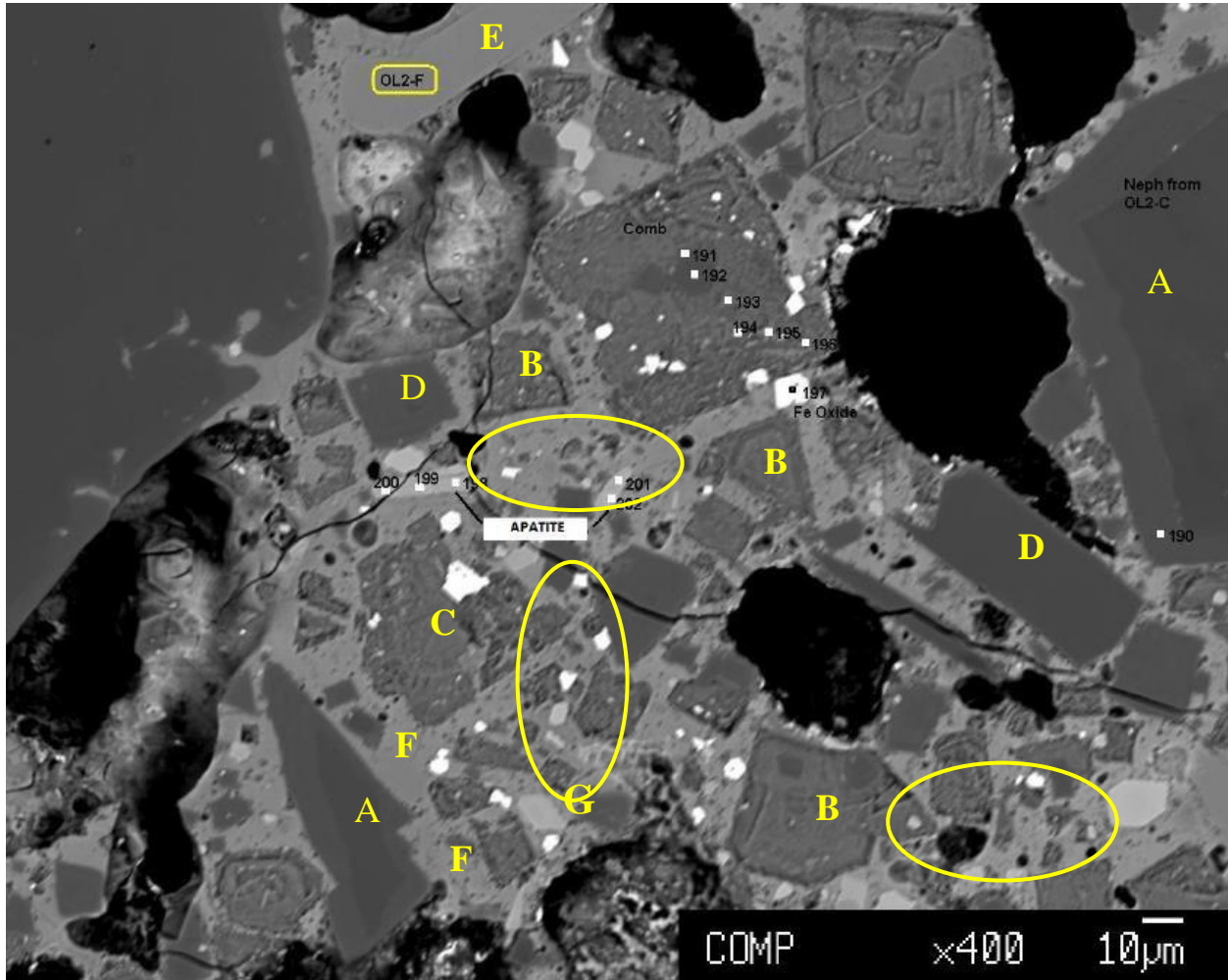


Figure 14b: Mineral resorbtion and zoning in combeitic-wollastonite nephelinite (OL2-CWN) with an abundance of smaller mineral grains ($5\text{-}30\mu\text{m}$ in diameter on the shortest axis), and microlites ($>5\mu\text{m}$ in diameter). A: nepheline mineral grains exhibiting step zoning within $10\mu\text{m}$ of grain boundary. B: Combeite mineral grains exhibiting overgrowth. C: combeite mineral grains exhibiting resorbtion. D: nepheline without zoning E: wollastonite, F: vesiculated glass G: Yellow circles indicate areas of abundant microlite mineral grains ($<5\mu\text{m}$ in diameter). Bright white mineral grains are apatite.

Figure 14c: Combeitic-wollastonite nephelinite (OL2-CWN) Glass Vesicles EMPA BSE Image (μm)

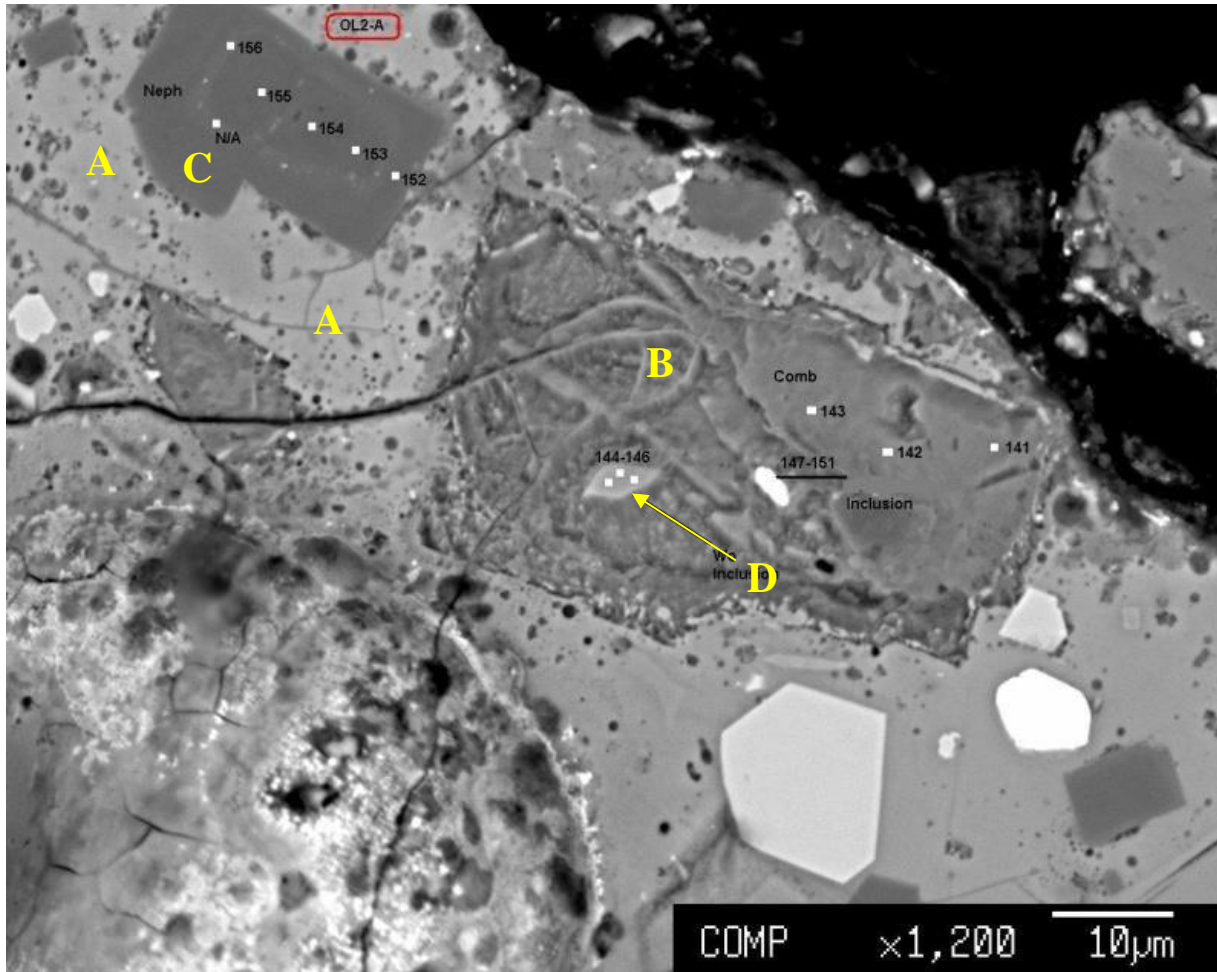


Figure 14c: Combeitic-wollastonite nephelinite (OL2-CWN) BSE image evidencing vesiculation, resorption and zoning. A: areas of glass evidencing vesiculation. B: combeite mineral grain exhibiting resorption. EMPA analyses points labeled on figure. C: nepheline with characteristic zoning coupled with inclusion band at chemical boundary. D: wollastonite inclusion in combeite

Glass and Microlites.

Glass abundance was higher by an order of magnitude in the wollastonite nephelinite (ASHES-WN) sample set as opposed to the combeite-bearing (OL2-CWN) assemblage (Figures 2 and 3). Combeitic-wollastonite nephelinite contained a greater abundance of small (10-30 μ m diameter on the shortest axis) and microlite (1-9 μ m diameter on the shortest axis) crystals. Glass vesiculation was observed in the combeitic-wollastonite nephelinite (OL2-CWN) in the samples in which combeite exhibited rim resorption and overgrowth (Figure 14c).

A comparison of images of the melt (Figures 4a-e and 14a-c) and the glass content as calculated by LispixTM (Figures 2 and 3) requires that the glass content calculations be qualified as follows: these values (WN-17% high, 11% mean, CWN-3% mean) is a low estimate which does not account for melt quench material which contains minerals of any kind. The mask generated for the glass phase, excluded mineral phases that had been already defined, therefore only represents pure amorphous melt – the portion of the melt that cooled as glass entirely. However, the large abundance of microlites and crystal mush texture that is visible in the BSE images, suggests that there was significant post-eruptive crystallization occurring in the ash deposits, and these microlites (Figure 14b) and crystalline groundmass may represent melt quench material which was excluded from the glass calculation, as per the Lispix phase map (Figure 2). The microlites and finer mineral material was primarily integrated into the total abundance for each mineral component (Figure 3).

Table 2: Normalized Mean Mineral Formulas (c.p.f.u)

Sample	Mineral [#]	Site	Si	Ti	Al	Fe ³⁺	Fe ²⁺	Mn	Mg	Ca	Na	K	Site Total
OL2-G	Ti-Andradite [12] Oxygens	Z	2.44	0.50	0.06								3.00
		Y		0.53		1.00	0.44	0.02					2.00
		X							0.13	2.87			
OL2-C	Ti-Andradite [12] Oxygens	Z	2.50	0.47	0.03								3.00
		Y		0.48		1.07	0.40	0.03					1.98
		X							0.07	2.95			
ASH-09	Ti-Andradite [12] Oxygens	Z	2.64	0.30	0.06								3.00
		Y		0.41		1.23	0.34						1.99
		X						0.03	0.05	2.93			
ASH15-DISEQ Inclusion	Ti-Andradite [12] Oxygens	Z	2.54	0.38	0.08								3.00
		Y		0.46		1.16	0.32	0.02	0.03				2.00
		X							0.05	2.95			
ASH15-EQUIL Inclusion	Ti-Andradite [12] Oxygens	Z	2.57	0.35	0.09								3.00
		Y		0.47		1.14	0.36	0.02					2.00
		X							0.08	2.92			
ASH-13	Ti-Andradite [12] Oxygens	Z	2.69	0.23	0.08								3.00
		Y		0.40		1.27	0.34						2.01
		X						0.03	0.04	2.92			
ASH-02	CPX [6] Oxygens	Z	1.98		0.00								2.00
		M2				0.22	0.30		0.47				0.98
		M1						0.02		0.82	0.18		1.02
ASH-09	CPX [6] Oxygens	Z	1.95		0.05								2.00
		M2		0.02		0.21	0.34	0.00	0.42				0.99
		M1								0.80	0.20		1.00
ASH-13	CPX [6] Oxygens	Z	1.89		0.10								1.99
		M2		0.03		0.15	0.22		0.59				1.00
		M1						0.01		0.89	0.10		1.01
OL2	CPX [6] Oxygens	Z	1.94		0.04								1.98
		M2		0.02		0.21	0.28	0.02	0.50				1.01
		M1								0.84	0.17		1.00
OL2	Wollastonite [3] Oxygens	Z	0.99		0.01								1.00
		Y				0.02		0.01	0.01	0.96	0.02	0.01	1.00
ASHES	Wollastonite [3] oxygens	Z	1.00										1.00
		Y				0.02		0.01	0.01	0.97			1.00
ASHES	Nepheline [4] Oxygens	Z	0.99		0.01								1.00
		Y			0.03	0.97							1.00
		X				0.03			0.04		0.21	0.75	1.03

Sample	Mineral	Site	Si	Ti	Al	Fe ³⁺	Fe ²⁺	Mn	Mg	Ca	Na	K	Site Total
OL2	Nepheline [4] Oxygens	Z	1.00										1.00
		Y	0.02	0.07	0.93								1.02
		X								0.01	0.75	0.23	0.99
OL2 (A-G Mean)	Combeite [9] Oxygens	Z	2.81	0.01	0.17								2.99
		Y			0.12		0.10	0.03	0.04	1.72	1.98	0.90	4.01

A summary of all oxide wt% can be found in Appendix C, and all mineral formula calculation tables in Appendix C.

Discussion

The results of this study reveal that the deposits of the 2007-8 pyroclastic eruption at Lengai are composed of two nephelinite assemblages, wollastonite-nephelinite (WN) and combeitic-wollastonite nephelinite (CWN). Both of which have been encountered in deposits at Lengai in the past, both the wollastonite-nephelinite (WN) and combeitic-wollastonite nephelinite (CWN) are of composition similar as erupted in 1993 (Dawson et al, 1994, 1996). The WN assemblage contains: nepheline, CPX, wollastonite, Ti-andradite, apatite and Fe oxides, CWN contains the same assemblage with the addition of combeite ($\text{Na}_2\text{Ca}_2\text{Si}_3\text{O}_9$). Both assemblages contain unique features such as zoning, overgrowth, resorbition and mineral instability.

The presence of two mineral assemblages, zoning, overgrowth, resorbition and other unique features (such as the two CPX phenocrysts from ASH15-WN,, Figures 7 and 8) of these eruptive ash deposits can explained by the injection of a deeper-sourced nephelinite magma (ASHES-WN) into a shallower more 'evolved' nephelinite magma (OL2-CWN), followed by a period of mixing and subsequent disequilibrium, triggering an eruption.

The two ash sample sets analyzed (ASHES and OL2) represent CWN and WN, although similar in composition, these two assemblages are differentiated by the following:

- The presence of combeite ($\text{Na}_2\text{Ca}_2\text{Si}_3\text{O}_9$) in CWN
- Relative phase abundances (Figure 3)

- Glass and microlite content (Figure 3, 14a, 14b)
- Combeite rims resorbed in CWN (Figures 14b-c) Al, Mg, and K rim overgrowth in CWN (Figure 6b).
- Resorption rims and near full CPX resorption in WN (Figure 14a)
- Mg and Fe rim overgrowth on nepheline from CWN (Figure 11, Figure 14b)
- CPX composition (higher Mg content) in WN (Figure 10b)
- Ti-andradite higher in Si and Fe content in WN (Figure 13)

The presence of these two distinct nephelinite compositions, in the ash deposits from this eruption can be explained by the injection of nephelinite from a deeper source, less peralkalinaline, relatively more enriched in Si, Al, Mg and Fe²⁺ (WN-ASHES sample set) into the highly evolved peralkalinaline magma enriched in Ti, Fe³⁺, Ca and Na from Lengai's central magma chamber (CWN-OL2 sample set). Initial SEM analyses provided several sources of mineralogical evidence that the WN (ASHES set) are from a deeper source than the CWN (OL2 set). The relative phase abundances of the two nephelinite assemblages in Figure 1 indicate that ASHES, the combeite-free assemblage, contains an order of magnitude greater glass content than OL2, the combeite bearing assemblage, which contains hardly any glass. It would be expected for a deeper magma to have higher temperatures, and therefore a higher liquid:crystal phase ratio, as seen in the wollastonite nephelinite (ASHES-WN).

In addition, the 2007-8 eruption at Lengai was uncharacteristically explosive, reaching plinian proportions (GVP, 2007-8). The assumed anhydrous nature (Sharygin, 2012) of the nephelinite magma at Lengai which was inferred primarily

from natrocarbonatite analyses, does not explain this highly volatile behavior. However the injection a deeper sourced, and therefore more volatile rich nephelinite would. The nepheline melt inclusions analyzed by De Moor et al, in 2013, were found to have up to 10 wt% H₂O, these samples came from the same ash layer that compose the wollastonite-nephelinite analyses from this study (ASHES-WN). This suggests the WN is not from Lengai's main magma chamber, which at ~3.3km depth would not be deep enough to stably maintain 10wt% H₂O in the melt, but from a deeper more volatile rich source. Mineral Chemistry and textures from this study support the premise that the WN deposits represent a magma from a deeper source and the CWN deposits represent the contents of Lengai's main nephelinite magma chamber known to historically bear combeite (Dawson 1995).

From the inclusion observations (Table 1) it is evident that combeite is the last phase to crystallize in the CWN (OL2) assemblage, as it contains inclusions from all phases: nepheline, CPX, wollastonite, and Ti-Andradite, whereas combeite was not observed as an inclusion in any mineral phases, this indicates that combeite was the last phase to crystallize in the CWN melt. If WN is the source of Lengai's nephelinite magma then combeite is a mineralization that occurs forming CWN from WN and probably occurs at the depths and temperatures of Lengai's main chamber, as CWN gets depleted of certain elements either through magmatic evolution or interaction with the natrocarbonatite.

It follows to infer that this deeper-sourced WN (ASHES) is the parental nephelinite for the Lengai magma chamber, then from the observed phase abundances (Figure

3) it can be suggested that combeite crystallizes at the expense of CPX at the pressure and temperature conditions of Lengai's magma chamber. This can be seen by comparing the phase abundances in the WN (non-combeite bearing ASHES) assemblage and the CWN (combeitic assemblage) (Figure 3), because all mineral phase abundances are fairly close to each other from one assemblage to the other except for CPX which is an order of magnitude lower in the CWN, and the addition of combeite to the CWN. For the WN (ASHES) deposits there was an average of 24% CPX, whereas in the CWN (OL2) deposits there was only 14% CPX, but there was 15% combeite. In contrast, for all other mineral phases the relative abundances were within 3% of each other for the two assemblages: nepheline (CWN-35%, WN- 33%), wollastonite (CWN-22%, WN- 25%), Ti-andradite (CWN-8%, WN-5%) (Figure 3). This suggest that as combeite becomes stable and crystallizes in the wollastonite-nephelinite forming combeitic-wollastonite nephelinite, the relative abundance of CPX in the melt decreases, but the other mineral abundances remain within 3% of each other. If CPX is no longer stable once combeite begins to crystallize that may explain why the CPX from the WN deposits exhibit degrees from resorbtion on the rims to near full resorbtion of a CPX grain (Figures 8 and 14a). This variability in features would have resulted during the period of injection of WN into CWN, and therefore the longer the WN melt interacted with the CWN the more resorbtion, reaction rims, overgrowth and mineral instability that is evidenced by the deposits.

The two nephelinite assemblages were also differentiated by glass content and microlite abundances. The mineral phase abundances from Figure 3 included

mineral grains as small as 5 μ m in diameter and therefore include much of the melt quench composition, the pure glass content from the Lispix phase maps (Figure 2), omitted vesicles, microlites and mineral grains 4 μ m and larger, and the pure glass content was on average 11% in the WN and 3% in the CWN, with the CWN displaying a highly vesiculated glass with an abundance of microlites between 2-5 μ m in diameter (Figure 14b), whereas the WN contains a nephelinite groundmass (Figure 14a). This supports the premise that CWN is Lengai's main nephelinite magma chamber (800° C, ~3.3km depth) assemblage as it would be more crystal rich and contain less liquid than its deeper (as inferred from volatile content), and therefore high temperature parental source (WN).

Combeite mineral instability is a result of recent changes in the surrounding melt resulting from WN mixing with the CWN. The combeite composition from the crystallized groundmass crystals with areas <400 μ m², demonstrate a change from the ideal magma conditions for combeite crystallization. The outermost point of the resorbed rim on this crystal had 0.95 Fe cations and only 0.47 Ca cation totals, indicative of Ca to Fe³⁺ substitution, in the last stages of crystallization. Combeite (Na₂Ca₂Si₃O₉) crystals demonstrate uncommonly high cation totals for [Fe +Mg] and Al (both non-formulaic elements) both as high as 1.0 per [9] Oxygens. The Fe-rich combeite rim composition indicates exposure to higher ratios of Fe and Mg in the CWN melt than available before. Percentage of [(Fe + Mg)/total cations] for the combeite crystallized under earlier and more ideal conditions is 1.8% and under the new conditions demonstrated by rim resorption 14.8%. These changes occurred within 25 μ m of the grain boundary (Figures 6a-b), and therefore may have

occurred over a period of time as the magmas were mixing prior to eruption, initially destabilizing the combeite mineral formula and then finally causing resorption when the abundance of WN mixed into the melt was increased just prior to eruption (seen as vesiculated glass around combeite mineral grain in Figure 14b). The increase Fe, Al and Mg in the combeite-wollastonite nephelinite (CWN) is from influx of the more primitive wollastonite-nephelinite (WN) into Lengai's main chamber (CWN).

Compositional zoning and overgrowth in the rims of minerals can be explained by the chemical interactions of WN magma (ASHES) mixing with the existing CWN magma chamber (OL2). Upon mixing, chemical changes in the surrounding melt are reflected in both assemblages. In the CWN, the Ca content of the melt is significantly lowered by the influx of WN, a magma richer in Si, Mg, Fe and Al, this is evidenced by the lowered Ca content on the rims of CWN minerals: wollastonite, nepheline and combeite rims in the Ca map on Figure 4. In addition, CWN (OL2) demonstrates a late stage increase in available Mg and Fe (Figure 12). This trend of increased Mg and Fe is also apparent in the combeite core to rim point analyses (Figure 6). Change in the melt chemistry of both melts is indicated by in the CWN assemblage by the Mg overgrowth on combeite (OL2-A, Figure 14b), which additionally exhibit increased Al and Fe within $<10\mu\text{m}$ of the rim (Figure 6). This implies combeite which was previously stable in the conditions of the CWN magma, becomes unstable when the WN (being more glass-rich and therefore less viscous) becomes the primary influence in the new conditions of the magma chamber providing a higher availability of Si, Al, Mg and Mn. (Figure

14a). Combeite rim zoning and overgrowth are indicators of a Si, Al, Mg and Fe rich melt (WN) changing the composition of the surrounding CWN melt enough to destabilize the combeite mineral stability field (Figures 6a and 6b). If the mixing of WN into CWN was initially gradual over a period of time this could result in the mineral overgrowth on rims of combeite as it adjusts to the new melt chemistry. Then if there was a sudden increase in the WN content in the surrounding melt then combeite can no longer stabilize and resorption takes place.

Evidence in support of the hypothesis that the deeper sourced WN magma is mixing with and supplying additional Si, Al, Mg, and Fe to the CWN melt of Lengai's main chamber is present in the nepheline, CPX, and Ti-andradite. Nepheline composition demonstrated difference by assemblage, compositional variability from core to rim and by grain size, all indicative of changes in the melt chemistry. Much like combeite from CWN, nepheline MgO and FeO concentrations exhibit a definite trend from low MgO and FeO wt% in larger crystals to higher values in the microlites (up to 25 μ m) and within 10 μ m of a crystal rim (Figure 11). In contrast larger (>100 μ m) nepheline crystals in the WN had relatively high FeO content, as compared to nepheline crystal of the same size from the CWN deposits (Figure 11). Large nepheline phenocrysts demonstrated zoning (Figure 14b) as well, with a clearly visible compositional change within 10 μ m of the grain boundary. In the combeite-bearing assemblage (CWN-OL2), nephelines exhibit zoning (within 10 μ m) with inclusions, and an inclusion band associated with the onset of zoning (Figure 14b). The minor elements, Fe and Mg are in low concentration in the larger phenocrysts (>100 μ m) and higher in the

microlites (<15 μm) and rims (within 10 μm of edge). The larger (100-250 μm) phenocrysts contain ~0.05% MgO wt% and up to 1.5 FeO wt%, whereas the microlites and rims contain 0.25 wt% MgO and 4.3 – 5.7 wt% FeO respectively. Similarly, higher FeO and MgO wt% was found in groundmass and rim analyses by Dawson et al (1998). Microlites (<15 μm) and small crystals (<50 μm) in the combeite-bearing assemblage have a visible compositional change within 10 μm of the rim.

CPX and Ti-andradite both also contain textural and compositional evidence of magma-mixing. Texturally, the CPX in WN (ASHES) exhibits the most resorption features (Figure 8), even nearly fully resorbed CPX (Figure 14a). Compositionally this can be seen by the trend of Mg enrichment in the rims of CPX phenocrysts from CWN melt, shown in the CPX quadrilateral diagrams (Figures 10a-c), as the compositional trend for the CPX rims to be more diopsidic than the cores (Figure 10a). Ti-Andradite also exhibits resorption (Figure 14a) in the WN, and zoning in the CWN (Figure 14c). Resorption occurs when the compositionally different, hotter, less viscous (higher glass, lower crystal content) WN (ASHES) magma comes in contact with minerals from the CWN more evolved melt. Ti-andradite mineral composition (Figure 13) differs substantially in the Ti and Fe content. These elements are inversely correlated in these garnets as seen in the cation proportion figure (Figure 13). Ti-andradite from CWN was higher in Ti and lower in Fe^{3+} than in the WN. Ratio of $\text{Ti}:\text{Fe}^{3+}$ was typically around 1, whereas for WN it was closer to 0.5. Ti-andradite from WN has much higher Fe content than Ti-andradite from WN, which supports the idea that WN is the source of the influx

of Fe in the CWN melt, additionally that these garners crystallize in different magmatic conditions. CPX and Ti-andradite texture and compositions support magma-mixing is behind the features observed in the deposits. All the apparent chemical instabilty, disequilibrium (zoning, overgrowth), and vesiculation in these magma are indicators that the 2007-8 eruption occurred as a result of magma-mixing of CWN and WN prior to (and during) eruption.

Pressure estimates for depth of the magma chamber(s) is still uncertain since attempting to use the CPX Al-geobarometer has an associated estimated error of 1.75-2.00 kbar (Nimis and Ulmer, 1998) and therefore does not provide any valuable information on pressure for the system.

Conclusion

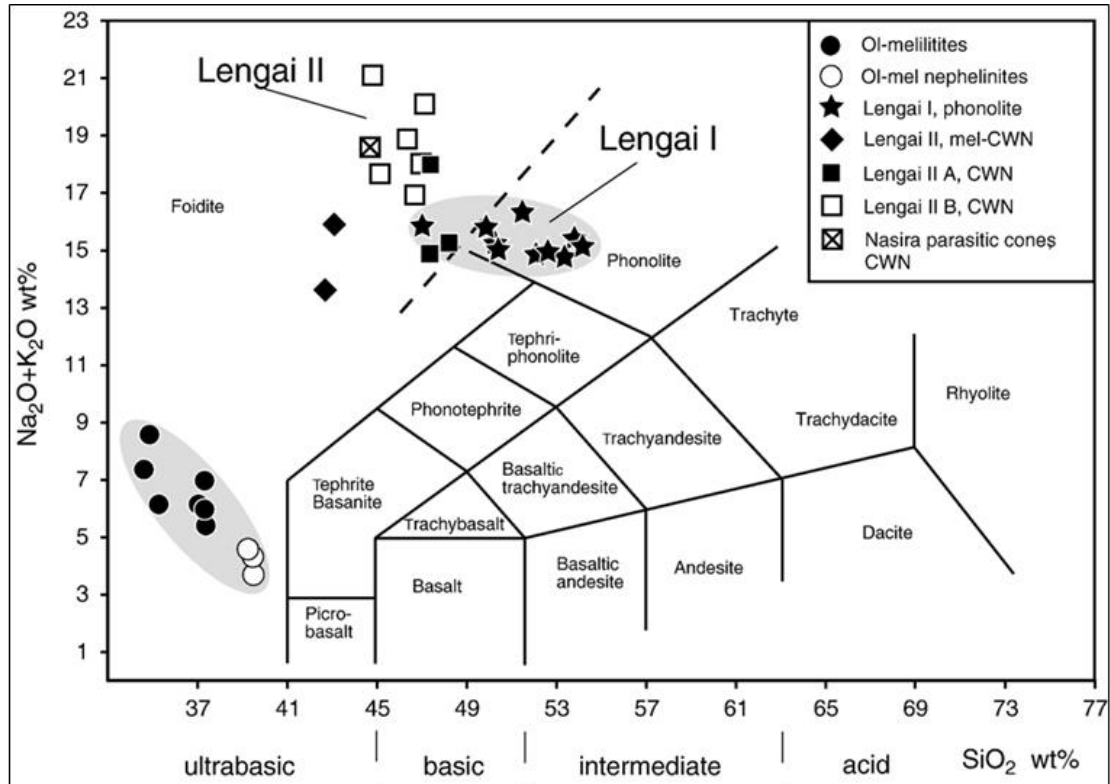
Mineralogical analysis of ash deposits from Lengai's Sept 2007- July 2008 explosive eruption demonstrates the presence of two distinct nephelinite magmas; combeitic-wollastonite nephelinite (CWN from the OL2 sample set) a more evolved, low-glass and crystal-rich magma, with wollastonite-combeite nephelinite composition similar to that which erupted in 1993 (Dawson et al, 1994); and a deeper sourced combeite-free wollastonite-nephelinite (WN, from the ASHES sample set), also found in deposits from the 1917 eruption (Sharyin, 2012).

Additional lines of evidence for magma mixing during the 2007-8 explosive eruption at Lengai, reverse zoning, rim resorbtion, in addition to variance in groundmass composition and phase abundances. This mixing is likely an injection of magma from a hotter, deeper Si, Al, Mg and Mn enriched magma into Lengai's more evolved (re: peralkalinic and volatile depleted) magma chamber. Decompression melting of the deeper magma could explain the high degree of explosivity and volatile content (De Moor et al., 2013) of the 2007-8 eruption. The compositional difference and higher temperature of the deeper (WN) magma explains the resorbtion of the mineral grains of the more evolved CWN. The injection of a deeper sourced magma (WN-ASHES) that has undergone incomplete crystallization into a shallower chamber of combeite-bearing crystal-rich magma (CWN-OL2) is responsible for disequilibrium of minerals with the surrounding melt, this occurs in both assemblages and produces features such as overgrowth, compositional zoning and mineral instability.

Lengai historically typically erupted two general types of nephelinite magmas, as seen in the total alkali vs. silicate diagram compiling the compositions of the cone-building

deposits (Klaudius and Keller 2006, Figure 15). Both compositions fall into the foidite field, however, the more Si rich deposits tend toward a more phonolitic composition. Further analyses of the melt from these samples coupled with REE and trace element analyses may help further evidence that the WN came from a deeper source than the CWN, thereby supporting the premise that the assemblages, textures and compositional variability demonstrated by these deposits are a result of magma–mixing.

Figure 15: TAS: composition of Lengai historic cone-building deposits (Klaudius and Keller 2006)



(Klaudius and Keller 2006): TAS-diagram after Le Maitre et al. (1989) for Oldoinyo Lengai peralkaline lavas. Dashed line denotes proposed division between Foidite and Phonolite fields. Olivine melilitite and olivine-melilitite nephelinite data from Keller et al. (2006). CWN: combeitic-wollastonite-nephelinite

Implications

It is vital to note this hypothesis can be applied to historic eruptive activity and can be evidenced in the earliest, cone-building deposits at Lengai. These deposits are composed of interbedded and highly differentiated mineral assemblages (Dawson, 1962, 1966). The extruded black pyroclastic nephelinites, which compose the majority of the volcano, contain nepheline, clinopyroxene, garnet, apatite, magnetite, and glass. However, three additional phases: vishnevite, wollastonite and combeite both interbed, and pre-date this black layer (Donaldson, 1987). Similarly, these deposits contained the same minerals with the exception of vishnevite. The combeite-bearing (CWN-OL2) deposits of this eruption will also interbed the WN deposits (Figure 1). This suggests that this magma-mixing process is not a new occurrence at Lengai, but may be evident in prior deposits as well. The varied nephelinite mineral content which is a common occurrence in Lengai's eruptive history and has been attributed to a variety of causes, commonly natrocarbonatite-nephelinite interactions (Dawson 1998) and chemical stratification within magma chamber (Kjarsgaard and Hamilton, 1989). However, recent geophysical studies and seismicity/eruption correlation also support the existence of a third deep-seated magma source below Lengai. This has been evidenced by the presence of dykes as deep as 15km (InSAR elastic modeling Baer et al, 2008), and the occurrence of a peak seismic event at a depth of 8km (USGS NEIC). A study by Biggs et al (2013), containing geodetic observational data from Lengai area for 2007-2010 suggests one of three sources of the seismic onset was the presence of a dyke deep and narrow enough to be geodetically undetected.

Geochemically, mineralogical data from Lengai is not only integral in aiding petrologists to further our understanding of the rare foidite field of the TAS diagram, but perhaps more specifically can provide vital geochemical data needed to define phase stability in mixed magma silicon-carbon liquid immiscibility systems, and the ongoing role played by their parental magmas.

References

- Baer, G., Hamiel, Y., Shamir, G. & Nof, R., Evolution of a magma driven earthquake swarm and triggering of the nearby Oldoinyo Lengai eruption, as resolved by InSAR, ground observations and elastic modeling, East African Rift, 2007, Earth planet. Sci. Lett., 272 (2008.): 339–352
- Biggs, J., Amelung, F., Gourmelen, N., Dixon, T.H. & Kim, S., InSAR observations of 2007 Tanzania rifting episode reveal mixed fault and dyke extension in an immature continental rift, Geophys. J. Int., 179 (2009a): 549–558.
- Biggs J., Amelung F., Gourmelon N., Dixon T., Kim Sang-Wan, “InSAR observations of 2007 Tanzania rifting episode reveal mixed fault and dyke extension in an immature continental rift,” Geophysical Journal International, (Oct 2009), 179:549–558, <https://doi.org/10.1111/j.1365-246X.2009.04262>.
- Dawson, J.B., “The Geology of Oldoinyo Lengai,” Bull Volcanol (1962) 24: 349. <https://doi.org/10.1007/BF02599356>
- Dawson J. B., Pyle D. M., and Pinkerton H., “Evolution of Natrocarbonatite from a Wollastonite Nephelinite Parent: Evidence from the June, 1993 Eruption of Oldoinyo Lengai, Tanzania,” The Journal of Geology (Jan 1996), 104(1):41-54. <https://doi.org/10.1086/629800>
- Dawson J.B., Hili, P.G. “Mineral chemistry of a peralkaline combeite lamprophyllite nephelinite from Oldoinyo Lengai, Tanzania,” Mineralogical Magazine (Apr 1998) 62(2):179-196
- Dawson J.B., Joseph V. Smith, and I. M. Steele, Combeite ($\text{Na}_2\text{Ca}_2\text{Si}_3\text{O}_9$) from Oldoinyo Lengai, Tanzania, The Journal of Geology (1989) 97:3, 365-372
- Dawson JB, Bowden P, Clark GC., Activity of the carbonatite volcano Oldoinyo Lengai, 1966. Geol Rundsch (1968) 57:865–879.
- Dawson JB, Pinkerton H, Norton GE, Pyle D (1990) Physicochemical properties of alkali carbonatite lavas: data from the 1988 eruption of

Oldoinyo Lengai, Tanzania. *Geology* 18:260–263.

De Moor M., Fischer T.P., King P., Botcharnikov R.E., Hervig R.L., Hilton D.R., Barry P., Mangasini F., Ramirez C., “Volatile-rich silicate melts from Oldoinyo Lengai volcano(Tanzania):Implications for carbonatite genesis and eruptive behavior” *Earth and Planetary Science Letters* (Jan 2013), 361:379-390

Droop, G.T.R., A general equation for estimating Fe^{3+} concentrations in ferromagnesian silicates and oxides from microprobe analyses, using stoichiometric data. *Mineralogical Magazine*, 51 (1987), 431-5.

Fairhead, J.D., Girdler, R.W. The seismicity of Africa. *Geophys. J. R. Astron. Soc.* 24 (1971): 271–301.

Fischer, T.P., Burnard, P., Marty, B., Hilton, D.R., Furi, E., Palhol, F., Sharp, Z.D. & Mangasini, F. Upper-mantle volatile chemistry at Oldoinyo Lengai volcano and the origin of carbonatites, *Nature*, 459 (2009), 77–80.

Global Volcanism Program:

http://volcano.si.edu/volcano.cfm?vn=222120#bgvn_200711

Keller J., Zaitsev A.N., Geochemistry and petrogenetic significance of natrocarbonatites at Oldoinyo Lengai, Tanzania: Composition of lavas from 1988 to 2007, *Journal of Volcanology and Geothermal Research* (Jan 1997), 75:89-106; <https://doi.org/10.1016/j.lithos.2012.08.012>

Kervyn, M., Ernst, G.G.J., Keller, J. et al., “Fundamental changes in the activity of the natrocarbonatite volcano Oldoinyo Lengai, Tanzania,” *Bull Volcanol* (2010) 72: 913. <https://doi.org/10.1007/s00445-010-0360-0>

[Klaudius J.](#), [Keller J.](#), Peralkaline silicate lavas at Oldoinyo Lengai, Tanzania. *Lithos* (Oct 2006), 91(1-4):173-190
<https://doi.org/10.1016/j.lithos.2006.03.017>

Lee, Woh-Jer, and Peter J. Wyllie. “Experimental Data Bearing on Liquid Immiscibility, Crystal Fractionation, and the Origin of Calcicarbonatites and Natrocarbonatites *International Geology Review*, vol. 36, no. 9, 1994, pp. 797–819., doi:10.1080/00206819409465489.

Mitchell, R. H., and J. B. Dawson. "The 24th September 2007 ash eruption of the carbonatite volcano Oldoinyo Lengai, Tanzania: mineralogy of the ash and implications for formation of a new hybrid magma type." *Mineralogical Magazine* 71.5 (2007): 483-492.

Nimis, P., and P. Ulmer. "Clinopyroxene Geobarometry of Magmatic Rocks Part 1: An Expanded Structural Geobarometer for Anhydrous and Hydrous, Basic and Ultrabasic Systems." *Contributions to Mineralogy and Petrology* 133.1-2 (1998): 122-35.

Nyblade, A.A., Owens, T.J., Gurrola, H., Ritsema, J., Langston, C.A. Seismic evidence for a deep upper mantle thermal anomaly beneath East Africa. *Geology* 7 (2000): 599–602.

Nyblade, A. "The upper mantle low velocity anomaly beneath Ethiopia, Kenya and Tanzania: constraints on the origin of the African Superswell in eastern Africa and plate versus plume models of mantle dynamics." *Volcanism and Evolution of the African Lithosphere* 478 (2011): 37-50.

Pekov, I.V., Krivovichev, S.V., Zolotarev, A.A., Yakovenchuk, V.N., Armbruster, T., Pakhomovsky, Y.A. (2009) Crystal chemistry and nomenclature of the lovozerite group. *European Journal of Mineralogy*: 21: 1061-1071.

Peterson, T.D. "Peralkaline nephelinites. I. Comparative petrology of Shombole and Oldoinyo Lengai, East Africa" *Contr. Mineral. and Petrol.* (1989) 101: 458. <https://doi.org/10.1007/BF00372219>

Peterson T.D., Kjarsgaard B.A., What Are the Parental Magmas at Oldoinyo Lengai. In: Bell K., Keller J. (eds) *Carbonatite Volcanism*. IAVCEI Proceedings in Volcanology, vol 4. Springer, Berlin, Heidelberg

Petibon, C.M., Kjarsgaard, B.A., Jenner, A., Jackson, S.E., Phase relationships of a silicate-bearing natrocarbonatite from Oldoinyo Lengai at 20 and 100 MPa. *Journal of Petrology* 39 (1998): 2137–2151

Victor V. Sharygin, Vadim S. Kamenetsky, Anatoly N. Zaitsev, Maya B. Kamenetsky, Silicate–natrocarbonatite liquid immiscibility in 1917 eruption combeite–wollastonite nephelinite, Oldoinyo Lengai Volcano, Tanzania: Melt inclusion study. *Lithos* 152 (2012): 23-39

[Olivine, Pyroxene, Garnet, Spinel and Feldspar Spreadsheets](#): (updated by Rhian Jones, 2015)
https://serc.carleton.edu/research_education/equilibria/mineralformulaerecalculated.html

[Clinopyroxene Formula Spreadsheet](#): (cpx.formula.v2)
https://serc.carleton.edu/research_education/equilibria/mineralformulaerecalculated.html

CHAPTER II:

MAGMA MIXING AT OLDOINYO LENGAI: MINERAL AND MELT TRACE ELEMENT ANALYSIS OF 2007-8 ERUPTIVE DEPOSITS

By:

Nicole Thomas

Abstract

Oldoinyo Lengai is the world's only active natrocarbonatite-nephelinite mixed-magma system on earth. Recent volcanic activity and geochemical studies suggest there may be two nephelinite magmas mixing prior to the 2007-8 eruption.

In this study, we present scanning electron microscope (SEM) analyses from 2006 natrocarbonatite deposits, electron microprobe (EMPA) melt analyses for the 2007-8 eruptive nephelinite deposits: combeite-wollastonite nephelinite (CWN) and wollastonite nephelinite (WN). We also present laser ablation inductively-coupled plasma mass spectrometry (LA-ICPMS) trace and rare earth element data (ppm) for a xenolith sample (consisting of CPX and apatite), melt phenocrysts (andradite, and CPX), and matrix (a non-vitrified, non-crystalline, ultrafine ash representative of the pre-eruptive melt

composition). Rare earth and trace element data presented for: V, Cr, Cu, Zn, Rb, Sr, Y, Zr, Nb, Ba, La, Ce, Pr, Nd, Sm, Eu, Gd, Tb, Dy, Ho, Er, Tm, Yb, Lu, Pb, Th, and U. In addition, mineral/matrix partition coefficients (Kds) are presented for andradite and CPX.

From the total alkali vs. silicate (TAS) diagram and Harker's diagram two distinct melt compositions were identified. These two melt compositions are characterized by different REE and trace element abundance patterns for the melt and phenocrysts, both of which demonstrate differences of up to 3 orders of magnitude in concentration (ppm), especially in the LREE.

Similarity in trace- and rare-earth-element-normalized abundance patterns for both matrix and andradite phenocryst analyses suggest they share a common source and may originate from the same parental magma. However the broad range in values suggests that the WN may be more recently evolved from the parental magma than the CWN, which demonstrates evidence of contact with natrocarbonatite in the form of resulting enrichments of HREE, Th and U.

However, interaction with the natrocarbonatite was not indicated by the CPX patterns, which show significant differences in concentration (ppm; normalized to CI chondrite), in addition to a pronounced negative K anomaly and a positive Y anomaly displayed by some samples.

Overlap in melt compositions is interpreted as the chemical signature of magma mixing, especially in combination with evidence of other disequilibrium features, as documented by Thomas et al (2018), such as CPX and garnet resorption, zoning, and the two different

mineral assemblages (CWN and WN).

The data from this study support the presence of a deeper nephelinite source (WN) injecting Lengai's primary nephelinite chamber (CWN) causing the 2007-8 eruption. A time series of seismic and eruptive events at Lengai supports the hypothesis that all explosive eruptions are triggered by injection of deeper magma (WN) which is preempted by a series of significant seismic events (ISC., 2001, Baer et al., 2008, and GVP., 2014), as supported in the most recent eruption by InSAR studies (Biggs et al 2009., 2013).

These geochemical data support the premise there is more than one nephelinitic magma source in the eruptive deposits from the 2007-8 eruption. These varied melt compositions match similar conebuilding deposits from the past (Dawson 1962, 1966, 1989, Klaudius and Keller 2006). Therefore, it could be inferred from this study that the explosive eruptions at Lengai are being triggered by injection of a deeper, more hydrous (De Moor et al., 2013) nephelinite, which is responsible for the chemical instability, melt/matrix disequilibrium, and REE/trace element variation of these eruptive ash deposits.

Table of Contents

CHAPTER II:.....	xi
List of Figures.....	xvi
List of Supplementary materials.....	xvii
List of Supplementary materials Tables:.....	xviii
Introduction.....	69
Geophysical and Volcanic Background.....	69
Magma Chamber (s).....	71
Geochemistry.....	72
Seismic and Eruptive Activity.....	77
Volatiles.....	78
Hypothesis.....	78
Methods.....	79
Sample Collection and Processing.....	79
SEM Analyses.....	80
Geochemical Analyses.....	80
Mineral Formula Calculations.....	81
LA_ICPMS Analyses.....	82
LA-ICPMS Normalization.....	83
QA/QC Summary.....	84
Results.....	86
Mineral Assemblages.....	89
Textural Observations.....	90

Melt Composition.....	90
LA-ICPMS.....	91
LA-ICPMS QA/QC.....	92
Xenolith: CPX and Apatite.....	93
Andradite.....	94
CPX.....	97
Ash Particulates/Matrix.....	100
Andradite Partition Coefficients from LA-ICPMS.....	102
Andradite Partition Coefficients.....	102
CPX Partition Coefficients.....	109
REE and Trace Element Ratios.....	110
Discussion.....	111
CWN and WN Melt compositions.....	111
CWN and WN Mineral Chemistry.....	113
Phenocryst: CPX.....	113
Phenocryst: Ti-andradite.....	114
Implications for magma origins.....	116
Carbonatite-silicate interactions.....	116
Mineral Partition Co-efficients (Kds).....	119
Magma-mixing.....	121
Geophysical and Eruptive Correlation.....	123
Alternate Hypotheses.....	126
Conclusion.....	132
References.....	134

List of Figures

Figure 1a Location.....	70
Figure 1b: Stratigraphic Section.....	75
Figure 1c: Explosivity and Earthquake Correlation.	77
Figure 3: Nephelinite SEM BSE.....	88
Figure 4a-b: TAS Melt Compositions.	91
Figure 9a-b: Andradite REE and Trace Element Compositions.....	95-96
Figure 10a-b: CPX REE and Trace Element Compositions.....	98-99
Figure 11a-b: Ash REE and Trace Element Compositions.	101-102
Figure 13-13b: Andradite Partition Coefficients.	105-106
Figure 14b: CPX Partition Coefficients.....	108-109
Figures 15c, e, g: Eruption Sequence Schematic.	129-131

List of Supplementary materials Figures:

Figure 2: Natrocarbonatite SEM Backscatter Electron Image.....S-1

Figure 4b: TAS Lengai 1989..... S-2

Figure 5: Lengai 2007-8 Melt Composition: Mg#[Na+ Al]..... S-3

Figure 6: Lengai 2007-8 Oxides..... S-4

Figure 7a: Melt Oxide Abundances SiO₂/MgO (wt%)..... S-5

Figure 7b: Melt Oxide Abundances SiO₂/Al₂O₃ (wt%)..... S-6

Figure 7c: Melt Oxide Abundances SiO₂/TiO₂ (wt%)..... S-7

Figure 7d: Melt Oxide Abundances SiO₂/CaO (wt%)..... S-8

Figure 7e: Melt Oxide Abundances SiO₂/Na₂O (wt%)..... S-9

Figure 7f: Melt oxide abundances SiO₂/FeO (Tot) (wt%)..... S-10

Figure 7g: Melt oxide abundances SiO₂/K₂O (wt%)..... S-11

Figure 7h: Melt oxide abundances SiO₂/P₂O₅ (wt%)..... S-12

Figure 8a: Rare Earth Element Abundances (ppm) Xenolith..... S-13

Figure 8b: Trace Element Abundances (ppm) Xenolith..... S-14

Figure 10c: Y vs. Sr/Y (ppm) for CPX from LA-ICPMS..... S-15

Figures 12a-i: Melt Trace Element Ratios (ppm)..... S-16-24

Figure 15a-h: Schematic of Eruption Sequence.....S-25-32

List of Supplementary materials Tables:

Table 1: Natrocarbonatite Composition as Generated by SEM EDS.....	S-33
Table 2: Apatite from Xenolith Elemental Abundances (ppm).....	S-34
Table 3: CPX from Xenolith LA-ICPMS Elemental Abundances (ppm).....	S-35
Table 4: Ti-andradite LA-ICPMS Elemental Abundances (ppm).....	S-36
Table 5: CPX from Ashes LA-ICPMS Elemental Abundances (ppm).....	S-38
Table 6: Finest Ash Particulates LA-ICPMS Elemental Abundances.....	S-39
Table 7: Lengai 2007-8 Andradite Partition Coefficients	S-44
Table 8: Lengai 2007-8 CPX Partition Coefficients from LA-ICPMS.....	S-45
Table 9: Elemental Ratios from Matrix (ppm).....	S-47

Introduction

Oldoinyo Lengai is a stratovolcano located in the eastern portion of The Great Rift Valley, known as the Gregory rift in Tanzania Africa, just south of Lake Natron (Figure 1a).

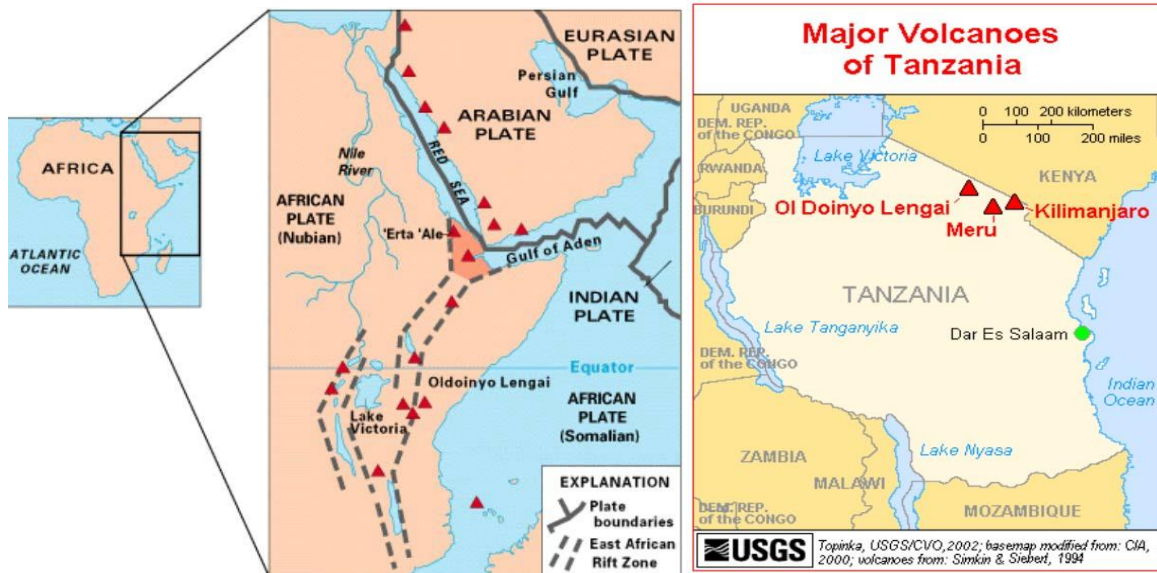
Aside from the lava lake atop Mt. Nyamuragira, Lengai is the only currently active volcano in the Great Rift Valley, and the only carbonatite volcano to erupt in historic time.

Geophysical and Volcanic Background

In Northern Tanzania, near Lake Natron, the East Africa Rift's (EAR) Eastern branch transforms from a narrow (50 km wide) N-S rift zone to a broad (300 km wide) extension area, which terminates near Lengai. Large escarpment features from the largest rifting event in this region were dated 1.15-1.2Ma (MacIntyre et al., 1974). At the end of the extensional zone three branches of the EAR, the NW trending Pangani rift, the N-S trending Manyara rift, and the NNE trending Eyasi rift form the North Tanzania Divergence (NTD) triple junction (Baker et al., 1972; Dawson, 1992; Foster et al., 1997). The NTD is known for a deep-sourced, upper mantle low-velocity thermal anomaly (Nyblade et al., 2000), which has been attributed to a superplume (Nyblade, 2011), and is noted for its high degree of seismicity compared to the surrounding region (Fairhead and Girder, 1971). This thermal anomaly has also been attributed to magma intrusion associated with the beginning of the final stages of continental rifting. In addition there is ample supporting evidence from Rayleigh wave tomography of an upper mantle plume beneath the Archean Tanzanian craton, which is located between the two mixed-magma

carbonatite- silicate (both combeite bearing) volcanoes: the active lava lake at Mt. Nyiragongo and Oldoinyo Lengai) (Dayanthie et al., 2003).

Figure 1a: Oldoinyo Lengai Location



Lengai cycles through effusive-eruptive volcanism marked by either natrocarbonatite or nephelinite deposits respectively. Typically, Lengai produces long-lasting effusive natrocarbonatite tephra and lavas. These volcanic deposits are anhydrous, low silica, high sodium, and of noticeably low temperature and viscosity (535⁰C and ~0.516 poise) (Dawson, 1962, 1998). Alternately, approximately every 30-50 years Lengai has a subplinian or plinian explosive pyroclastic eruption event/sequence of short duration. These nephelinite deposits are also low silica, high sodium and marked the presence of unique mineralogy forming the foidite field of the total alkali vs. silicate (TAS) diagrams (Figure 4a and Figure S-4b).

Magma Chamber(s)

The magma chamber(s) below Lengai are compositionally and thermally stratified (Kjarsgaard and Hamilton, 1989). The lower density, lower viscosity natrocarbonatite caps the more viscous, denser nephelinite magma (Dawson et al., 2007). Temperatures increase significantly with depth within the magma chamber to account for the presence of both the low temperature natrocarbonatite and the peralkalinitic nephelinite. Magma temperatures for Lengai magma chamber have been estimated at 550-800⁰C (Kervyn et al., 2010). Petibon et al. (1998), modeled the sub-volcanic structural plumbing of Lengai, as a two-story magma chamber; with the deeper chamber at approximately 3.3 km (~100MPa) depth, and the shallower chamber at ~0.6 km (~20 MPa depth). Although the presence of a third, deeper magma chamber has not been examined, geophysical models derived from recent InSAR

data from the 2007 earthquake (Baer et al., 2008) swarm demonstrate the occurrence of dykes at a depth of 15km is indicative of the potential of another, previously unpredicted deep-seated magma source at Lengai.

Silicate lavas extruded at Lengai are comprised of olivine-free nephelinites, phonolitic nephelinites, and phonotites (Dawson, 1962a). The earliest extruded black pyroclastic nephelinites that compose the majority of the volcano contain: nepheline, clinopyroxene, garnet, apatite, magnetite, and glass (Donaldson et al., 1987). However, three additional phases: vishnevite, wollastonite, and combeite interbed, and pre-date this black layer.

Geochemistry

The mineralogy at Lengai is singularly unique, not only as the only source worldwide of natrocarbonatites, but also in the unique minerals which occur only at this volcano: gregoryite- $(\text{Na}_2, \text{K}_2, \text{Ca})\text{CO}_3$, and nyerereite- $\text{Na}_2\text{Ca}(\text{CO}_3)_2$, both crystallizing in the Natrocarbonatite. Lengai is also host to another rare Al-free silicate mineral: combeite- $\text{Na}_2\text{Ca}_2\text{Si}_3\text{O}_9$ which crystallizes in the nephelinite magma, and is a mineral unique to Lengai, Nyiragongo, and Shombole (Dawson et al., 1989, Peterson et al., 1989, Peterson and Kjarsgaard, 1995, Dawson et al., 1998)

Recent SEM and EMPA analyses from the 2007-8 eruption revealed two distinct nephelinite assemblages (Thomas et al, 2018). Mineral phases present within both of the assemblages are: augite, nepheline, wollastonite, apatite and Fe-rich Ti-andradite, and Fe-oxide. The only difference in the ash layers is that the OL2 ash samples contain combeite ($\text{Na}_2\text{Ca}_2\text{Si}_3\text{O}_9$). The ash samples represent two nephelinite magmas defined by several

major differences: glass to mineral percentage, the presence of combeite in the OL2, and disequilibrium features such as resorption, overgrowth, zoning and mineral instability (Thomas et al., 2018). The OL2 set contains a very low percentage (<2.5 vol% mean) of glass. The ASHES set has a much higher percentage of glass (up to 17 vol% in one sample and an average of 10 vol%). Ti-andradite and apatite from the OL2 sample set (CWN) were lower in SiO₂ content than T-andradite and apatite from the ASHES sample set (WN). Suggesting CWN is potentially a more evolved magma (with more crystallization, and less SiO₂ in the melt as a result), whereas ASHES are deeper sourced (higher glass content, higher Mg and Fe content). Additional lines of evidence for magma mixing in these eruptive products: zoning, rim resorption, variance in groundmass composition and abundance, and the sudden increase in SiO₂, Al₂O₃, FeO, and MgO in mineral rims (Thomas et al., 2018).

The ash samples were analyzed by layer (Thomas et al, 2018), these can be seen in Figure 1b. The OL2 sample set, a combeite-bearing assemblage (inferred to be from the magma chamber) was from Layers BCD and M, whereas the middle section of the deposit, the ASHES, sample set from layers e-l contained the glass-rich nephelinite with higher available SiO₂, Al₂O₃, MgO and FeO content.

The inference was made that the first deposits (layer M: CWN - combeite-bearing nephelinite) contained the vent plug and some of the magma chamber contents which emptied initially, then the higher velocity and lower viscosity, deeper-sourced nephelinite (Layers E-L: WN- combeite-free nephelinite), erupted continuously for the majority of the eruptive sequence. The final deposits (Layers BCD: CWN – combeite-bearing nephelinite)

contained the more viscous, and crystal- rich magma that had remained in the magma chamber.

Based on the existing evidence of magma mixing in these samples, a trace element and REE analyses (LA-ICPMS) of the minerals, and ash matrix, as well as additional EMPA analyses to further define the various melt compositions was undertaken at Columbia University Lamont-Doherty Earth Observatory and University of New Mexico respectively.

Figure1: Oldoinyo Lengai Ash Stratigraphy Column of eruptive ash deposits from 2007-8.

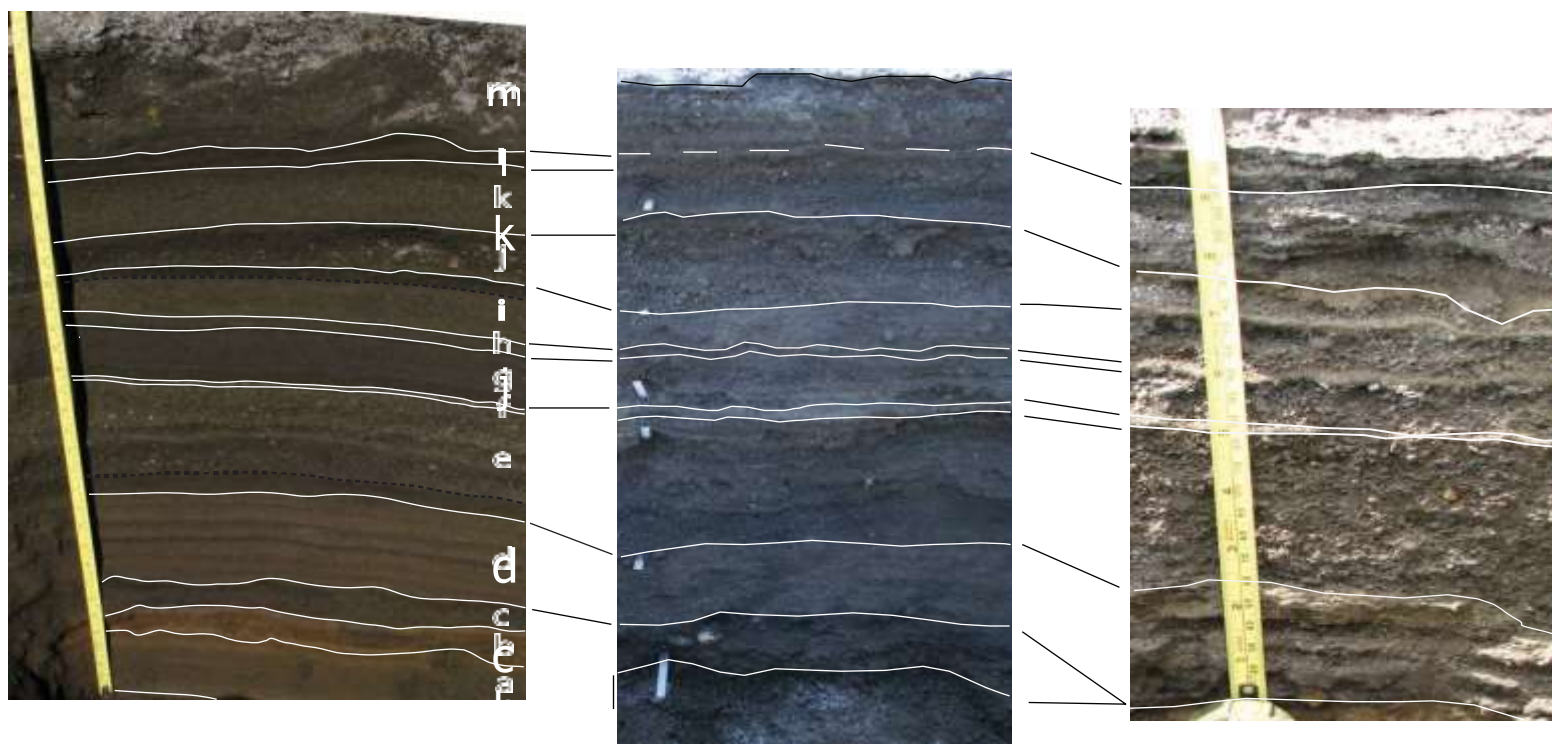


Figure 1b: 2007-8 Oldoinyo Lengai Nephelinite Ash Stratigraphy Column.
All samples collected and stored by layer as shown by Maarten de Moor. Letters denote the layer identifier within the ash deposits.
The scale is in inches on the left and centimeters on the right of the measurement tape.
Sample "OL2" is from the M layers of these deposits. Samples labeled "ASHES" were from layers E-J.
Scale is in inches on the left and centimeters on the right.
Photos and samples courtesy of Maarten De Moor

Seismic and Eruptive Activity

Since 1550 B.C.E., explosive eruptions at Lengai have been coupled with nephelinite ash deposits. The eruptive cycle at Lengai is usually 50 years of effusive natrocarbonatite flows followed by a more explosive nephelinitic eruption. The explosivity of the 2007-8 eruption Lengai was uncharacteristic in that it did not follow the typical periodicity (last explosive eruption was in 1993). In addition, it was the first pyroclastic eruption to be recorded at Lengai (Sept 6th 2007 plume rose 6km, with 12 hours of subsequent ash fall) (Keller et al., 2010). The eruption was pre-empted by the intrusion of a E–W 4 km-long trending dyke, with subsequent deflation directly below the summit of the volcano (Baer et al., 2008, Biggs et al., 2103). The sudden increase in the degree of explosivity is suggestive of magma and volatile recharge from a deeper source, possibly interacting with the crystal-rich, evolved nephelinite in the magma chamber, with subsequent degassing.

A time series of seismic events and eruptive activity at Lengai from 1960-2013 shows a direct correlation between all seismic events of greater than 3 MbN and all explosive (nephelinite) eruptions (Figure 1c). In contrast, the effusive, natrocarbonatite eruptions at Lengai are not correlated with seismic activity, and occur for long durations of over 20 years, such as from 1994 to 2006, between the last two explosive eruptions. The correlation between seismic swarms and explosive eruptions at Lengai implies that the eruptions may be being triggered by seismic activity.

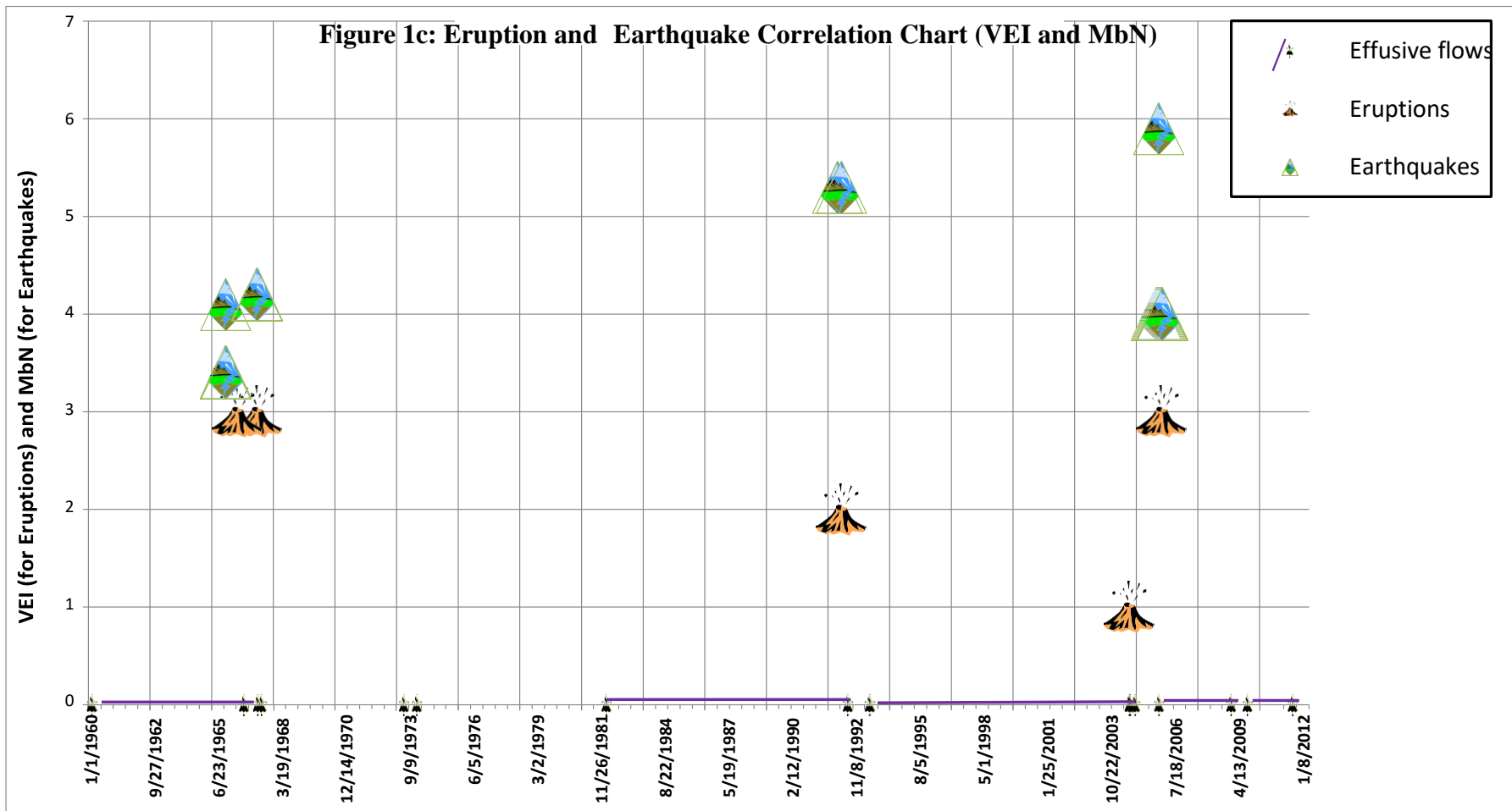


Figure 1c: A time series (1960-2014) of seismic and eruptive activity at Oldoiyo Lengai. Earthquakes (green triangles), effusive eruptions (purple lines and symbols), and explosive eruptions (volcano symbol) plotted according to either volcanic explosive index (VEI for eruptions) or moment magnitude (MbN for earthquakes) on the y-axis, and dates of on the x-axis ((Data sources: *International Seismological Center 2001, Baer et al 2008, and Global Volcanism Program 2014*).

Volatile Content

Previous fumarole H₂O analyses from the 1993 eruption (Koepenick et al., 1996), reported the lowest H₂O and highest CO₂ ever found at a volcano. However, the 2007-8 eruption was uncharacteristically pyroclastic (Feb 15th 2008 plume rose 11km, Global Volcanism Project). H₂O analyses from nepheline melt inclusions produced values ranging from 8-20 wt% (de Moor et al., 2013), values high even for high temperature, silicic magmas. The significant increase in the H₂O content in the 2007-8 eruption is suggestive of volatile recharge from a deeper source.

Hypothesis

The 2007-8 eruption at Lengai was triggered by an injection of a deeper-sourced wollastonite-nephelinite magma (WN) into Lengai's main magma chamber containing a combeitic wollastonite-nephelinite (CWN).

Methods

Sample Collection and Processing

Lava rock samples from the 2005-6 natrocarbonatite flows were collected by Tobias Fischer in July 2005 and September of 2006. A total of 3 natrocarbonatite samples were isolated for analysis.

Nephelinite ash samples were collected from the ash fall deposits of the 2007-8 eruption by Maarten de Moor in 2008 and 2009. A total of 6 of these ash sets were isolated for this analysis, representing the stratigraphic ash layers: BCD, E, F, G, L, M.

A xenolith sample was collected by Melania Maqway on July 4th 2014 from Lengai's southern crater, its location indicative of ejection during the 2007-8 eruption.

Lengai is carbonate-rich and previously presumed anhydrous; therefore it was necessary to take extra precautions in sample preparation to prevent the specimens' exposure to H₂O and to allow for carbon analyses.

Natrocarbonatite samples were processed for analysis using SEM. The lava rocks were broken into pieces <8mm diameter and glued to Al sample holders, followed by Au/Pd sputter coating. The delicate and friable nature of the anhydrous minerals (nyerereite and gregoryite) in the natrocarbonatite made it preferable to analyze the entire lava rock fragments rather than attempt to polish the samples.

Ashes (nephelinite) were set into 1" epoxy rounds. The samples were sonicated in anhydrous kerosene between all sanding and polishing steps. The final cleaning was completed with anhydrous alcohol, polished to 0.03µm finish, and initially

the samples were sputter-coated in a thin coat of Au to prevent charging during SEM and electron microprobe analyses. Then electron microprobe analyses were conducted with the Au coating to determine if there was carbon present in the ashes from interaction with the natrocarbonatite. When no carbon was found the Au coating was removed, the samples were subsequently re-polished and sputter coated with a thin layer of carbon (~6µm) to prevent charging during SEM and electron microprobe analyses.

Geochemical Analyses

Scanning Electron Microscope (SEM) Analyses

Natrocarbonatite.

A total of 8 natrocarbonatite lava samples were analyzed in the Scanning Electron Microscope at the University of New Mexico. Analytical conditions: 20kV, Spot size: 11µm, Aperture: 2, Z=10mm. Backscatter images were collected and mineral phases in the natrocarbonatite were initially identified with the SEM, from the EDS generated KCnt/kEv graphs. Observations were made from the BSE (Backscattered Scanning Electron) images on: crystalline textures, mineral grain sizes, and groundmass.

Electron Microprobe (EMPA) Analyses

Nephelinite.

A total of 5 nephelinite ash samples (representative samples from layers: BCD, E, G, LK, M (see Figure 1b for layers)) and 2 xenolith samples (OL14-1, OL14-2) were analyzed for Al, Ca, Fe, K, Mg, Mn, Na, P, S, Si and Ti in the electron microprobe at UNM's Institute of Meteoritics, Department of Earth and Planetary

Sciences, with a JEOL 8800 Electron Microprobe with energy dispersive x-ray spectroscopy (EDS) and wave-dispersive spectroscopy (WDS). Operating conditions: accelerating voltage 15 kV, beam current 10 nA, counting times on peak and background were 30-60 seconds.

Initial analyses were conducted on the samples that were sputter coated in Au in order to allow for carbon analyses, and later re-analyzed after removal Au coat and recoating with carbon, with varying standards sets for each analysis. For a complete summary of the standards/coating used see the EMPA Appendix Raw data tables (S-Appendix).

Small areas of melt found in layers BCD, D, G, LK and M of the ash deposits were analyzed in the EMPA under the lowest possible beam current conditions (25kV, 10nA, focused) for Al, Ca, Fe, K, Mg, Mn, Na, P, S, Si, and Ti.

Three point analyses were taken at each LA-ICPMS location for the purpose of normalizing the LA-ICPMS intensities to ppm. Clinopyroxene, nepheline and Ti-andradite point analyses were conducted on mineral grains representing a range of crystal sizes from >10 μ m up to >500 μ m diameter (as measured on the shortest axis), in order to gain an impression of compositional changes occurring in the melt just prior to eruption.

Mineral Formula Calculations

FeO wt% for Ti-andradite and CPX was recalculated for Fe₂O₃ and FeO according to charge balance utilizing the updated [Olivine, Pyroxene, Garnet, Spinel and Feldspar](#)

[Spreadsheets](#) (as updated by Rhian Jones in 2015 for Andradite, and the [Clinopyroxene](#)

[Formula Spreadsheet](#) (cpx.formula.v2) for CPX; both found on the Science Education

and Research Center (SERC) website of Carleton College.

LA-ICPMS Analyses

Laser ablation inductively-coupled mass spectrometry (LA-ICPMS) analyses of clinopyroxene, nepheline and Ti-Andradite mineral grains were conducted at Lamont-Doherty Earth Observatory of Columbia University for the following trace and rare earth elements: ^7Li , ^9Be , ^{29}S , ^{31}P , ^{43}Ca , ^{47}Ti , ^{51}V , ^{52}Cr , ^{65}Cu , ^{66}Zn , ^{85}Rb , ^{88}Sr , ^{89}Y , ^{90}Zr , ^{93}Nb , ^{138}Ba , ^{139}La , ^{140}Ce , ^{141}Pr , ^{145}Nd , ^{147}Sm , ^{153}Eu , ^{160}Gd , ^{159}Tb , ^{163}Dy , ^{165}Ho , ^{166}Er , ^{169}Tm , ^{172}Yb , ^{175}Lu , ^{208}Pb , ^{232}Th , and ^{238}U .

Standards used: NIST-610 (Pearce) NIST-612 (Pearce), NIST-614 (Norman, Kent)

All values with counting errors exceeding $\pm 9.99\%$, and all values below the detection limit (BDL) were removed from the dataset. See QA/QC summary for a discussion on all discarded values.

All melt areas were too small to analyze with the laser (minimum spot size which would still produce viable totals was $50\mu\text{m}$ diameter). However, analyses were made of the finest ash particulates, which is as close to melt composition obtainable due to spot size constraints. These bulk ash analyses contained no mineral grains. Background epoxy values were subtracted from the totals of each individual sample to produce trace element data on the melt composition.

Finest ash particulates: this is the finest ash deposits within a sample layer without crystalline mush or mineral grains visible at the micron scale, from layers BCD, E, G, LK, and M.

Minerals: Clinopyroxene, Ti-andradite and nepheline from layers BCD, E, G ,LK and M.

7 CPX analysis points and 3 apatite (2 of from inclusions in CPX) from the xenolith sample (MEL-OL14)

LA-ICPMS Normalization

All raw data points were normalized from intensity to ppm by either utilizing the lab- provided macro: LasyBoy©; in which the user may select between SiO₂, TiO₂, or CaO wt% as the normalizing value. EMPA oxide wt% normalization values used for these analyses are an average of three points taken from the LA-ICPMS location (or as nearby as possible) on the same mineral grain. In cases where EMPA oxide wt% data for a mineral grain could not be obtained or was discarded due to low totals, the average wt% value for that mineral from that ash sample layer was used (see QA/QC summary).

QA/QC Summary

EMPA

All EMPA mineral grain points with a total oxide count less than 95 wt% or greater than 104.99 wt% were discarded.

Due to the small area, complex chemistry and friable texture of the melt, all data points with a total <80% were discarded.

LA-ICPMS

Data validation of all LA-ICPMS analyses was conducted as follows:

1. Setting background constraints in addition to upper and lower end limits for all intensity graphs.
2. Visual inspection of intensity graphs and data values for errors.
3. Normalization check: conducted by comparing the normalization generated value for a non-normalizing oxide (SiO₂ typically) against the EMPA collected value. All data had to fall within >2 wt% to pass.
4. BDL check: all data values that fell below the detection limit were removed
5. Accumulated counting errors: Removal of all data points with an accumulated counting error that exceeds $\pm 5\%$

Kd Calculations

Trace Element Partition Co-efficients (Kd) calculations from LA-ICPMS:

Mineral to ash matrix Kd values for trace elements were calculated from the normalized elemental values in ppm for each mineral (C_s) divided by the ash particulate (matrix/melt component) normalized values for the same layer. In the cases of more than one ash particulate analysis for the layer in question, the average taken from all the analyses for the layer was used (C_l). These partition co-efficients C_s/C_l calculated for andradite crystal/matrix partition co-efficients (Kds) and CPX crystal/matrix Kds.

EQ 1: $Kd_i = [C_s]_i/[C_l]_i$; where i indicates the trace or rare earth element of interest, C_s is the concentration (ppm) of element i in the solid (mineral grain), and C_l is the concentration (ppm) of element i in the liquid (fine ash particulates as melt equivalent).

Results

SEM: Natrocarbonatite

Mineralogical observations:

Two of the four minerals identified in the natrocarbonatite lavas are unique to Lengai, as that is their only known occurrence, they are: gregoryite (Na₂,K₂,Ca)CO₃, and nyererite Na₂,Ca(CO₃). In addition a sulphide known to occur at Lengai (Mitchell et al., 2008, 2012): an Fe-rich alabandite (MnS) is also present. A very delicate halide is also present, however due to the fine grained nature of the lava the EDS analyses for the halide appear to have some overlap with surrounding phases (halide areas were <5µm diameter, spot size was 11µm), the exact composition of the Na rich halide has yet to be determined. The glassy portions are Al, Na, and Ca-rich liquid enriched in: Ba, Sr, Mn, and Cl. All mineral compositions were generated by EDS (Table S-1).

Textural Observations:

Natrocarbonatite samples revealed a primarily gregoryite (Na₂,K₂,Ca)CO₃, and nyererite Na₂,Ca(CO₃) groundmass, with glassy areas, with secondary euhedral mineralization of acicular halides and microcrystalline ferroan alabandite (Figure S-2: natrocarbonatite BSE).

SEM and EMPA– Nephelinite

A total of 92 mineral grains from the ash layers BCD, E, G, LK, and M (Figure 1b) were analyzed for Si, Ti, Al, Fe (tot), Mn, Mg, Ca, Na, K, P, S, and F. All mineral grains which had LA-ICPMS analysis had a minimum of 3 points measured (for averaging the normalizing oxides necessary for converting LA-ICPMS data from intensity to ppm). BSE maps of all EMPA mineral analyses points can be found in the Appendix.

EMPA analysis points which were discarded due to low (<95 wt%) or poor totals (poor totals defined as totals that appeared non-representative as a result of the beam interaction area extending beyond the mineral grain boundary).

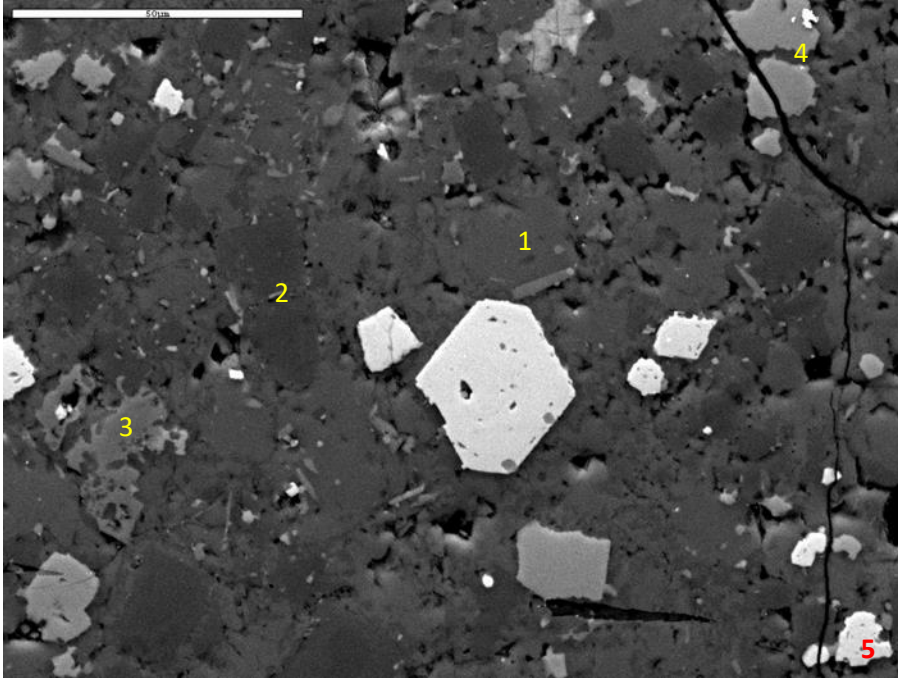
OL3 and OL5 (Layer BCD)

Textural Observations:

This previously unanalyzed nephelinite assemblage from layers B,C and D is a very low glass, crystal-mush rich combeite-wollastonite-nephelinite, with the same textural qualities, reverse zoning, resorbition rims and mineral instability as seen in the OL2 assemblage (Thomas et al., 2018). The combeite in OL3 retains its crystalline structure, whereas in OL5 it appears as a combeitic groundmass. Glass does not appear as a readily definable phase in the nephelinite samples as in the natrocarbonatite; however for OL5 the "combeite" phase abundance values represent the combeitic groundmass, not combeite crystals and therefore provides a rough estimate of the groundmass to mineral ratio at 0.33.

Figure 3a: Layer BCD (CWN) Nephelinite Ash: Textural Observations (SEM BSE Image)

1: Combeitic groundmass, 2: Nepheline evidencing mineral overgrowth, 3: Almost fully resorbed CPX, 4: partially resorbed CPX, 5: partially resorbed garnet.



Mineral Assemblages:

Two distinct nephelinite mineral assemblages are present in the ash deposits. The nephelinite assemblages are distinguished by the presence of combeite ($\text{Na}_2\text{Ca}_2\text{Si}_3\text{O}_9$), a rare, highly peralkalitic cyclo-silicate, by the degree of glass content vs. crystalline micromush, and differing relative mineral abundances (Thomas et al., 2018). The combeitic-wollastonite-nephelinite (CWN), and the wollastonite-nephelinite (WN) are represented in the depositional layer as follows:

CWN- combeitic-wollastonite-nephelinite (nepheline, CPX, Ti-andradite, wollastonite, combeite, apatite, Fe-oxides, primarily microcrystalline groundmass): This assemblage is encountered in the initial and final ash deposits (Layers BCD and M, Figure 1b).

WN- wollastonite-nephelinite: nepheline, CPX, Ti-andradite, wollastonite, apatite, Fe-oxides, micromush only agglomerated to phenocrysts, much higher glass content. This assemblage is found in the middle of the ash deposits and composes a larger part of the depositional sequence (Layers E, G, KL).

EMPA: Melt

A total of 44 melt analyses were taken, of which 26 were discarded due to low totals. Low oxide totals for EMPA melt data can be partially attributed to fragility of melt upon beam contact, which was visible as destruction of the sample area. Low melt totals may also represent electron beam induced decomposition.

Layers BCD, E, G, and M provided melt areas with viable totals, however Layer L,

despite an abundance of glass area proved too fine/friable for accurate melt analyses.

Textural Observations:

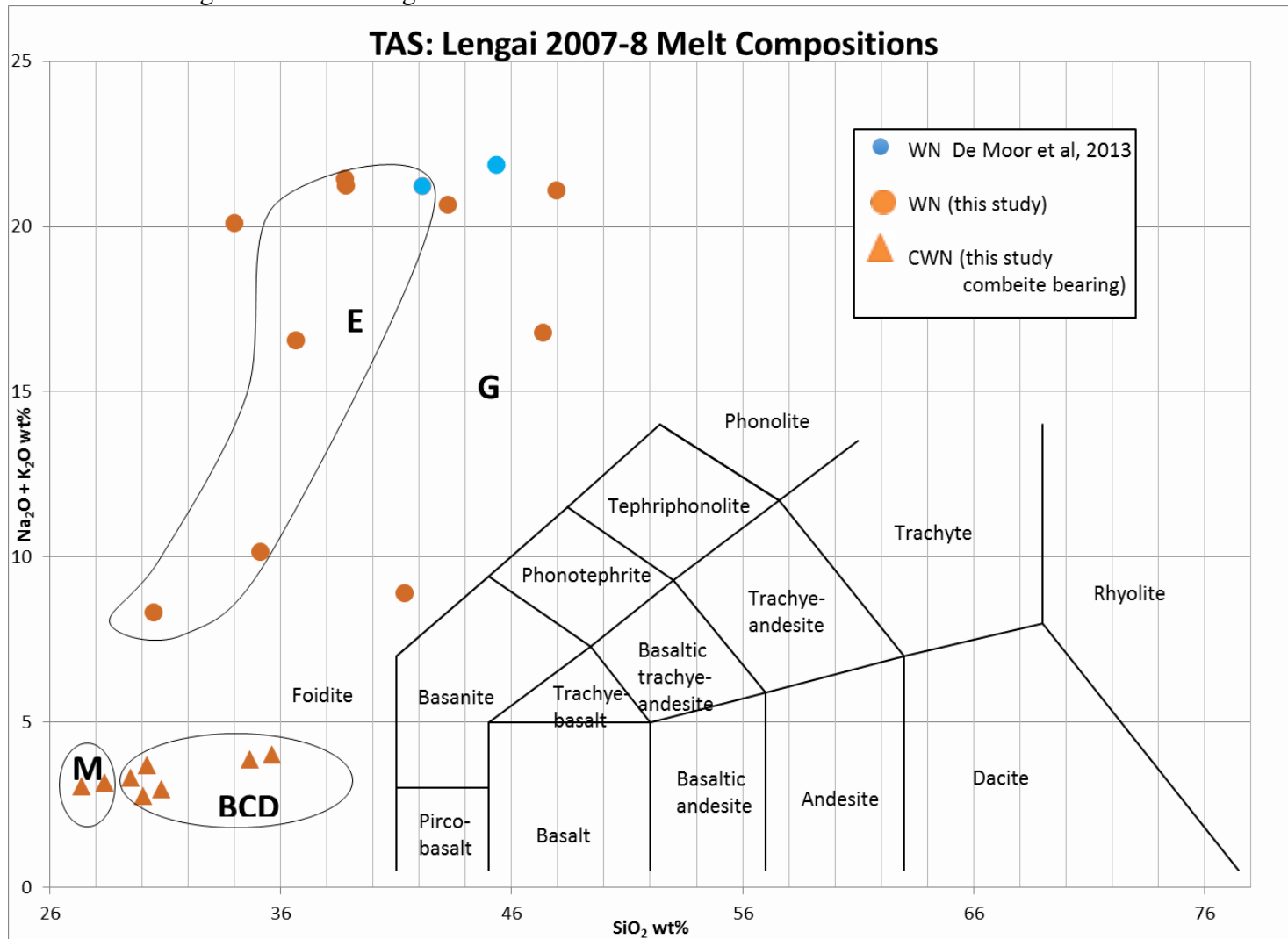
SEM and EMPA analyses of the 5 nephelinite ash samples revealed 3 main groundmass/glass textures:

- 1) Glassy melt: Layers BCD, E, G, M - low in abundance (<10% on average except for Layer L ~60%), very fine and friable with very small surface areas (<50 μm^2), subject to low totals due to the destruction of the sample upon beam impact.
- 2) Combeitic groundmass: Layers BCD, M
- 3) Micro-crystalline mush: All layers
- 4) Non-crystalline very fine ash particulates: All Layers

Melt Composition:

Melt point analyses from layers BCD, E, G, and M revealed distinct melt compositions differentiated primarily by SiO₂, Al₂O₃, and K₂O content. Figures 4a, S-5, S-6, and S-7a-h demonstrate the chemical variation in melt composition of the various ash deposits according to layer. A distinct pattern is evident, in which layers BCD and M (the combeite-bearing assemblage) contain a highly peralkalitic, SiO₂, Al₂O₃, Na₂O, and K₂O depleted composition.

Figure 4a: TAS Lengai 2007-8



LA-ICPMS

QA/QC Results

Nepheline LA-ICPMS mineral analyses contained concentrations of trace and rare earth elements that were very low. Consequently normalization using CaO or TiO₂ wt% was not possible as their abundance in the mineral structure was too low (<0.1 wt%). Attempts to normalize with SiO₂ wt% did not reproduce viable results as noted by the TiO₂ wt% values generated by the normalization were in excess of actual values collected by the probe.

Andradite data was successfully normalized by CaO wt%, as noted by comparison to the SiO₂ wt% values generated from the normalization macro as compared to actual values collected on the probe.

CPX was normalized by both CaO wt% and TiO₂ wt%. All CPX was initially normalized with CaO wt%, however, if the data did not pass the SiO₂ wt% crosscheck then normalization by TiO₂ wt% was attempted.

Mineral grain analyses that did not pass the SiO₂ wt% crosscheck by falling within less than 1.5 wt% of the EMPA analysis values after normalization were not presented in this study.

Layer LK proved too fragile and friable for good totals on the LA-ICPMS instrument. All data collected from the sample from layer LK was discarded.

613 Fine ash particulate points were discarded due to either below detection limit (BDL) or accumulated counting errors (ACE>9.99%).

411 Kd values for andradite and 338 Kd values for CPX had to be discarded due to either BDL or ACE error.

Xenolith: CPX and Apatite

The xenolith found on the non-active southern crater surface of Lengai's summit by Melania Maqway on July 4th 2014 was clearly ejected from the active crater during the most recent eruption, likely representative of magma chamber and/or conduit xenoliths, and therefore commonly in contact with the nephelinite from Lengai's primary magma chamber. This offers the opportunity to compare the composition of the CPX found in the xenolith to the CPX mineral grains in the ash deposits. Apatite analyses of one crystal and two inclusions in CPX demonstrated practically identical compositions.

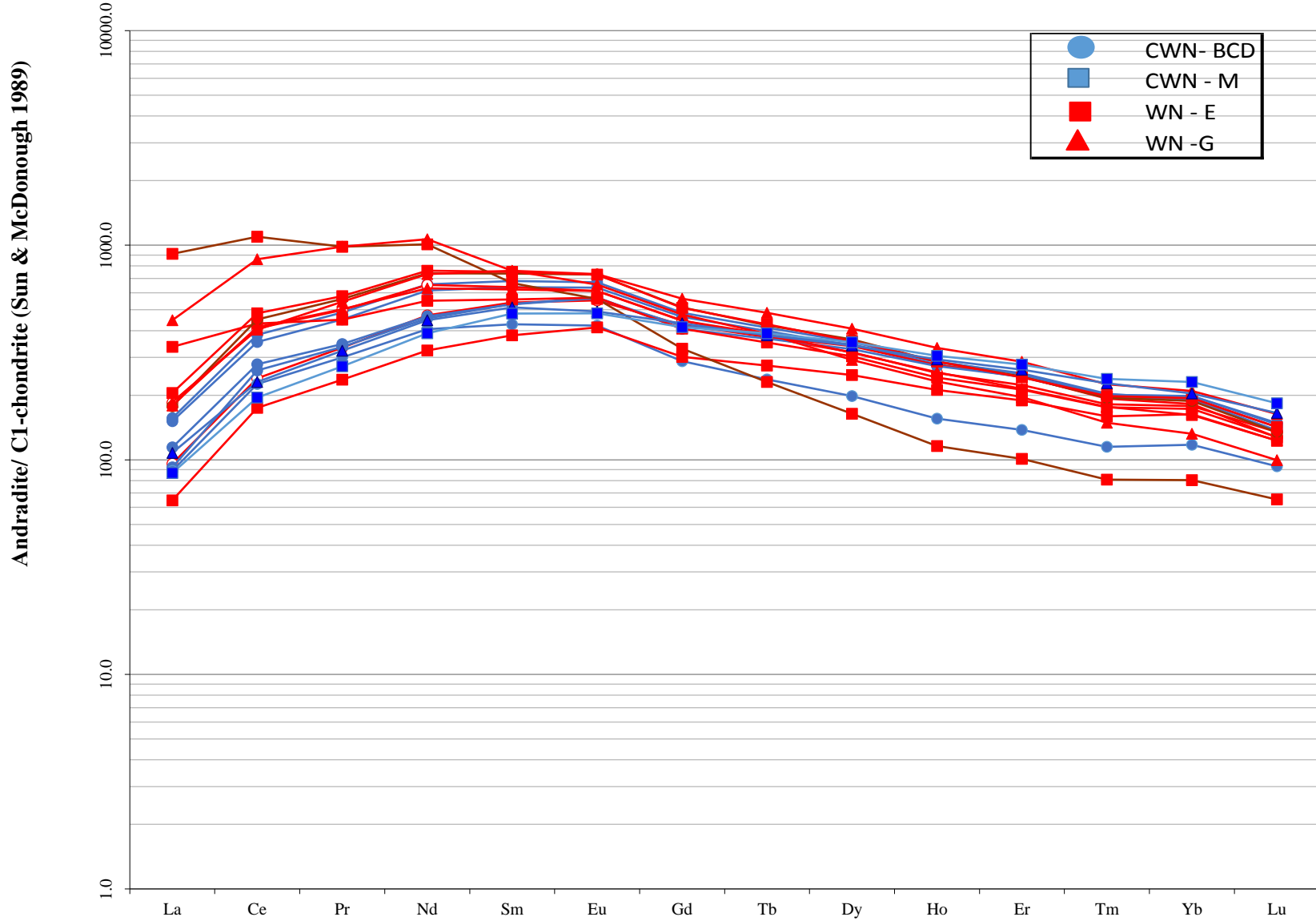
This xenolith is solely composed of apatite and CPX crystals. The apatite and CPX crystals in this xenolith co-crystallized as evidenced by the presence of co-inclusions. The LA-ICPMS data support this relationship, as the low concentration of light REEs in the CPX (seen as a slight negative parabolic trend) is counterbalanced by up to 2 orders of magnitude greater light REE abundances (ppm) in the apatite. In contrast the heavy REE concentrations in the apatite and CPX are within 5-27 ppm of each other, with the apatite still bearing the higher concentrations. The exceptions to this trend are evident in the trace element distribution (Figure S-8b), where Ti and Zr preferentially enter the CPX mineral formula as seen in the positive Zr and Ti anomaly in the CPX and then reflected by apatite's negative Zr and Ti anomaly. Niobium values for CPX produced poor totals except for one data point, with that exception all trace and REE analyzed

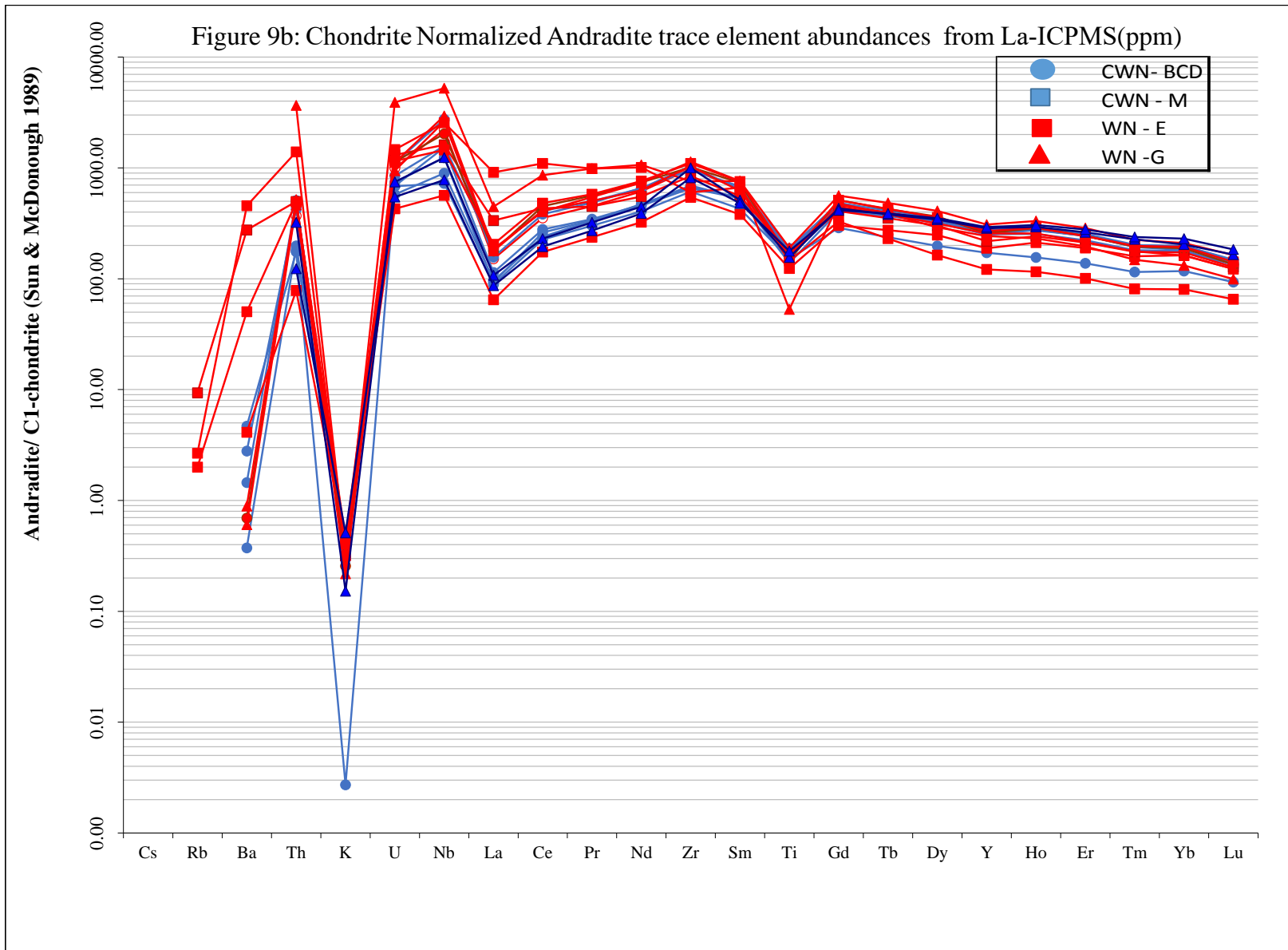
were inversely correlated between the two minerals apatite and CPX present in the xenolith, Trace element abundances not shown in Figures S-8a or S-8b can be found in Tables S-2 and S-3.

Andradite.

Andradite analyses from mineral grains in ash layers BCD, E, G and M (Figure 1b), demonstrated a range of greater than an order of magnitude in the light REEs (ranging from 15-215 ppm for La), as opposed to the heavy REEs which had ~5% of the variance seen in the light REEs (from 1.66-4.66ppm for Lu). Layer E had the highest variability in composition between mineral grains from the same sample (Figure 9a). Andradite trace element abundances reveal a slight Ti anomaly. Barium and Rb demonstrated up to 3 orders of magnitude difference in concentrations (Figure 9b). Niobium contents lie in the range of 139-677, and are at least 2 orders of magnitude greater than total Nb in the xenolith sample. All figures represent C-I chondrite (Sun and McDonough. 1989) normalized REE values. Chondrite normalized REE patterns for andradite of CWN and WN have a high range of value (1200) in the LREEs, and a range of 400 in the HREEs. Although these patterns do not resemble those of typical garnets, Ti-andradite is a rare garnet, and does not have any available trace or REE data in the GERM database to compare to.

Figure 9a: Chondrite Normalized Andradite REE abundances from LA-ICPMS(ppm)





CPX.

CPX analyses from mineral grains in ash layers BCD, E, G and M (Figure 1b), are plotted along with the CPX analyses from the xenolith for comparison (Figures 10a and 10b). Light REE values for CPX mineral grains from the ash deposits were on average at least an order of magnitude greater than the CPX from the xenolith. CPX samples from Layer E had the highest concentration of light REEs, with concentrations of La 3 orders of magnitude greater than the xenolith. Lanthanum concentrations from Layer E were as high as 368 ppm, as compared to La concentrations from the CPX from the xenolith which were as low as 1ppm. Within the 4 ash layers, BCD, E, G, and M there was a large variation in concentration in light REE (Figure 10a). Heavy REEs concentrations for all CPX were all very low (<1.5). Trace element distributions within the CPX Layer E sample had the lowest Ti content, and highest Nd values of all CPX analyzed. All CPX from the ash layers were higher in La, Ce and Pr than the xenolith CPX. Trace element abundances of CPX from the ashes not found in Figures 10a or 10b can be found in Table S-5, and those of CPX from the xenolith in Table S-3.

CPX/CI-chondrite (Sun & McDonough 1989)

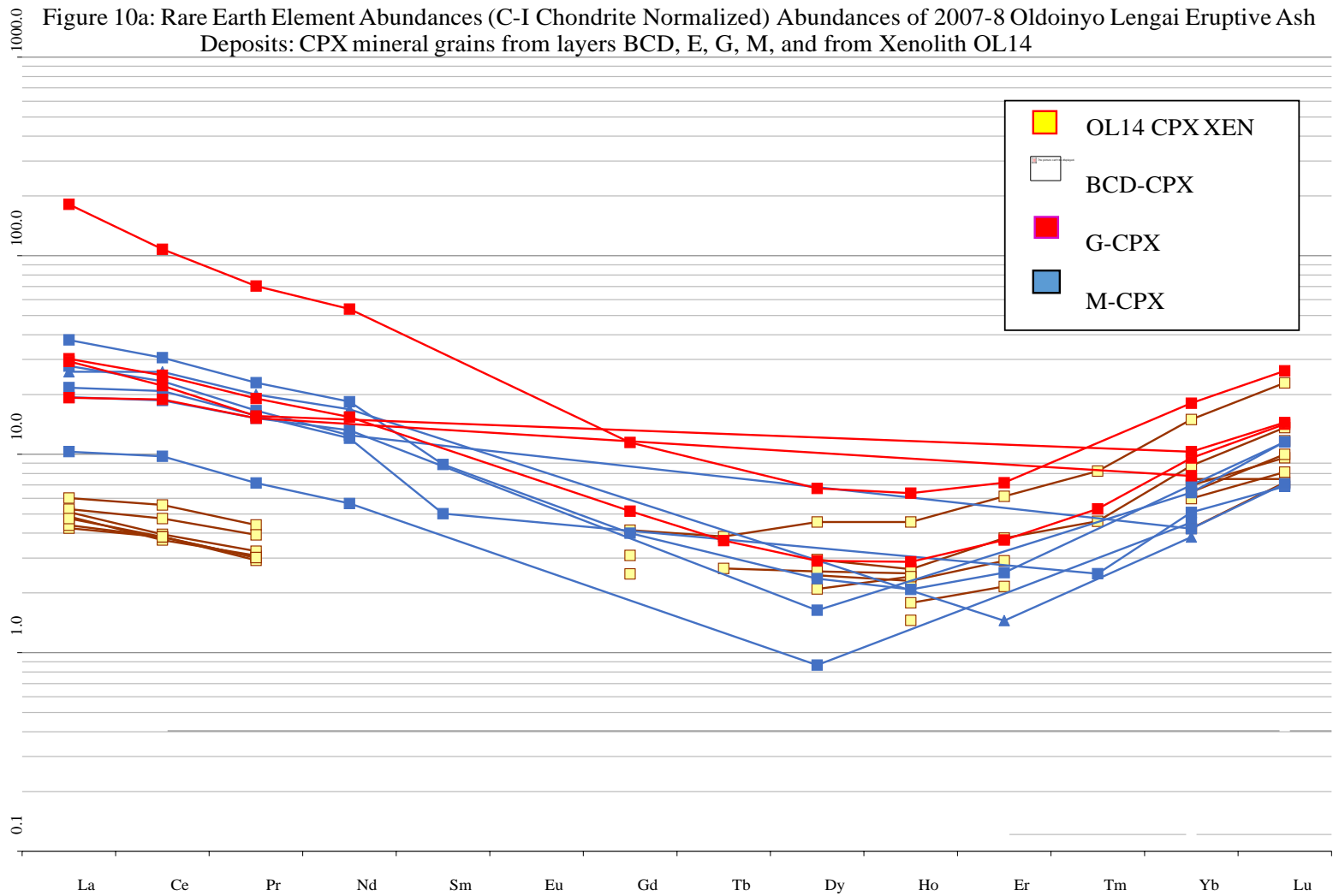
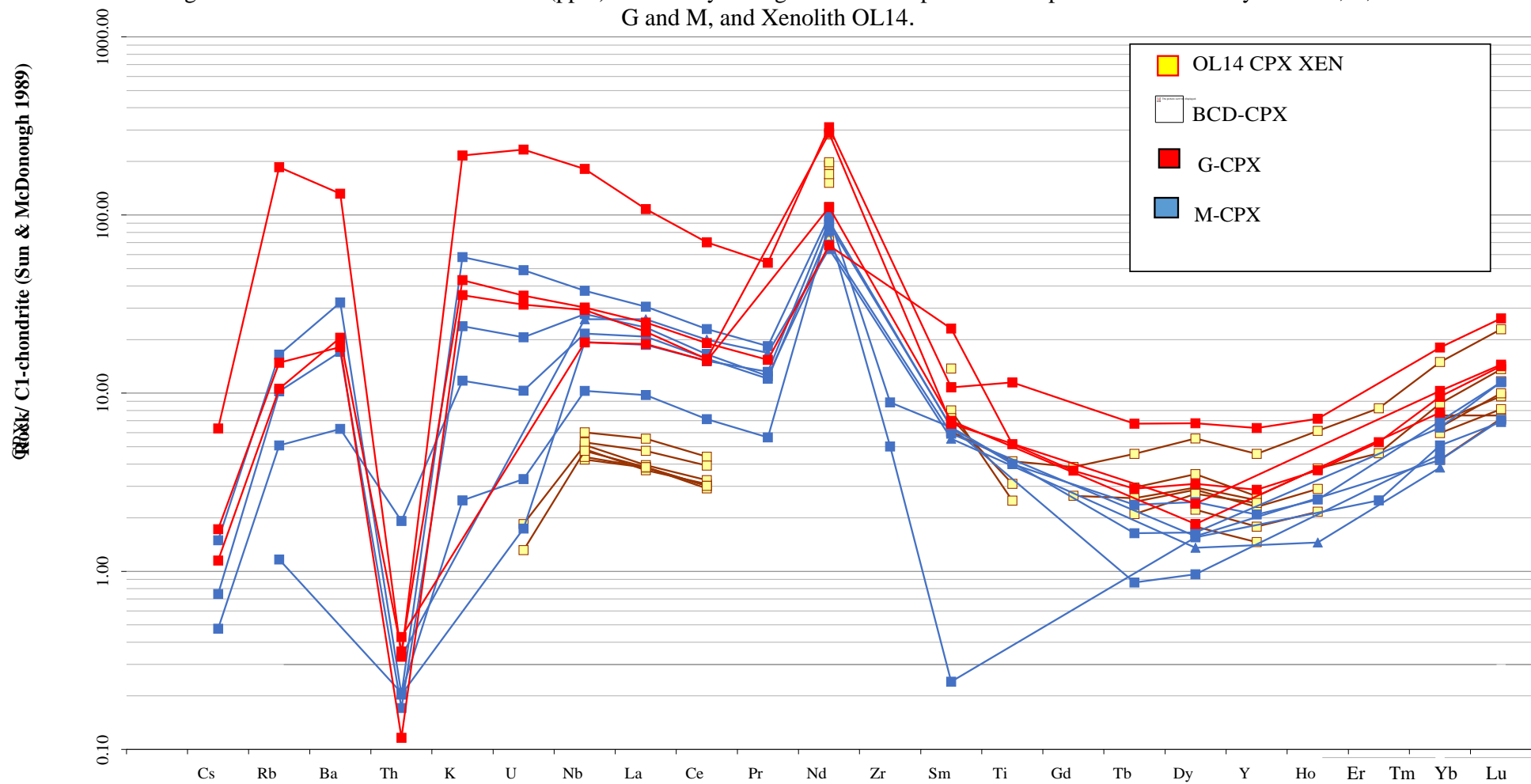


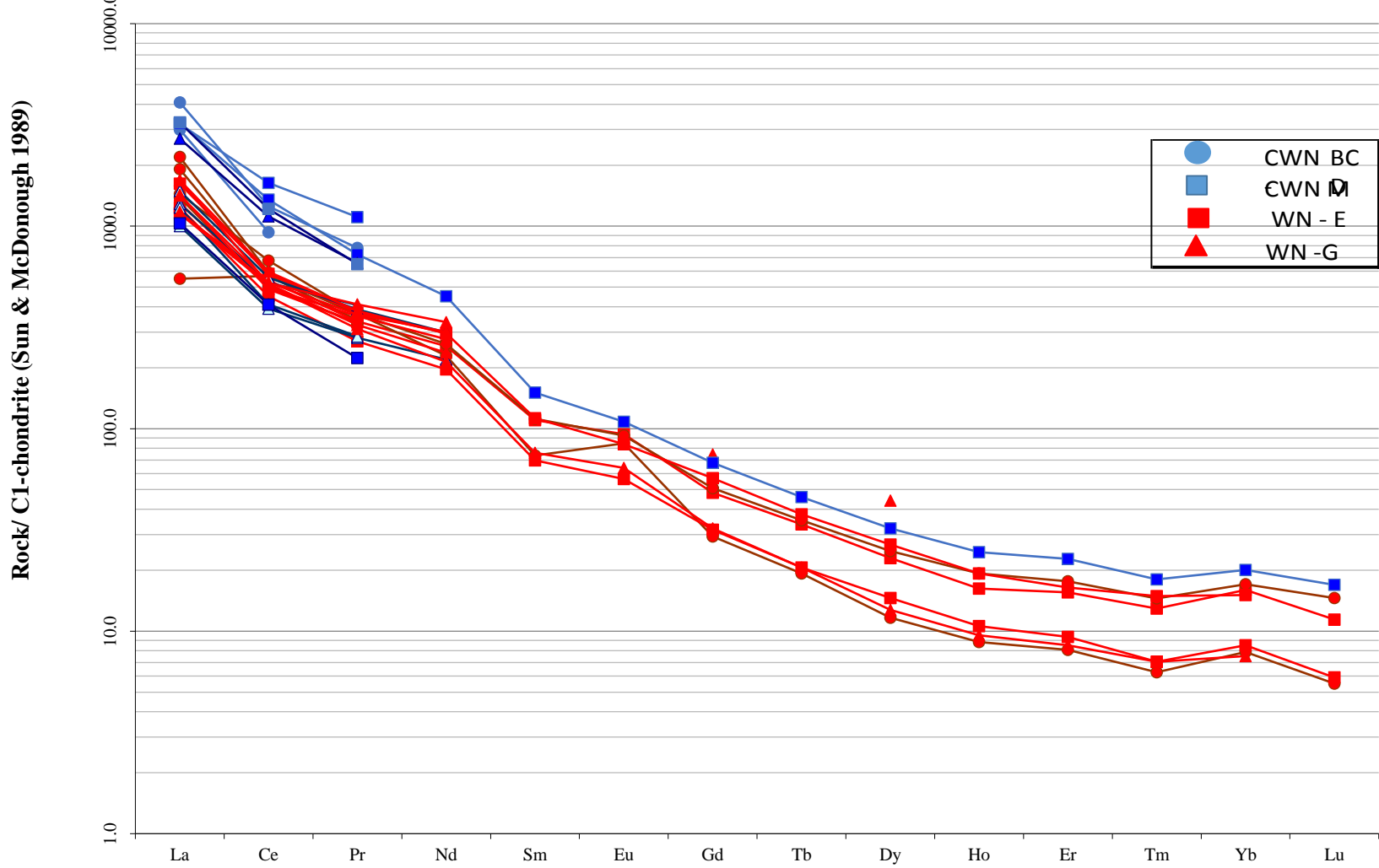
Figure 10b: Trace Element Abundance (ppm) of Oldoinyo Lengai 2007-8 Eruptive Ash Deposits: CPX from layers BCD, E, G and M, and Xenolith OL14.

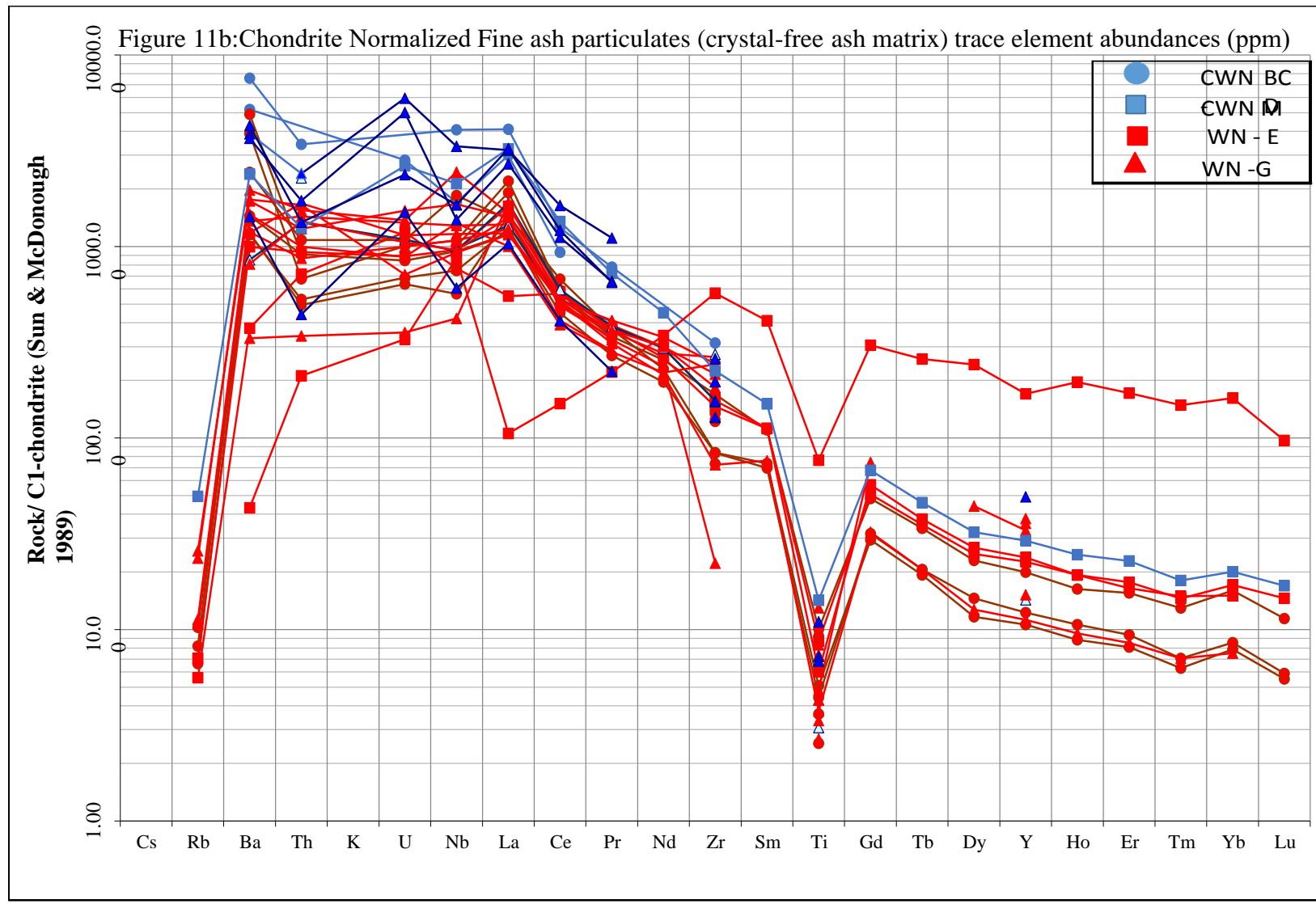


Matrix: Ultrafine Ash Particulates (Groundmass)

REE concentrations in the finest (non-crystalline) ashes from layers BCD, E, G, and M (Figure 1b) were relatively consistent in slope, layers BCD and M contained greater concentrations of the light REEs: La, Ce and Pr than the other layers (Figure 11a, and Table S-6). Heavy REE concentrations did not demonstrate as much variance by depositional layer. Layers BCD and M had the highest concentration of Sr and Ba, with up to an order of magnitude greater than the other layers. Trace element abundances not shown in Figures 11a or 11b can be found in Table S-6.

Figure 11a: Chondrite Normalized Fine ash particulates (crystal-free ash matrix) REE abundances from LA-ICPMS (ppm)





Partition Coefficients from LA-ICPMS

Kd values calculated from the mineral trace element concentrations for both andradite and CPX and matrix composition. The variability of the melt composition by depositional layer accounts for a large portion of the range for Kds. The wide range of REE and trace element concentrations displayed by the andradite and CPX mineral grains in the ash deposits produces a significant range of Kds.

Andradite Partition Coefficients

Ti-andradite phenocryst/matrix partition coefficients (Kds) are presented for: Rb, Ba, Sr, Pb, Zn, Cu, V, Y, Nb, Th, U, Zr, La, Ce, Pr, Nd, Sm, Eu, Gd, Tb, Dy, Ho, Er, Tm, Yb, Lu in Table S-7. The Kds for the REE as compared to previous studies allows for an understanding of the variability expressed. For example, a comparison with the high and low experimental Kd values of experimental garnets in carbonatites (Sweeney et al., 1992) for Rb, Sr, Y, Zr, Nb, Ba, Ce, Lu reveal that none of Kd values in these ash deposits, other than overlapping ranges for Zr are similar to those from Sweeney et al. (1992). This confirms that these garnets did not crystallize in the natrocarbonatite magma chamber and did not 'fall out' of the low viscosity carbonatite cap into the nephelinite magma. Comparing Kd values from this study for Sr, Ba, and Lu to other Kd garnet values in the GERM database, these Ti-andradites come closer to the composition of the experimental Kds of garnets from alkali basalts (GERM database: Shimizu, 1980) than garnets found in garnet pyroxenite from phenocryst/matrix studies (GERM database: Zack et al, 1997). Phenocryst/matrix Kds from garnets in hawaiiite (GERM

database: Irving and Frey, 1978) for La and Ho fall in the range of this study. There is some overlap with other garnet phenocryst/matrix Kds, however overall the Kds presented in this study are greater any other Kds presented for garnet REEs except for Lu and Yb in hawaiiite (GERM database: Irving and Frey, 1978). It is vital to note, that there do not exist andradite REE values in the GERM database to compare to, therefore attempting to compare or make inferences based on similarities to other garnets needs is subjective because the composition of these garnets is not represented by any of the garnet GERM Kds. Although, the garnets in experimental carbonatite-silicate conjugates from Sweeney et al. 1992 are used to determine if there were carbonatite interactions, it is important to note they are not very comparable due to significantly higher Al₂O₃ content, they more closely resemble grossular than andradite.

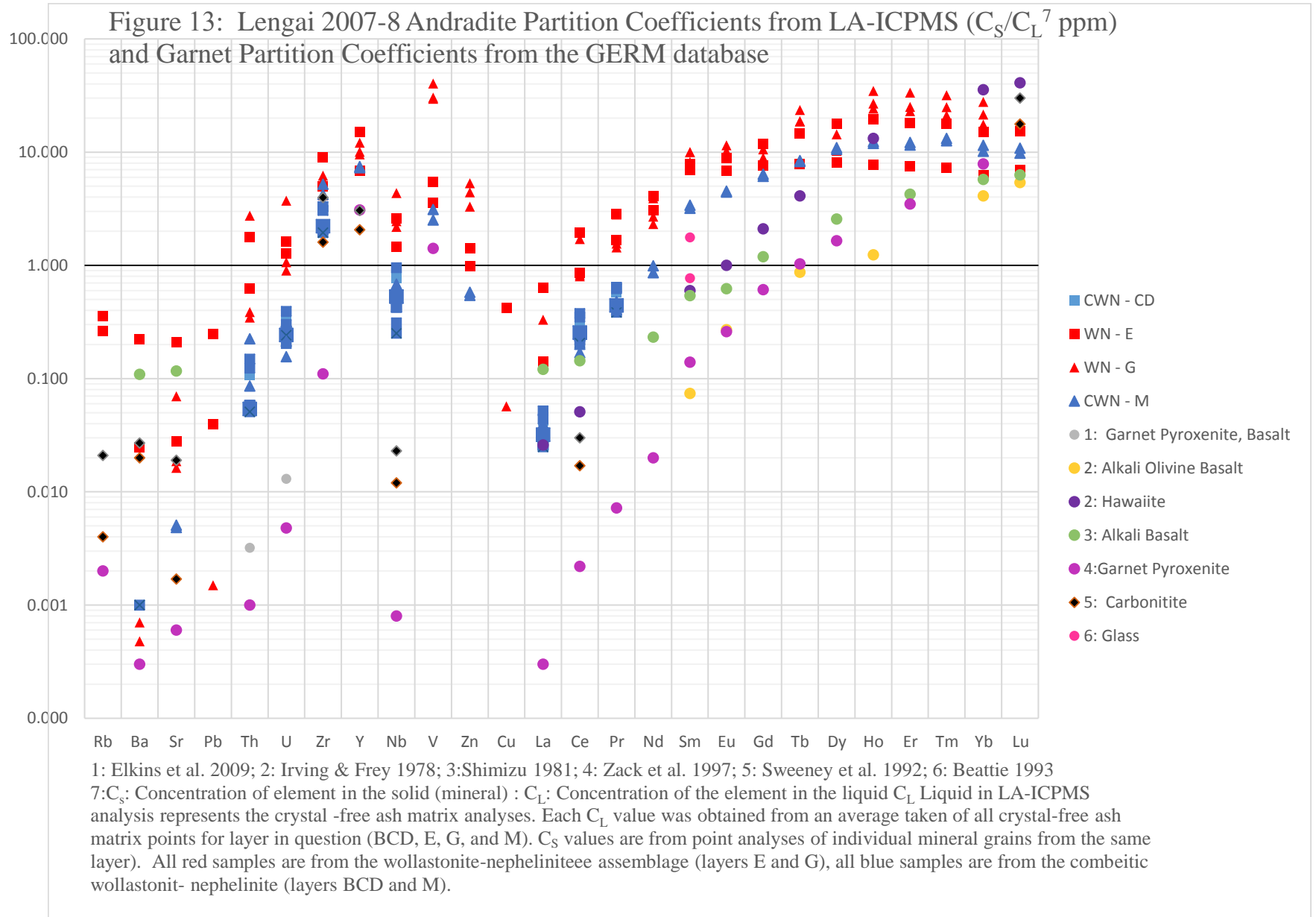
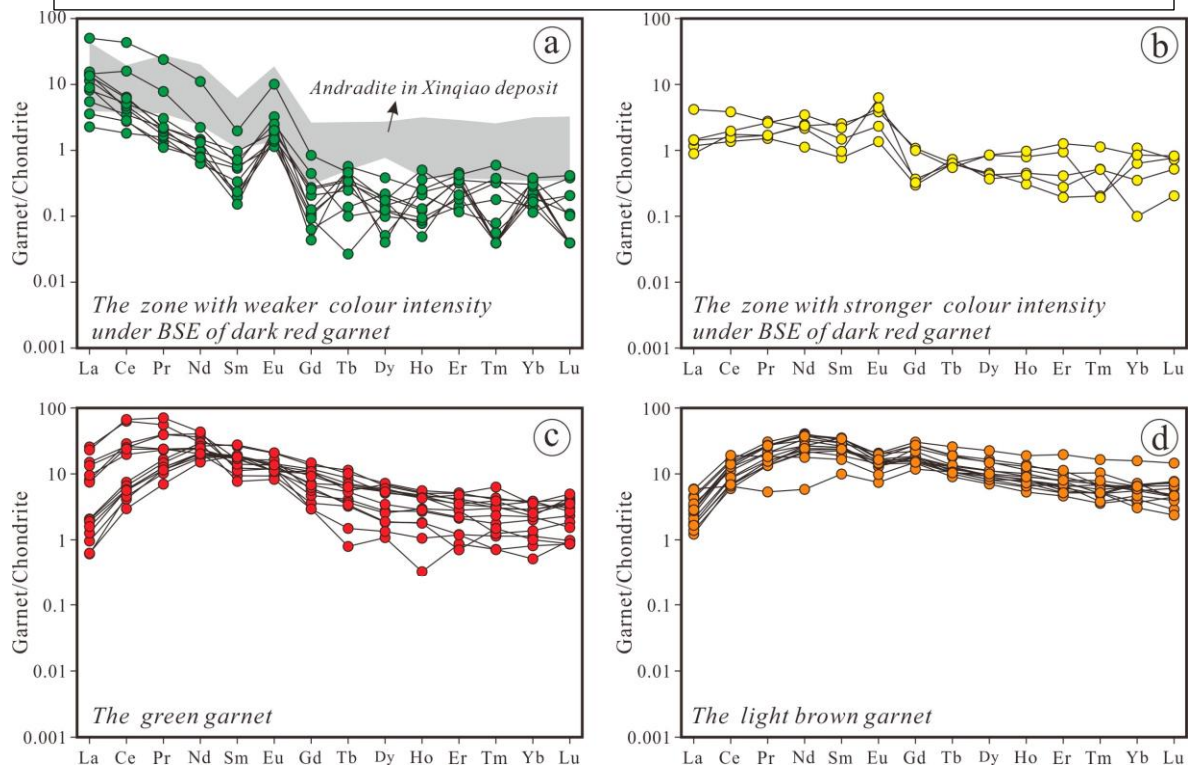


Figure 13b: Garnet REE patterns from Yongping China (Zhang et al. 2017)



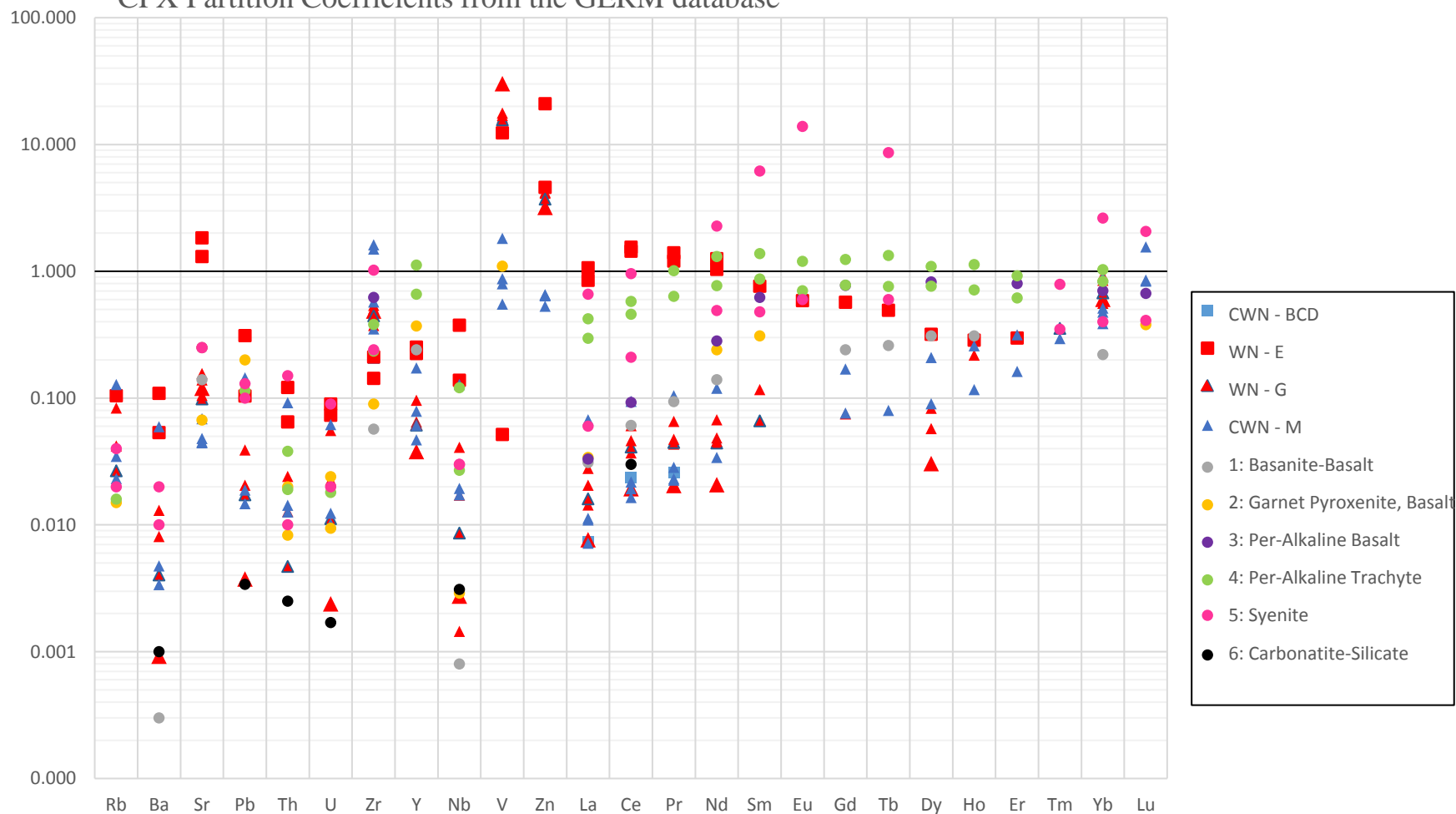
From Zhang et al (2017) Fingerprinting the Hydrothermal Fluid Characteristics from LA-ICP-MS Trace Element Geochemistry of Garnet in the Yongping Cu Deposit, SE China

Chondrite-normalized REE patterns of garnets from Yongping. Samples were normalized to the C1 values of Sun and McDonough [65]. The field of Xinqiao andradite is from [64]. (a) Zone with stronger color intensity under BSE of dark red garnet; (b) zone with weaker color intensity under BSE of dark red garnet; (c) green garnet; (d) light brown garnet.

CPX Partition Coefficients

Clinopyroxene (CPX) phenocryst/matrix partition coefficients (Kds) are presented for: Rb, Ba, Sr, Pb, Zn, Cu, V, Y, Nb, Th, U, Zr, La, Ce, Pr, Nd, Sm, Eu, Gd, Tb, Dy, Ho, Er, Tm, Yb, Lu in Table S-8. A comparison of the CPX Kds from this study and the calculated Kds of experimental augite partitioning in a carbonate melt for Nb, Ba, Ce, Pb, Th (Walker et al., 1992) demonstrate that the Kds for CPX in carbonate-silicate conjugate melt were at least an order of magnitude lower than those for this study, suggesting the CPX was not in contact with a carbonatite source. The Kds presented for: Zr, La, Ce, Nd, Sm, Eu, and Yb for CPX phenocryst in nephelinite matrix in this study are nearly the same (values overlap or fall within 5%) to phenocryst/matrix Kds of CPX from Alkali basalt (Fujimaki et al., 1984). Kds for Gd, Dy, and Er were greater in the CPX from alkali basalts (Fujimaki et al., 1984) than the Kds for the same elements for CPX from nephelinite matrix in this study. CPX Kds from this study were closest in composition to the alkali basalt compositions of Fujimaki et al., (1984), as opposed to CPX Kds from alkali trachyte (Larsen, 1979). Experimental Kd ranges presented for CPX from basanite-basalt at 2.5-7GPa (Green et al., 2000) for: Sr, Y, Zr, Nb, Ba, La, Ce, Pr, Nd, Sm, Eu, Gd, Tb, Dy, Ho, Er, and Yb were comparable to this study; and the CPX from nephelinite matrix producing overall higher Kds, with considerable overlap. Layer BCD bore atypically high (1.8-1.3) Kds for Sr, and the Kds for Nb, Y and Nd were an order of magnitude higher in these samples as compared to CPX from basanite-basalt (Green et al., 2000). In summary, the CPX Kds from CWN and WN differ by at least an order of magnitude for most elements, with up to 3 orders of magnitude difference for some elements, this supports the premise that the two

Figure 14: Lengai 2007-8 CPX Partition Coefficients from LA-ICPMS (C_S/C_L ppm) and CPX Partition Coefficients from the GERM database



1: Green et al. 2000; 2: Elkins et al. 2008; 3: Fujimaki et al. 1984; 4: Larsen 1979; 5: Marks et al. 2004; 6: Walker et al. 1992
 7: C_S : Concentration of element in the solid (mineral) : C_L : Concentration of the element in the liquid C_L Liquid in LA-ICPMS analysis represents the crystal -free ash matrix analyses. Each C_L value was obtained from an average taken of all crystal-free ash matrix points for layer in question (BCD, E, G, and M). C_S values are from point analyses of individual mineral grains from the same layer). All red samples are from the wollastonite-nephelinite assemblage (layers E and G), all blue samples are from the combeitic wollastonit- nephelinite (layers BCD and M).

Figure 14b: Partition Co-efficients for various CPX/matrix pairs from Fugimaki et al. 1984 for La, Ce, Nd, Sm, Eu, Gd, Dy, Er, Yb, Lu, Hf, and Zr

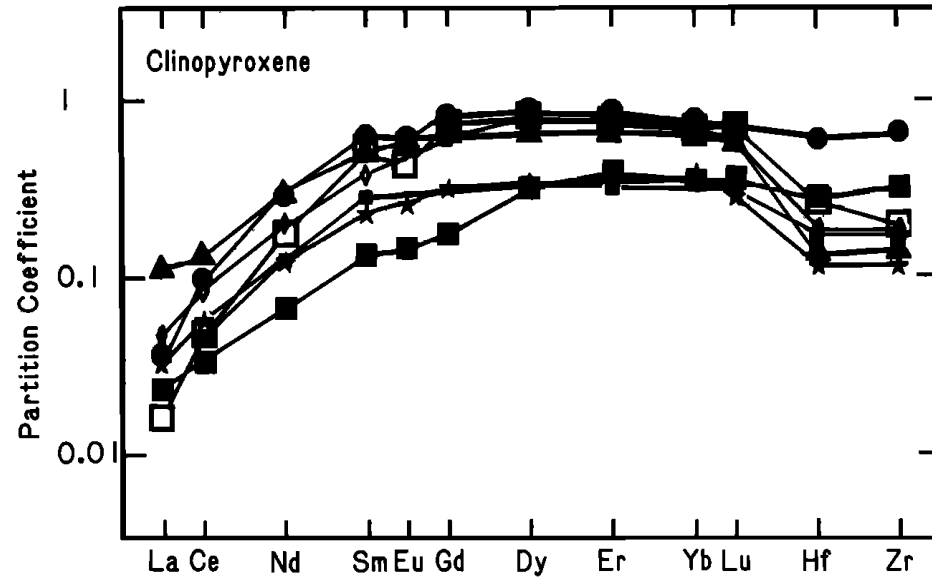


Fig. 3. Partition coefficients for Hf, Zr, and the rare earth elements between clinopyroxene phenocrysts, megacryst, and their corresponding matrices including experimental run product. Symbols: (■) megacryst in kimberlite; (●) phenocryst in peralkaline olivine-augite basalt from Nyamuragira; (▲) phenocryst in tholeiite basalt from Usu; (★) phenocryst in alkaline olivine-augite basalt from Hawaii; (□) phenocryst in augite-hypersthene dacite from Akita-yakeyama; (◇) phenocryst in augite-hypersthene andesite from Komagatake; (▪) synthetic augite.

assemblages WN and CWN represent different pressure, temperatures and compositions.

REE and Trace Element Ratios

Various trace element ratios for the matrix compositions of Layers BCD, E, G, and M.

Elemental ratios (ppm) from the ultrafine matrix: Th/U, Ba/Sr, Sm/Nd, Th/Nb, Ce/Pb,

Zr/Nb, La/Nb, Ba/Nb, Rb/Nb are presented in Table S-9. Elemental plots from the matrix

presented in Figures 12a-i respectively are: Sr/Y, V/[Th/U], Th/U, La/Nb, Rb/Sr, V/Nd

V/Pr, and V/Nb.

Discussion

CWN and WN Melt compositions

There are two different nephelinite assemblages in the ash deposits from the 2007-8 eruption at Lengai: combeitic wollastonite-nephelinite (CWN) and wollastonite-nephelinite (WN). The CWN is composed of the first and final eruptive ash deposits (layers M and BCD respectively, Figure 1b), and the WN is found in the middle eruptive deposits layers (E, G, KL, Figure 1b). These mineral assemblages vary in the following: the presence of combeite ($\text{Na}_2\text{Ca}_2\text{Si}_3\text{O}_9$), the glass vs. microcrystalline groundmass content, both major and minor element concentrations of primary minerals and relative mineral abundances (Thomas et al, 2018). In addition, in this study we observe significant chemical variation in the overall melt compositions (Figure 4a), the trace and rare earth element concentrations in the andradite and CPX phenocrysts from CWN and WN deposits (Figures 9a-b and 10a-b).

EMPA glass analyses are one of the clearest indicators of the compositional differences between CWN and WN melts. A plot of the 2007-8 Lengai melt compositions on the total alkali vs. silicate (TAS) diagram after Maitre et al., 1989 (Figure 4a) clearly demonstrates differences of several orders of magnitude difference based on assemblage. Comparison of these melts to those from previous cone-building eruption deposits at Lengai (Figure S-4b: data from Klaudius and Keller 2006) demonstrates that this pattern of widely

varied foidite melt compositions has occurred during some of the past episodes of large eruptive deposits at Lengai.

The CWN is a highly-evolved peralkalitic magma, as indicated by several factors: the presence of combeite; a unique mineral known to erupt from Lengai historically (Dawson et al., 1989, Peterson et al., 1989, Peterson and Kjarsgaard, 1995, Dawson et al., 1998), and the low glass content (Thomas et al., 2018). In addition, the CWN has far lower silica content (27-36 SiO₂ wt%) than the WN (31-46 wt%). The CWN melt composition is the lowest in total Na₂O + K₂O (<5 wt%, Figure 4a). Oxide abundances (Figures S- 7a-h) of the CWN samples (Layers BCD and M) demonstrate higher TiO₂, MgO, FeO, and lower Na₂O, as compared to WN (Layers E and G).

The WN melt, which does not contain combeite, contains greater SiO₂, Al₂O₃, K₂O, and Na₂O, with up to >19 wt% more SiO₂ than CWN, and Na₂O + K₂O 5-20% wt % higher than CWN (Figure 4a). WN texture is also indicative of a higher temperature and lower viscosity melt, due to a higher abundance of glass, and a lower abundance of larger phenocrysts (>150µm radius). Overall concentrations of REE and trace elements in the WN were significantly higher than the CWN. The LREEs are on average an order of magnitude greater in the CWN deposits than in the WN (Figure 11a-11b). In addition, the high field strength elements (HFSE) Th, U, and N, were relatively enriched in the CWN (by up to 3 orders of magnitude, Figure 11b), similar to Ba and K. In Figures S-12a-I, the two magma types are clearly distinguished by their trace element ratios. This implies the WN (ASHES sample set) was not in contact with the CWN when the CPX phenocrysts

crystallized, the WN CPX has higher Kds because of any combination of the following factors higher crystallization temperatures and pressures, and greater availability of trace and REE components in the melt.

CWN and WN Mineral Chemistry

Phenocryst: CPX

CPX resorption was one of the first mineralogical indicators of disequilibrium between the phenocrysts and the surrounding melt (Thomas et al., 2018). These earlier studies demonstrated that CPX from CWN contains a greater hedenburgite component than the CPX from WN, except for in the rims (within 10 μ m of grain boundary) and the smaller mineral grains which are more diopsidic in composition. This implies the CWN melt became enriched in MgO, which suggests an influx of more primitive magma into the CWN. Additionally, the presence of two CPX of very different compositions and crystallization histories, which could not have crystallized from the same magma were found in the WN deposits (Thomas et al., 2018). This variation in CPX composition was also reflected in the trace and rare-earth element analyses in this study (Figure 10a-b). These CPX partition co-efficients are the same as CPX partition co-efficients from other igneous and mantle rocks as shown by Fugimaki et al. (1984) for La, Ce, Nd, Sm, Eu, Gd, Dy, Er, Yb, Lu, Hf, and Zr (Figure 13b). As seen in Figure 14 partition co-efficients for La, Ce, and Nd range from .015 to 0.09, which is the same range of values for CPX (augite in Figure 13b) from

peralkaline olivine-augite basalt from Nyamuragira and from alkaline augite-olivine basalt from Hawaii. The Lu, and Zr Kds from this study were higher, and more closely resembled those Kds of megacrysts from Kimberlites. Layer E which demonstrated a much different pattern of Kds, was closer to the Kds of megacrysts from Kimberlites as well (Figures 14 and 14b). Although the REE patterns did not demonstrate much similarity with other CPX patterns, the Kds match up fairly well with those of generated by Fugimaki et al, (1984).

Phenocryst: Ti-andradite

Data for carbonatite trace element partitioning between silicate-carbonatite conjugate melts (Veksler et al., 2005) demonstrate that Zr, Hf, and the HREE preferentially fractionate into the conjugate silicate melt. Simultaneously, in nephelinite-natrocarbonatite conjugates Na₂O, CaO, Sr, Ba, and the LREE concentrations decrease in the silicate, as they preferentially fractionate into the natrocarbonatite melt (Keller and Spettel 1995; Kjarsgaard et al. 1995; Dawson 1998; Veksler et al. 2005). Since these elements are more compatible in the natrocarbonatite, then this would produce a decrease in their abundance (lower K_d values) if the silicate (nephelinite) melt had been in contact with the natrocarbonatite, then its store of Na₂O, CaO, Sr, Ba, and LREE would be depleted as these elements preferentially entered into the natrocarbonatite. In addition the HREEs and HFSE preferentially partition into the silicate (Petibon et al, 1998). This would potentially produce higher HREEs and lower LREEs in target minerals in the silicate that had been in contact with the carbonatite (such as garnet, known to be a REE sink) a decrease in the expected abundance for LREEs, and an increase in HREE and HFSE. Compared to other garnets, these garnets have a less steep slope, from LREE to HREE. When these patterns are compared to other patterns of garnets, surprisingly these garnet REE patterns more closely resemble the patterns presented by Zhang et al. (2017) of hydrothermal garnets from Yongping, China (Figure 12b).

The andradite in the CWN deposits have the lowest LREE values which was predicted from natrocarbonatite-silicate conjugates (Keller and Spettel, 1995; Kjarsgaard et al., 1995; Dawson, 1998; Veksler et al., 2005), with Sr and Ba

values up to an order of magnitude lower than in the WN. Since Sr and Ba are enriched in the natrocarbonatite, and these are an order of magnitude higher in the WN than the CWN, this implies that WN was not part of the system of liquid immiscibility involving the carbonatite liquid, and supports the premise that the WN is not from Lengai's main nephelinite magma chamber. Heavy REE values do not vary as much but are higher in the CWN as would be expected from contact with the natrocarbonatite. The explanation for the all the chemical variation encountered in both the Kds of CWN and WN deposits is these melts can be attributed not just to phenocrysts and melts from different depths and temperatures existing in the same eruption, but is also is likely largely an effect of the magma mixing that occurred prior to deposition.

Implications for magma origins.

Carbonatite-silicate interactions

Determinations on the origins of the two nephelinite magmas (CWN and WN) can be approached from several geochemical angles with the data collected. The first approach would be to compare these assemblages with those from previous studies. Since it is commonly accepted that Lengai's main nephelinite magma chamber is in contact with the natrocarbonatite, then that magma composition would reflect the chemical interactions based on the system of liquid immiscibility between the carbonatite-silicate liquids.

There is a compositional similarity between the CWN melt composition of this study (Figure 4a) to the olivine-melilitite nephelinites from Lengai (Figure S-

4b, Klaudius and Keller 2006). These most recent CWN eruptive deposits are even more silica and alumina deprived than those previous deposits presented in Figure S-4b (Klaudius and Keller, 2006), however those were whole rock (lava) analyses that include all minerals as well, which could account for the apparent lower SiO₂ content in these deposits.. This high degree of peralkalinity, as evidenced by the presence of combeite, low Al₂O₃ and SiO₂ wt%, suggests that the CWN (layers BCD and M) is from the primary nephelinite magma chamber known historically to bear combeite (Dawson 1962, 1995). In addition, CWN at Lengai has historically occurred in close proximity both stratigraphically and isotopically to the natrocarbonatite deposits (Keller and Kraft 1990, Bell and Dawson 1995), which is interpreted as evidence that the CWN is the nephelinite magma of Lengai's main chamber which has a zone in contact with the natrocarbonatite magma 'cap'.

Dawson (1998) hypothesized that the natrocarbonatite formed from liquid immiscibility reactions involving the crystallization of combeite from WN to form CWN, citing evidence of combeitic reaction rims on Ne and CPX. Earlier aspects of this study (Thomas et al. 2018) support this by evidence of combeitic reaction rims on CPX, nepheline overgrowth and compositional zoning, and in this study with CPX and andradite resorbition rims and combeite microcrystalline groundmass (Figure 3). Klaudius and Keller (2006), argued that this was not sufficient evidence of formation of natrocarbonatite from WN by liquid immiscibility, and that there would also be evidence in the form of an increase in available SiO₂, FeO, MnO, Al₂O₃, MgO, TiO₂ in the CWN. These oxides are detected in the CWN in this

study, however if their presence is simply due to the process of generation of natrocarbonatite by liquid immiscibility, that would not explain the plinian eruption of 2007. It is presumable that these oxides were encountered by others by the process of magma mixing that caused this eruption occurring in the past. In addition the increase of MnO in their analyses was not necessarily due to liquid immiscibility reactions since, the presence of alabandite (MnS) in the natrocarbonatite SEM analyses from this study (Table S-1) suggests that MnO fractionates preferentially into the carbonatite melt, as opposed to the silicate melt as hypothesized by Klaudius and Keller (2006). In addition, high Ba (8.7 atomic wt%,) and Sr (3.0 atomic wt%) in the gregoryerite groundmass indicate Sr and Ba preferentially fractionate into the natrocarbonatite as suggested in previous studies (Keller and Spettel, 1995; Kjarsgaard et al, 1995; Dawson 1998; Veksler et al, 2005).

Another indicator of silicate-carbonatite melt interaction may be evident in the K content of the samples. K content in the minerals from natrocarbonatite was 1-7 atomic wt% (Table S-1), far higher than K content in the CWN (<1 wt%, Figure S-7h), this suggests K preferentially fractionates into the natrocarbonatite. This would suggest the WN, which has higher K₂O than the CWN, had less or no contact with the natrocarbonatite. The distribution of K (Figure S-7h) by layer demonstrates two distinct melt compositions (one K₂O and SiO₂ poor, and one K₂O and SiO₂ rich); with what appears to be some crossover or overlap in Layer E (high SiO₂, low K₂O). This would be expected as the injection of the WN would inevitably contact the natrocarbonatite as a function of viscosity and density contrast between the

CWN and WN (Thomas et al , in prep) at some point prior to eruption, depleting it in K, Ba, Sr, Mn, S, and any necessary C, Ca and Na. In addition, this WN would still maintain its high Si and Al content as enough time had not elapsed for sufficient crystallization of the remaining elements to occur as it had with the CWN, which had been slowly cooling and crystallizing combeite in the primary magma chamber since the 1993 eruption.

Again, Layer E (from WN deposits) displayed the greatest variability in composition, displaying properties from both CWN and WN; with both the highest concentration of La and the lowest concentrations of Lu. With one exception (WN, Layer E), the CWN deposits produced REE patterns which were relatively low in LREE and high in HREE, as compared to the WN (Figure 9a, Table S-2). Since the LREE are compatible in the natrocarbonatite, and HREE are not, the inverse correlation of HREE and LREE concentrations in CWN suggests it evolved through contact with the carbonatite.

Mineral Partition Co-efficients (Kds)

REE and trace element distributions for Ti-andradite and CPX phenocrysts have ranges of up to 3 orders of magnitude. The elemental partition coefficients generated from this data set can further indicate the origins of the CWN and WN melts. In Figure 13, the calculated elemental Kd values from andradite phenocrysts in both CWN and WN are plotted against known garnet Kds from the GERM database. It is important to note that the composition of these garnets are varied, however based on their rock type they are unlikely to be Ti-andradite similar to the composition found in these samples. Analysis of the overall garnet REE and trace

element distribution patterns (Figure 13) reveal that the overall pattern presented by andradite from the CWN melt is reflected (although far less concentrated) by the Garnet Pyroxenite Kds (GERM; Zack et al, 1997). All Zr Kds for the CWN fall within the range for carbonatite (Sweeney et al. 1992). The range of Kds presented for La in both CWN and WN was very defined.

The CWN La Kds were the same as those for hawaiite (GERM; Irving & Frey 1978). In contrast, the Kds for La and Lu from the WN matched the Kds for alkali basalt, (GERM; Shimizu 1981), not only confirming the WN and CWN originated from very different regions, but also suggestive that the WN contains a deeper mantle signature associated with a hot spot. This implies that the WN deposits are not from Lengai's main nephelinite magma chamber because they don't share the CWN signature of contact with the carbonatite. Instead the WN Kds have a different signature closer to alkali-basalt. In addition, many Kds for WN matches those experimental Kds for garnet pyroxenite at 2,5-7.5 GPa (Green et al. 2000).

Although there are a lot of similarities and narrow ranges for Kds from CPX (Figure 14), significant differences between the CWN and WN can be observed. Kds for Ba, Sr and Y from the WN displayed values similar to those from Basanite-Basalt (GERM; Green et al. 2000), whereas the Sr, Kds from CWN were in the range for Garnet-Pyroxenite Basalt (GERM; Elkins et al. 2008), Ce Kds from CWN were in the range for carbonatite- silicate, whereas Ce Kds from WN were closer resembled those for Basanite-Basalt and Syenite. However even CWN La values were closest to those for Basanite-Basalt.

The mineral and melt chemistry show abundant evidence of the presence of two distinct nephelinite magmas, CWN and WN. Trace and REE concentrations and distribution in the minerals and melt of the two nephelinite magmas (CWN and WN), indicate that WN is a magma with deeper chemical signatures (composition is closer to peralkaline augite-olivine basalts, alkali basalt and garnet pyroxenite Kds). In contrast, the CWN trace and REE chemistry is closer in composition to carbonatite, and carbonatite-silicate conjugates, with some overlap with Hawaiite. This implies CWN it is from Lengai's main nephelinite chamber. An explanation is the deeper sourced WN was injected into the CWN chamber as a result of the seismic and dyking event, and then CWN and WN magmas mixed in Lengai's main chamber for a short period prior to eruption. A slightly longer interval of mixing can be seen in the chemical overlap present in Layer E, which was the last of the WN to erupt, and may have been interacting with the CWN longer.

Magma-mixing

Some of the first evidence in support of magma mixing in Lengai's ash deposits was CPX resorption, primary mineral instability, Mg overgrowths, and nepheline overgrowth and compositional zoning (Thomas et al 2018). This textural evidence in support of short term mixing of the WN and CWN was also encountered in this study. In the BSE image from the BCD layer of the CWN deposits (Figure 3) there is evidence of nepheline evidencing step zoning, an almost fully and a partially resorbed CPX, and a garnet with resorption rim, all in a combeitic groundmass.

CPX resorption is one of the mineralogical indicators of disequilibrium between the phenocryst and surrounding melt (Thomas et al. 2018). These earlier studies demonstrated that there were CPX mineral grains in equilibrium with evidence of chemical convection and CPX grains with evidence of major disequilibrium (samples ASH15-EQUIL and ASH15-DISEQ, Thomas et al 2018) in the WN. In Figure S-5, ($Mg\#/Na_2O + Al_2O_3$), CWN has an overall higher Mg# than WN, which could be the result of one or more factors such as, CPX resorption, and the incompatibility of Mg in the natrocarbonatite. CPX resorption would increase the Mg, Ca and Fe in the melt. The Fe and Ca have the andradite, wollastonite, and combeite formulas to easily join, but Mg is not a main formulaic component for either andradite, nepheline, combeite, or wollastonite, which would leave it in the melt, and could explain some of the mineral overgrowth on combeite rims. Another source of the higher MgO content in the CWN could be a result of the interactions between silicate-carbonatite conjugates. MgO is known to be incompatible in natrocarbonatite (Keller and Zaitsev, 1997, Lee et al. 1994,) ,which would cause MgO from the system of liquid immiscibility to preferentially enter the silicate conjugate melt (Klaudius and Keller, 2006; Keller and Zaitsev, 2012), in this case the CWN.

The mixing of CWN and WN must have occurred along a relatively short time scale, which can be interpreted from the seismic events that triggered the injection of WN into the CWN chamber. However, this may not be the first time a deeper nephelinite has been injected as a result of seismic or other forces into Lengai's main nephelinite magma chamber, Figure S-4b demonstrates that similar unrelated

nephelinite compositions have erupted in the past.

The most compelling evidence in support of magma regeneration from depth causing chemical instability in the main magma chamber occurs in the time series of seismic and eruptive events at Lengai (Figure 1c). In the time series of earthquakes and eruptions at Lengai (Figure 1c) we see that all eruptions of VEI 2 or higher at Lengai since 1960 have been pre-empted by seismic swarms of MbN 3-6. In fact there have not been any recorded seismic swarms at Lengai which were not followed by an eruption within 2 months or less.

Geophysical and Eruptive Correlation

A geophysical study (Kendall et al, 2005) has shown that magma intrusion plays a pivotal and as of yet understood role in the final transitional stages of continental breakup from continental rifting to seafloor spreading, and the method by which this magma is incorporated in the extending plate is unclear (Bastow et al 2010). There have been several recent geophysical models of the seismic activity and dyke propagation at Lengai, such as the geophysical study by Biggs et al in 2013, containing geodetic observational data from Lengai/Gelei area for 2007-2010. In the Biggs et al. (2013); study they describe continued normal slip (graben faults), and they investigate the pre- and syn- eruptive stress changes and suggest one of three sources of the seismic onset was the presence of dykes deep and narrow enough to be geodetically undetected. The dykes would be capable of causing the stress changes necessary to trigger the ~1m long slip on a normal fault which was coupled by the

peak 5.9 magnitude event, supporting the premise that the seismic events at Lengai are magmatically driven, and supports the presence of deep magmatic injections of magma at Lengai.

The earthquake swarm coupled with dyke intrusion and swelling was an indicator of magmatic recharge from a deeper source below Lengai, supporting the suspicion that there is third magma chamber below Lengai. This recharge was evident in the SW-NE dyke propagation (Baer et al, 2008) away from the area of surface deformation, with a subsequent eruption and deflation.

The correlation of seismic and eruptive events at Lengai (Figure 1c) also suggests that these rift related faulting events (evidenced by seismic swarms) occur just prior to all the historic explosive eruptions. This correlation of seismicity too explosivity at Lengai was evident in the most recent eruption sequence. Starting on July 17, 2007, when a magma driven earthquake swarm, consisting of approximately 70 MN4 earthquakes, with a peak event of 5.9MbN which occurring at depths of 8-15km (Biggs et el, 2009), struck the Oldoinyo Lengai/Gelai region. This seismic event produced extensive surface deformation, and was followed by the Sept 4th 2007 plinian eruption. The dyke convergence (15-20km) and the depths of dyke propagation (8-15km) supports the presence of intrusion of magma a deeper source below Lengai. The injection of the deeper sourced WN (wollastonite-nephelinite) magma into the primary CWN (combeite-wollastonite-nephelinite) Lengai magma, is the result of the seismic activity and subsequent dykeing event below and around Lengai.

It has been suggested (Baer et al, 2008), the earthquake swarm was largely

induced by magma dykes, which originated from a deep-seated magma chamber below Lengai.

Traces of associated faulting and dyke migration converge at point 10km east of Lengai, where it is reasonable to assume the boundary of the primary nephelinite magma chamber, which exists at depth of ~2-3km. InSAR Elastic modeling of the temporal migration of the dykes supports the premise that the magma source of the dykes was a deep-seated magma chamber below Lengai; since the dykes originated from this point of convergence and propagated from this point in a SW-NE trend (Biggs et al, 2013; Baer et al, 2008).

A summary of data supporting the presence of a deep-seated magma source at Lengai are summarized in a schematic demonstrating the currently known geochemical and geophysical constraints on the system in Figures 15a-h. Three of these schematics are presented below, the rest can be found in the supplementary materials. Since, it is known that the deepest dyke was at 15-20km depth, and the dyke convergence was at approximately 11km depth (Biggs et al, 2009), it can be inferred that there is more than one deeper magma source below Lengai if magma travelled from as deep as 20km, to converge at a depth of 11km. Coupled by the subsequent dome growth of up to 40cm (InSAR, Baer et al 2008), the magma travelled up to Lengai's main nephelinite (CWN bearing) chamber, where WN mixed with the CWN for a short period prior to eruption. In Figure S-15, several potential depths are presented based on data from this and other studies. In addition the deposition sequence of CWN and WN by layer is shown in Figure S-15. Further support of this hypothesis could be presented calculating by density,

viscosity, and geophysically constrained velocities from the geochemistry of the WN and CWN of these eruptive deposits.

Alternate Hypotheses

In this study, we present data in support of the hypothesis that the 2007-8 explosive eruption at Lengai was triggered by magma mixing of two distinct nephelinite magmas. This occurred from injection of a deeper-sourced wollastonite-nephelinite magma (WN) into Lengai's main nephelinite magma chamber containing the combeite-wollastonite nephelinite (CWN). The correlation between seismic activity and explosive eruptions at Lengai (Figure 1c), suggests that the deeper WN is being remobilized into the CWN chamber by seismic or other related activity.

The possibility exists that such features observed in the phenocrysts such as reverse zoning, resorption rims and compositional variation, can also be caused by convection within a magma body with one composition. This convective magma mixing can explain how the crystals undergo heating events and the occurrence of intermingling of crystals that have very different thermal histories, since the magma is heated from below and cooled from above. Convective self mixing is a premise which allows for the existence of mineral compositions that cannot coexist under equilibrium conditions (Couch et al, 2001). Although this is a simple and reasonable outcome, it does not account for the sudden explosive eruption of 2007. The ranges in REE and trace element concentrations in the various layers would have to be accounted for by shallower convective cycles that were in contact with the natrocarbonatite and deeper convective cycles that did not contact the

natrocarbonatite. However, this would still not trigger the eruption, unless it occurred in combination with the system being shaken up by the seismic swarm, causing bubble nucleation leading to the explosive eruption. If these textural and compositional observations were simply the product of convective self mixing, and the eruption the product of bubble nucleation, there is still no explanation provided by these outcomes for the observed volatile content, in particular the high H₂O content in the nepheline phenocryst melt inclusions from the WN deposits (De Moor et al. 2012).

The De Moor et al. (2012) study attributes the high explosivity of the 2007 eruption to the volatile content of the ascending nephelinite, in the schematic proposed a vent plug forms which prevents the exsolution of gases through liquid immiscibility and quiescent degassing of the natrocarbonatite. The De Moor et al. (2012) model describes a system cyclic eruptions based on cycles of quiescent degassing alternated by periods of vent obstruction caused by crystallization driven by the lowering of the liquidus due to H₂O exsolution from the nephelinite to the natrocarbonatite melt. Many of the features observed in this study can be explained by this pattern of volatile exsolution-driven crystallization which can change the mineral stability fields causing resorption, oscillation zoning and overgrowth and stimulate chemically-driven convection. This does not account for the high volume of WN deposits sandwiched between the 2 layers of CWN deposits (Layer BCD and M) in the stratigraphic ash column (Figure 2). The combeitic-wollastonite nephelinite (CWN) from Layer BCD represents the vent plug, and that part of the eruption is very well explained in the De Moor schematic of the eruption, as driven by the

buildup of volatiles in the ascending nephelinite melt. The subsequent deposition of layers E-L of the wollastonite-nephelinite (WN) deposits, followed by more deposition of CWN is not explained by their model, but it is explained by the eruptive viscosity driven magma mixing model presented by Clynne (1999).

In Clynne's model (1999) as magmas of differing viscosities compete to exit the vent of the volcano via the conduit. These magmas flow becomes entrained by laminar flow and viscosity constraints in the volcanic conduit, such that the slower more viscous flows adhere to the conduit walls during the passage of the faster (hotter, lower viscosity) melts through the central portion of the conduit. Therefore, in this model once the plug is blown, the lower viscosity (hotter, faster) magmas erupt continuously, and the slower, higher viscosity melts last. This model explains the deposition found in the Lengai deposits, In addition, Clynne's model for magma-mixing also accounts for generations of disequilibrium phenocryst assemblages, and the presence of reacted and unreacted minerals in one deposit.

Figure 15c - Time 3: 27 AUGUST 2007- Dykeing convergence completed from Gelai to Lengai (lateral NE-SW trending), deepest dykes detected at 15-20 km, magma accumulation occurs, causing injection into Lengai's main chamber

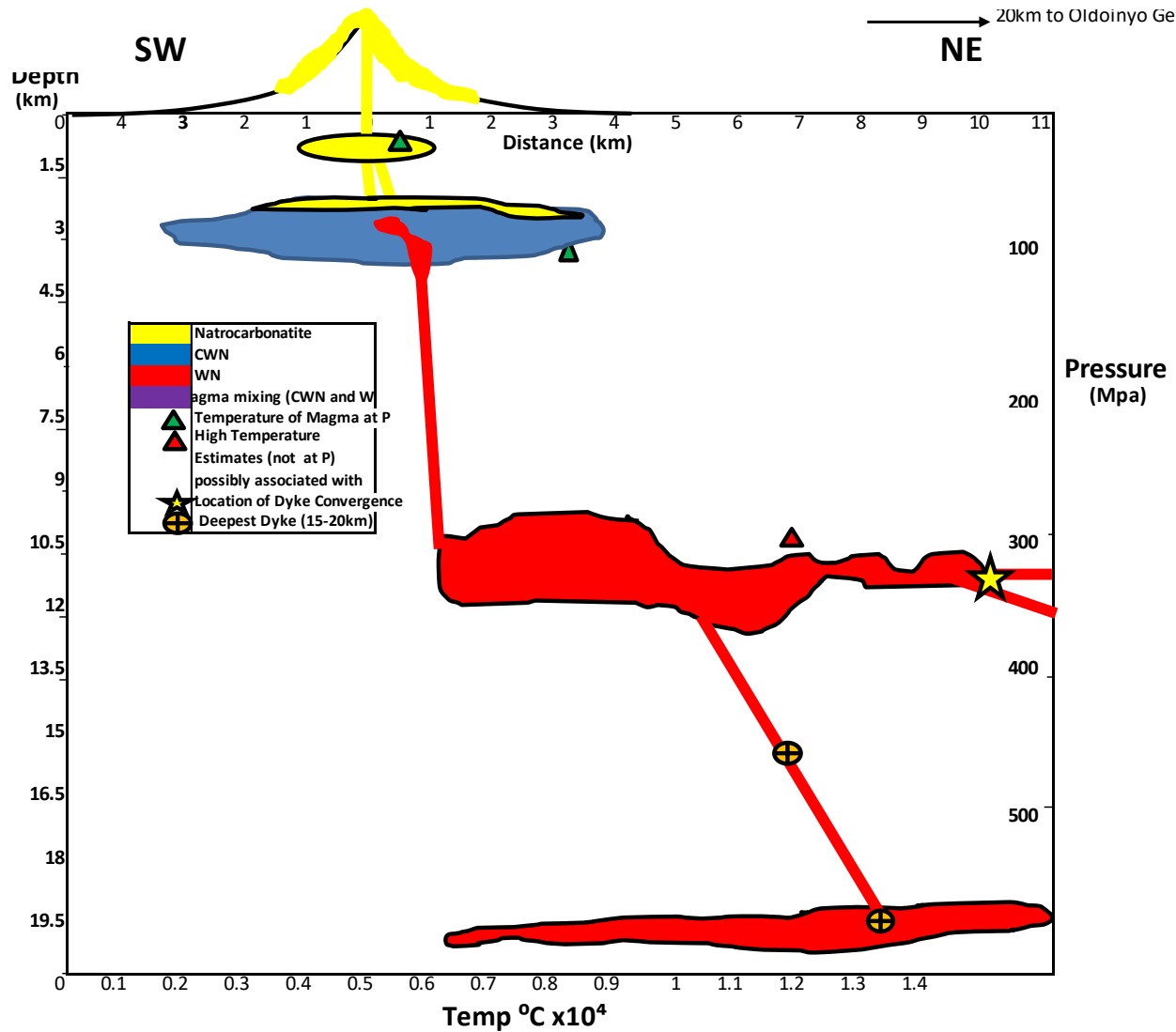


Figure 15a: Time series schematic of Lengai's eruption with deposition sequence, dyke depths and proximities. Temperature is in $^{\circ}\text{C} \times 10^{-4}$ on the bottom x-axis, distance on land surface in km on the upper x-axis. Depth below land surface in km is on the left y-axis, and pressure in Mpa on the right y-axis. Symbols: natrocarbonatite (yellow-NT), wollastonite-nephelinite (red-WN), combeitic-wollastonite nephelinite (blue-CWN) location of dyke convergence (yellow star), deepest dykes (orange circle marked with a cross), high temperature estimates for nephelinite at Lengai (red triangles), temperature of magma at pressure (green triangles). Red lenses represent hypothetical magma locations of the source for the WN deposits based on known dyke and seismic activity.

[Time 3: 27 AUGUST 2007]- Dykeing convergence completed from Gelai to Lengai (lateral NE-SW trending), deepest dykes detected at 15-20 km, magma accumulation occurs, causing injection into Lengai's main chamber

Sources: Baer et al. 2008; Biggs et al. 2009, 2013; GVP 2008; Albaric et al. 2009

Figure 15e - Time 5: SEPT 4 2007- Eruption onset, Deposition of CWN (Layer M) from main nephelinite chamber

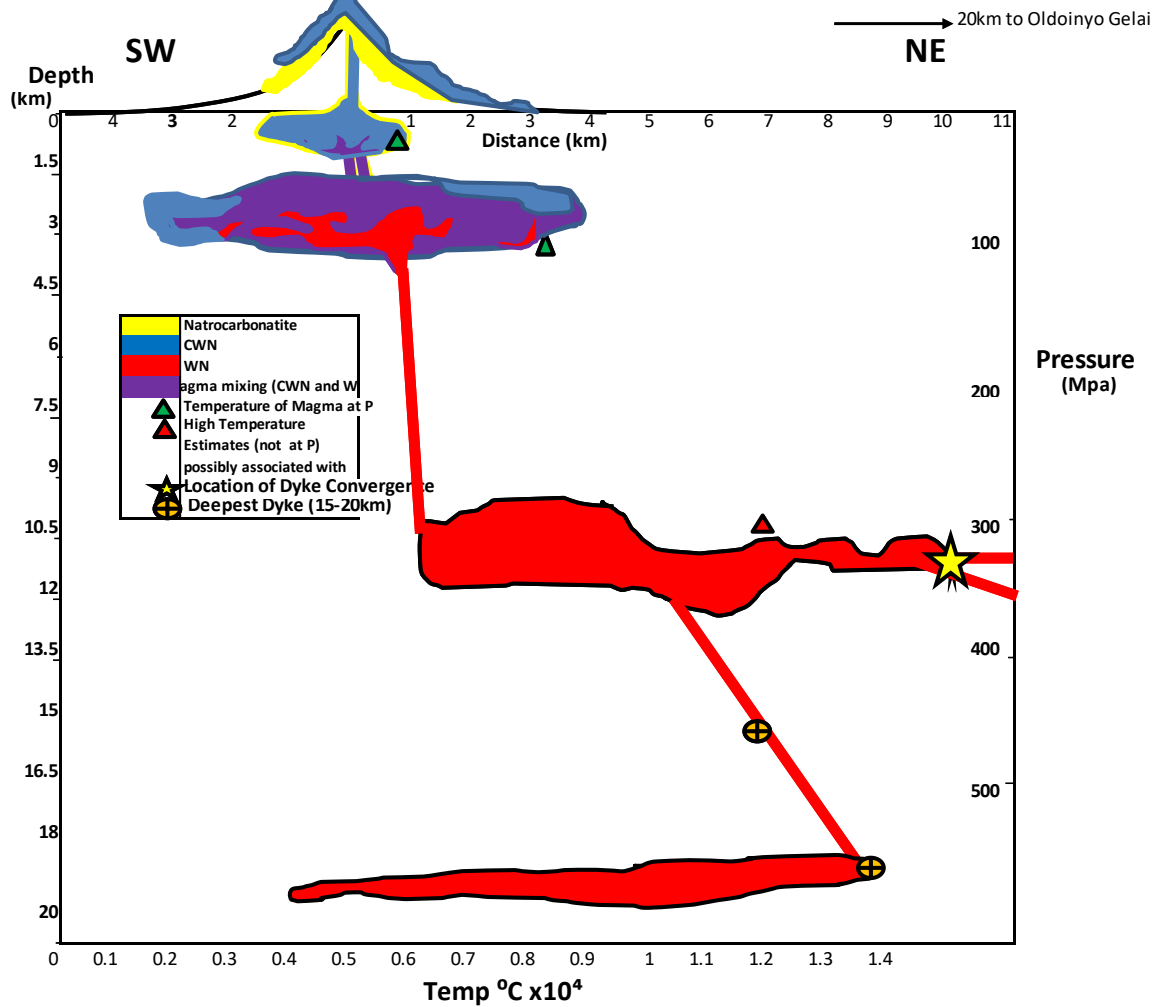


Figure 15e: Time series schematic of Lengai's eruption with deposition sequence, dyke depths and proximities. Temperature is in $^{\circ}\text{C} \times 10^{-4}$ on the bottom x-axis, distance on land surface in km on the upper x-axis. Depth below land surface in km is on the left y-axis, and pressure in Mpa on the right y-axis. Symbols: natrocarbonatite (yellow-NT), wollastonite-nephelinite (red-WN), combeitic-wollastonite nephelinite (blue-CWN) location of dyke convergence (yellow star), deepest dykes (orange circle marked with a cross), high temperature estimates for nephelinite at Lengai (red triangles), temperature of magma at pressure (green triangles). Red lenses represent hypothetical magma locations of the source for the WN deposits based on known dyke and seismic activity.

[Time 5: Sept 4 2007- Eruption onset, Deposition of CWN (Layer M) from main nephelinite chamber

Sources: Baer et al. 2008; Biggs et al. 2009, 2013; GVP 2008; Albaric et al. 2009

Figure 15h - Time 8: Mar-April 2008: End of eruption sequence Deposition of CWN left in main chamber (Layer BCD)

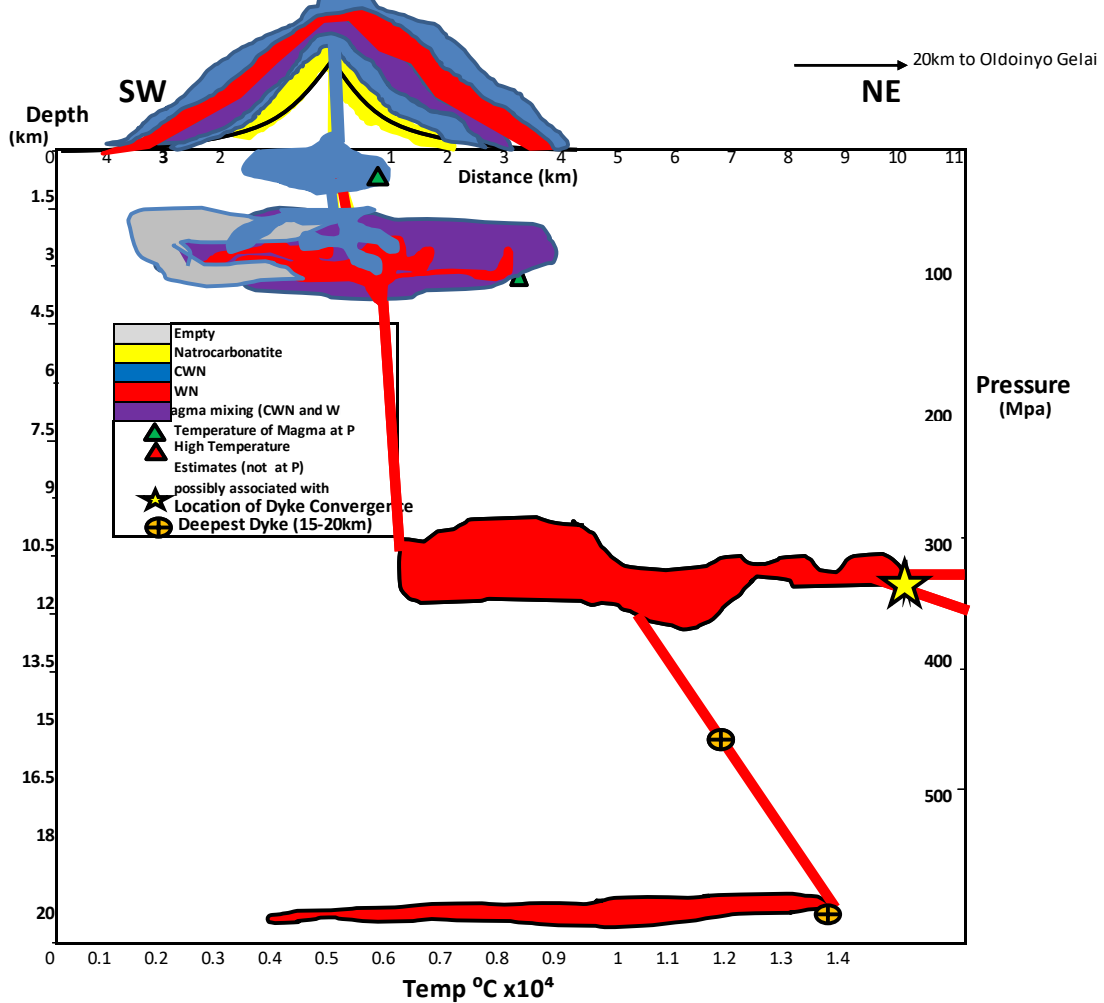


Figure 15h: Time series schematic of Lengai's eruption with deposition sequence, dyke depths and proximities. Temperature is in $^{\circ}\text{C} \times 10^{-4}$ on the bottom x-axis, distance on land surface in km on the upper x-axis. Depth below land surface in km is on the left y-axis, and pressure in Mpa on the right y-axis. Symbols: natrocarbonatite (yellow-NT), wollastonite-nephelinite (red-WN), combeitic-wollastonite nephelinite (blue-CWN) location of dyke convergence (yellow star), deepest dykes (orange circle marked with a cross), high temperature estimates for nephelinite at Lengai (red triangles), temperature of magma at pressure (green triangles). Red lenses represent hypothetical magma locations of the source for the WN deposits based on known dyke and seismic activity.

[Time 8: Mar- Apr 2008] eruption sequence ending, deposition of last of CWN deposits (Layer M).

Sources: Baer et al. 2008; Biggs et al. 2009, 2013; GVP 2008; Albaric et al. 2009

Conclusion

This REE and trace element study of the ash deposits examines the presence of two distinct melt compositions in the 2007-8 eruption of Oldoinyo Lengai from the stratigraphic ash deposits. Layer BCD and M a combeitic-wollastonite nephelinite (CWN), which represent the top and bottom of the eruptive deposits (Figure 1b), and Layers E, G, LK (WN), which represent deeper sourced wollastonite-nephelinite. The deeper sourced WN came into contact with the CWN of Lengai's main magma chamber and as a result of magma mixing between the two created some melt with compositional overlap (Layer E, Figure 4a). The presence of resorption of andradite and CPX phenocrysts (Figure 3) evidences the chemical instability of minerals in the surrounding melt. This pattern of melt variability is not new at Lengai (Figure S-4b - Klaudius and Keller 2005), nor is the pattern of seismicity prior to eruption (Figure 1c).

The CWN (combeite-wollastonite-nephelinite) and WN (wollastonite-nephelinite) ash deposits identified in the mineralogical study conducted by Thomas et al (2018) demonstrated significant compositional variation (i.e. solution range in CPX, resorption rims, nepheline step-zoning, and Mg overgrowths), to imply magma mixing occurred prior to and/or during the 2007-8 eruption at Oldoinyo Lengai.

Additional mineralogical indicators that there was injection of magma was H₂O content found to be up to 20wt% in melt inclusions from nepheline phenocrysts in the WN (De Moor et al, 2013).

Geophysical indicators in support of magma mixing can be seen in the correlation between seismic events and explosive (nephelinite) eruptions at Lengai (Figure 1c). The pattern of seismic events leading up the eruption suggests there may have been an injection of deeper magma into Lengai's primary (nephelinite) magma chamber.

Since WN demonstrates deeper-sourced signatures and CWN displays chemical signature of being in contact with the carbonatite it is reasonable to assume that Lengai's primary chamber is fed by this deeper nephelinite source which is released upon deep seismic events.

In addition, the comparison of these deposits to those of Lengai's eruptive past demonstrates that this pattern of two different nephelinite magmas in the large cone-building deposits (Figure S-4a) has occurred historically in conjunction with these explosive events.

Lengai, as a Si undersaturated Natrocarbonatite-Nephelinite stratovolcano, presents a petrological and geochemical mystery. The larger picture incorporating known geophysical data to the geochemical data from this study and Thomas et al. 2018, can provide potential insights into magma-mixing reactions, and possibly provide pressure and temperature constraints that would further confirm the presence of a deeper magma source.

References

- Baer, G., Hamiel, Y., Shamir, G. & Nof, R., Evolution of a magma driven earthquake swarm and triggering of the nearby Oldoinyo Lengai eruption, as resolved by InSAR, ground observations and elastic modeling, East African Rift, 2007, *Earth planet. Sci. Lett.*, 272 (2008.): 339–352
- Baker, B.H., Mohr, P.A., Williams, L.A.J. Geology of the eastern rift system of Africa. *Geol. Soc. Am. Spec. Pap.* 136 (1972): 1–67.
- Bastow, Ian D., and Derek Keir. "The protracted development of the continent-ocean transition in Afar." *Nature Geoscience* 4.4 (2011): 248-250.
- Benoit, J.P., McNutt, S.R. Global volcanic earthquake swarm database 1979–1989. U.S. Geological Survey Open File Report USGS OFR96-39 (1996): 333.
- Biggs, J., Amelung, F., Gourmelen, N., Dixon, T.H. & Kim, S., InSAR observations of 2007 Tanzania rifting episode reveal mixed fault and dyke extension in an immature continental rift, *Geophys. J. Int.*, 179 (2009a): 549–558.
- Biggs J., Amelung F., Gourmelon N., Dixon T., Kim Sang-Wan, "InSAR observations of 2007 Tanzania rifting episode reveal mixed fault and dyke extension in an immature continental rift," *Geophysical Journal International*, (Oct 2009), 179:549–558, <https://doi.org/10.1111/j.1365-246X.2009.04262>.
- Biggs, J. E. Robertson, and M. Mace, 2013. ISMER -- Active Magmatic Processes in the East African Rift: A Satellite Radar Perspective. *In: Remote Sensing Advances for Earth System Science* (pp. 81-91) Springer, Berlin Heidelberg.
- Couch, S., R. S. J. Sparks, and M. R. Carroll. "Mineral disequilibrium in lavas explained by convective self-mixing in open magma chambers." *Nature* 411.6841 (2001): 1037-1039.
- Dawson, J.B., "The Geology of Oldoinyo Lengai," *Bull Volcanol* (1962) 24: 349. <https://doi.org/10.1007/BF02599356>
- Dawson J. B., Pyle D. M., and Pinkerton H., "Evolution of Natrocarbonatite from a Wollastonite Nephelinite Parent: Evidence from the June, 1993 Eruption of Oldoinyo Lengai, Tanzania," *The Journal of Geology* (Jan 1996), 104(1):41-54. <https://doi.org/10.1086/629800>
- Dawson J.B., Hili, P.G. "Mineral chemistry of a peralkaline combeite lamprophyllite

nephelinite from Oldoinyo Lengai, Tanzania,” *Mineralogical Magazine* (Apr 1998) 62(2):179- 196.

Dawson J.B., Joseph V. Smith, and I. M. Steele, “Combeite ($\text{Na}_2\text{Ca}_2\text{Si}_3\text{O}_9$) from Oldoinyo Lengai, Tanzania,” *The Journal of Geology* (1989) 97:3, 365-372

Dawson JB, Bowden P, Clark GC “Activity of the carbonatite volcano Oldoinyo Lengai, 1966”. *Geol Rundsch* (1968) 57:865–879.

Dawson JB, Pinkerton H, Norton GE, Pyle D (1990) Physicochemical properties of alkali carbonatite lavas: data from the 1988 eruption of Oldoinyo Lengai, Tanzania. *Geology* 18:260– 263.

De Moor M., Fischer T.P., King P., Botcharnikov R.E., Hervig R.L., Hilton D.R., Barry P., Mangasini F., Ramirez C., “Volatile-rich silicate melts from Oldoinyo Lengai volcano(Tanzania):Implications for carbonatite genesis and eruptive behavior” *Earth and Planetary Science Letters* (Jan 2013), 361:379-390

Fairhead, J.D., Girdler, R.W. The seismicity of Africa. *Geophys. J. R. Astron. Soc.* 24 (1971): 271–301.

Fischer, T.P., Burnard, P., Marty, B., Hilton, D.R., Furi, E., Palhol, F., Sharp, Z.D. &Mangasini, F. Upper-mantle volatile chemistry at Oldoinyo Lengai volcano and the origin of carbonatites, *Nature*, 459 (2009), 77–80.

Foster, A.N., Ebinger, C.J., Mbede, E., Rex, D. Tectonic development of the northern Tanzania sector of the East African Rift System. *J. Geol. Soc. London* 154 (1997): 689–700.

Jestin, F., Huchon, P., Gaulier, J.M., The Somalia plate and the East Africa Rift System. *Geophys. J. Int.* 116 (1994): 637–654.

Keller J., Zaitsev A.N., Geochemistry and petrogenetic significance of natrocarbonatites at Oldoinyo Lengai, Tanzania: Composition of lavas from 1988 to 2007, *Journal of Volcanology and Geothermal Research* (Jan 1997), 75:89-106; <https://doi.org/10.1016/j.lithos.2012.08.012>

Kervyn, M., Ernst, G.G.J., Keller, J. et al., “Fundamental changes in the activity of the natrocarbonatite volcano Oldoinyo Lengai, Tanzania,” *Bull Volcanol* (2010) 72: 913. <https://doi.org/10.1007/s00445-010-0360-0>

Klaudius J., Keller J., Peralkaline silicate lavas at Oldoinyo Lengai, Tanzania.*Lithos* (Oct 2006), 91(1-4):173-190 <https://doi.org/10.1016/j.lithos.2006.03.017>

Lee, Woh-Jer, and Peter J. Wyllie. “Experimental Data Bearing on Liquid Immiscibility, Crystal Fractionation, and the Origin of Calcicarbonatites and Natrocarbonatites *International Geology Review*, vol. 36, no. 9, 1994, pp. 797–819., doi:10.1080/00206819409465489.

- McIntyre, R.M., Mitchell, J.G., Dawson, J.B., "Age of the fault movements in the Tanzanian sector of the East African Rift system," *Nature* (1974), 247:354–356.
- Mitchell, R. H., and J. B. Dawson. "The 24th September 2007 ash eruption of the carbonatite volcano Oldoinyo Lengai, Tanzania: mineralogy of the ash and implications for formation of a new hybrid magma type." *Mineralogical Magazine* 71.5 (2007): 483-492.
- Nimis, P., and P. Ulmer. "Clinopyroxene Geobarometry of Magmatic Rocks Part 1: An Expanded Structural Geobarometer for Anhydrous and Hydrous, Basic and Ultrabasic Systems." *Contributions to Mineralogy and Petrology* 133.1-2 (1998): 122-35.
- Nyblade, A.A., Owens, T.J., Gurrola, H., Ritsema, J., Langston, C.A. Seismic evidence for a deep upper mantle thermal anomaly beneath East Africa. *Geology* 7 (2000): 599–602.
- Nyblade, A. "The upper mantle low velocity anomaly beneath Ethiopia, Kenya and Tanzania: constraints on the origin of the African Superswell in eastern Africa and plate versus plume models of mantle dynamics." *Volcanism and Evolution of the African Lithosphere* 478 (2011): 37-50.
- Peterson, T.D. "Peralkaline nephelinites. I. Comparative petrology of Shombole and Oldoinyo Lengai, East Africa" *Contr. Mineral. and Petrol.* (1989) 101: 458. <https://doi.org/10.1007/BF00372219>
- Peterson T.D., Kjarsgaard B.A., What Are the Parental Magmas at Oldoinyo Lengai?. In: Bell K., Keller J. (eds) *Carbonatite Volcanism. IAVCEI Proceedings in Volcanology*, vol 4. Springer, Berlin, Heidelberg
- Petibon, C.M., Kjarsgaard, B.A., Jenner, A., Jackson, S.E., Phase relationships of a silicate-bearing natrocarbonatite from Oldoinyo Lengai at 20 and 100 MPa. *Journal of Petrology* 39 (1998): 2137–2151
- Thomas N., Fischer T.P., Brearley A.J., Mineralogical indicators of magma-mixing: Oldoinyo Lengai 2007-8. *American Mineralogist* (in prep) 2018.
- Wim Van Westrenen, Jonathan P. Blundy, Bernard J. Wood. A Predictive Model Of Thermodynamic garnet-Melt Trace Element Partitioning. *Contributions to Mineralogy and Petrology* 142 (2001): 213-234.
- [Olivine, Pyroxene, Garnet, Spinel and Feldspar Spreadsheets](#): (updated by Rhian Jones, 2015)
https://serc.carleton.edu/research_education/equilibria/mineralformulaerecalculation.html
- [Clinopyroxene Formula Spreadsheet](#): (cpx.formula.v2)
https://serc.carleton.edu/research_education/equilibria/mineralformulaerecalculation.html

[ml](#)

LazyBoy, V3.77f (10/09/2013); copyright (all rights reserved): Joel Sparks (2001, 2004, 2011, 2013) jwsparks@bu.edu.

GERM (Geochemical Earth Reference Model) Partition Coefficient (Kd) database: <https://earthref.org/KDD/> (Kds from: Larsen 1979, , Irving and Frey 1978, Shimizu 1980, Sweeney et al. 1992, Fujimaki et al. 1984, Zack et al, 1997, Green et al. 2000).